

ALL-FIBER AMPLIFIER BASED ON CHIRALLY-COUPLED-CORE FIBERS FOR GRAVITATIONAL WAVE DETECTORS

Von der QUEST-Leibniz-Forschungsschule
der Gottfried Wilhelm Leibniz Universität Hannover
zur Erlangung des akademischen Grades

Doktor der Naturwissenschaften
Dr. rer. nat.

vorgelegte Dissertation von

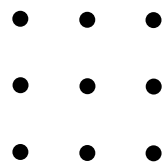
M.Sc. Sven Hochheim
geboren am 29.03.1991 in Gehrden

2023

Referent: Prof. Dr. Benno Willke, Leibniz Universität Hannover
Korreferent: Prof. Detlef Ristau , Leibniz Universität Hannover
Prof. Volker Quetschke, University of Texas Rio Grande Valley

Tag der Promotion: 18.01.2023

'Connecting the dots'
- Steve Jobs



Abstract

High-power lasers are required for the development of novel gravitational wave detectors based on interferometric measurements. The design study for the European 'Einstein Telescope' revealed that the optical performance of current used laser systems is no longer sufficient for the desired specifications of advanced detector designs. The development of such powerful laser systems is therefore a wide field of research and is of current interest. In particular, fiber amplifiers have increasingly come to the fore in recent years due to their excellent beam quality, even at higher power levels.

The power scaling of such laser systems beyond current limitations is the concept of this work. In the area of single-frequency fiber-based laser systems, the non-linear effect of stimulated Brillouin scattering represents the fundamental limitation. In particular, a significant excess noise level of the laser system can be measured above this threshold. In this context, the intensity noise was investigated in more detail. Here, the conversion of phase to intensity noise plays a crucial role. For the first time, the characteristics of the additional broadband noise was reconstructed based on the parameters of an asymmetric Brillouin gain spectrum.

The optical output power of fiber-based single-frequency laser systems is scaled, for example, by increasing the effective mode area of the fiber. For the compensation of the resulting reduction of the beam quality in fiber amplifiers, the special concept of the 'chirally-coupled core' (3C[®]) fiber was developed. This fiber type reduces the content of guided higher order modes through additional side cores rotating around the actual signal core. Compared to other specialty fiber types with micro-structures inside, this fiber features an all-solid design. The light-guiding properties of the 3C[®]-fiber were examined with a specially developed S²-setup and the high content of the guided fundamental mode in the fiber core was experimentally confirmed.

For the first time, optical fiber components were integrated directly into such a 3C[®]-fiber. Especially, the manufacturing of signal and pump light couplers opens up new possibilities for the development of advanced fiber amplifier systems. In this work, a first monolithic single-frequency fiber amplifier design was realized, which achieves a power level of over 300 W. This prototype is based on a 3C[®]-fiber without the need for additional fusion splices, because the optical fiber components were integrated directly into the Ytterbium-doped 3C[®]-fiber. So, the optimal beam parameters were realized after the amplification process. In particular with regard to the guided fundamental mode content of over 90%, this work emphasizes the high potential of fiber amplifiers based on 3C[®]-fibers as laser sources for the special requirements of gravitational wave detectors.

Key words: Fiber amplifier, 3C[®]-fiber, gravitational wave detector

Kurzfassung

Für die Entwicklung neuartiger Gravitationswellendetektoren auf Basis interferometrischer Messungen werden spezielle Hochleistungslaser benötigt. Die Designstudie für das europäische "Einstein Teleskop" offenbarte, dass die optischen Leistungslevel aktueller Lasersysteme für die zukünftig angestrebten Spezifikationen nicht mehr ausreichend sind. Die Entwicklung solcher leistungsstarken Lasersysteme ist daher ein weitreichendes Forschungsgebiet und von aktuellem Interesse geprägt. Insbesondere Faserverstärker sind durch ihre exzellente Strahlqualität auch bei höheren Leistungen in den letzten Jahren zunehmend in den Vordergrund gerückt.

Die Leistungsskalierung solcher Lasersysteme über aktuelle Limitierungen hinaus ist das Konzept dieser Arbeit. Im Bereich von einfrequenten faserbasierten Lasersystemen stellt dabei der nichtlineare Effekt der stimulierten Brillouin-Streuung die grundlegende Limitierung dar. Insbesondere ist ein signifikantes Rauschen des Lasersystems oberhalb dieser Schwelle messbar. In diesem Zusammenhang wurde das Intensitätsrauschen genauer untersucht. Die Konversion von Phasen- zu Intensitätsrauschen spielt dabei eine entscheidende Rolle. Erstmals konnte die Charakteristik des zusätzlichen breitbandigen Rauschens basierend auf den Parametern eines asymmetrischen Brillouin Verstärkungsspektrums rekonstruiert werden.

Die Leistungsskalierung von faserbasierten und einfrequenten Lasersystemen erfolgt beispielsweise durch die Vergrößerung der effektiven Kernfläche. Um die daraus resultierende Minderung der Strahlqualität in Faserverstärkern auszugleichen, wurde das Konzept der "chirally-coupled core" (3C[®]) Faser entwickelt. Dieser Fasertyp reduziert den Anteil geführter höherer Moden durch zusätzliche um den eigentlichen Kern rotierende Seitenkerne. Im Vergleich zu anderen Spezialfasertypen mit Mikrostrukturen weist diese Faser ein komplettes Glasdesign auf. Die lichtführenden Eigenschaften der 3C[®]-Faser wurden mit einem speziell entwickeltem S²-Aufbau untersucht und der hohe Anteil der geführten Grundmode im Faserkern experimentell bestätigt.

Zum ersten Mal wurden optische Faserkomponenten direkt in solch einer 3C[®]-Faser integriert. Insbesondere die Herstellung von Signal und Pumplichtkopplern eröffnet neue Möglichkeiten für die Entwicklung neuartiger Verstärkersysteme. In dieser Arbeit wurde erstmals ein monolithisches einfrequentes Faserverstärker-Design realisiert, welches ein Leistungslevel von über 300 W erreicht. Dieser erste Prototyp mit einer 3C[®]-Faser beruht auf dem Design, in der die optischen Faserkomponenten direkt in der Ytterbium-dotierten 3C[®]-Faser integriert wurden und somit auf die Notwendigkeit zusätzlicher Spleiße verzichtet werden konnte. Somit wurden bestmögliche Strahlparameter nach dem Verstärkungsprozess realisiert. Insbesondere in Hinblick auf den geführten Grundmodenanteil von über 90% unterstreicht diese Arbeit das hohe Potential von Faserverstärkern auf Grundlage von 3C[®]-Fasern als Laserquellen für die speziellen Anforderungen von Gravitationswellendetektoren.

Schlagerwörter: Faserverstärker, 3C[®]-Faser, Gravitationswellendetektoren

Contents

1	Introduction	1
2	Fundamentals of Single-Frequency Ytterbium-doped Fiber Amplifiers	7
2.1	Characteristics of optical fibers as waveguides	7
2.1.1	Ytterbium-doped fibers in laser and amplifiers	10
2.1.2	Fiber modes	12
2.2	Stimulated Brillouin scattering	14
2.3	Chirally-coupled-core fibers	18
2.3.1	Conceptual understanding of 3C [®] -fibers	19
2.3.2	3C [®] -fibers in fiber amplifiers architectures	23
3	Impact of Stimulated Brillouin Scattering on Noise Properties of Single-Frequency Signals	25
3.1	Conceptual understanding of the conversion from phase to intensity noise	25
3.2	Experimental layout and measurement method	28
3.3	Experimental results	29
3.4	Reconstruction of the low-frequency excess intensity noise	32
3.5	Conclusion	34
4	Integrated Optical Components in 3C[®]-Fibers	35
4.1	Characterization concept of an S ² -imaging technique	36
4.1.1	Experimental layout	39
4.1.2	S ² -measurement of a 3C [®] -fiber	43
4.2	Mode field adapter	45
4.3	End cap	48
4.4	Cladding light stripper	49
4.5	Signal and pump combiner	52
4.5.1	Detailed investigations of a multi pump-port 3C [®] -fiber combiner	55
4.6	Conclusion	56
5	Prototype of a 100 W all-fiber Single-Frequency 3C[®]-Fiber Amplifier	59
5.1	Experimental layout	59
5.2	Beam quality characterization	61
5.2.1	Optical Slope and polarization extinction ratio	61
5.2.2	Modal content analysis	63
5.2.3	Stimulated Brillouin scattering	65
5.2.4	Temperature behavior	66

5.3	Conclusion	67
6	High-power spliceless 300 W Single-Frequency 3C[®]-Fiber Amplifier Module	69
6.1	Prototype of an 170 W single-frequency all-fiber 3C [®] -fiber amplifier	70
6.1.1	Experimental layout	70
	Advanced interface device	71
6.1.2	Beam quality characterization	73
6.1.3	Conclusion	75
6.2	Experimental layout	75
6.3	Beam characterization	77
6.3.1	Experimental results of the pre-amplifier	77
6.3.2	Optical Slope and Spectrum	78
6.3.3	Polarization extinction ratio	80
6.3.4	Power stability in operation	81
6.3.5	Modal content analysis	82
6.3.6	Relative power noise	84
6.3.7	Transverse mode instabilities	85
6.3.8	Stimulated Brillouin scattering	86
6.4	Enhanced reliability through interlock system	87
6.5	Conclusion	90
7	Summary and Outlook	93
	Bibliography	97
	Appendix	123
A	Advanced mode field adapter	123
B	Automatic interlock system	125
B.1	List of used electrical components	126
	Publications	127
	Curriculum Vitae	129

CHAPTER 1

Introduction

The history of gravitational waves goes all the way back to the novel consequences of Albert Einstein's general theory of relativity in 1916 [Ein16], as they would have been inconceivable in Newton's classical theory of gravity. The direct detection of gravitational waves on the 14th of September 2015 made events, such as the merging of two black holes, in the universe 'audible' for the first time [Abb16]. This knowledge not only influenced the astronomy, but also revolutionized the entire physics and opened up a new perspective on the universe. This is a paragon of modern scientific research and shows at the same time important aspects, about how international research collaborations work together with a common goal and the use of large measuring equipment, complex computer simulations and powerful and stable high-power laser systems. In 2017, Rainer Weiss, Kip Thorne and Barry Barish were awarded with the Nobel prize in Physics for their contribution to this work.

Gravitational waves can be described as disturbances in the curvature of spacetime propagating away from their origin at the speed of light. As a solution of the equations of Einstein's general relativity, any mass that changes its speed or the direction of speed in space (with the exception of spherically symmetrical collapsing or expanding objects) produces such disturbances in spacetime. The intensity of the emitted gravitational waves depends on the involved mass but to an even greater extent on its speed change. Therefore, only astronomical objects such as neutron stars or black holes exhibit sufficiently large disturbances of spacetime, which are primarily of interest for gravitational wave research. Only compact objects can orbit each other much faster on narrow paths, so that they also generate significant gravitational waves. So far, four sources of gravitational waves are known which are relevant for the frequency range of ground based gravitational wave detectors (GWDs): compact binary systems, supernovae, rotating neutron stars and background noise. Thereby, these waves do not interact significantly with any kind of matter, unlike electromagnetic waves [Sch99; Sig98], which makes the proof even more difficult.

The story of the experimental search for gravitational waves through the use of GWDs begins with the physicist Joseph Weber in the early 1950s [Gro18]. Weber's basic idea was to use a large mass in the form of a cylinder made of an aluminum alloy that can be excited into vibrations by a gravitational wave. This excitation of the cylinder is most effective, when the oscillation frequency of the spatial disturbance coincides with the eigenfrequency of the cylinder and accordingly, the *Weber-cylinder* has the best sensitivity at a certain frequency. Such a cylinder, operated at room temperature, achieved a sensitivity of 10^{-16} at an oscillation frequency of 1660 Hz [Web69]. Limited due to the thermal noise, these

resonance antennas were not able to detect directly a gravitational wave according to scientific consensus so far, even if Weber had published the opposite [Web72; Web71].

In the 1970s, the idea of using the new technology of a Michelson interferometer to measure gravitational waves has been discussed by various scientists, e.g. experimentally by Rainer Weiss and theoretically by Kip Thorne. Hereby, a slight phase shift of the light waves in the two arms of the interferometer induced by the distortions of the spacetime can be detected. Based on this idea, the LIGO (Laser Interferometer Gravitational-Wave Observatory) project was launched in 1984 through the initiative of Rainer Weiss, Kip Thorne and other scientists [Gro18]. The advanced LIGO (aLIGO) systems belong to the second generation of GWDs, which use an arm length of 4 km at the two locations Hanford and Livingston in the USA [Aba12]. Through active seismic pre-isolation of the 40 kg test masses, which are suspended on glass fibers, electrostatic actuators and signal recycling, a strain sensitivity between $10^{-23} \text{ Hz}^{-1/2}$ and $10^{-21} \text{ Hz}^{-1/2}$ in the frequency range of 10 Hz to 10 kHz can be reached [Hil09]. A variety of GWDs was set up in Italy (VIRGO since 1994 and later advanced VIRGO), Germany (GEO600 since 1995) and in Japan (TAMA since 1995 and KAGRA since 2010) over the last decades and other detectors such as LIGO-India are in the construction phase [Gro18].

On 14th of September 2015 at 9:50:45 am, the two aLIGO detectors registered the cosmic event *GW150914* of a merging binary system of two black holes at a distance of 1.4 billion light years [Abb16]. This signal corresponded to a relative expansion of the space-time of 10^{-21} and was detected before the data runs O1 and O2 [Gro18]. At the end of the O2 data run, the merging of two neutron stars was registered on the 17th August 2017. Besides, this event *GW170817* was detected by the satellites *Fermi* and *INTEGRAL* and also subsequently by optical telescopes [Abb17]. The direct evidence for gravitational waves is complete after fifty years of vigorous effort but on the other hand, a new phase in the use and further developments of these instruments as a new tool of astronomy begins. For the 3rd generation of GWD and the improvement of the sensitivity of ground-based detectors over their astrophysical range, three main factors are important: 1. the length of the arms, 2. the rest of the (test-) masses and 3. the power of light. In particular, increasing the light power leads to an improved sensitivity at higher frequencies of GWDs, because the limiting shot-noise decreases proportional to the square-root of the laser power [Row00]. For these purposes, a high-power injection-locked laser system was initially developed in master-oscillator power-amplifier (MOPA) configuration [Win11]. The seed signal of a non-planar ring oscillator (NPRO) was amplified to an optical output power of 35 W by Nd:YVO₄ crystals and the subsequent high power oscillator using Nd:YAG crystals enabled an optical output power level of 200 W at 1064 nm.

The current high power laser source of a 140 W pre-stabilized amplifier system operating at 1064 nm reduces the complexity of the past injection-locked oscillator and was used with an output power level of 70 W in the third observation run of the aLIGO detectors [Adh06; Bod20a]. Here, the power level of 2 W of the NPRO was amplified in the first stage by the existing 35 W-solid state amplifier as a copy of the enhanced LIGO (eLIGO) system [Fre07]. Afterwards, a neoVAN-4S solid state amplifier built by the company neoLASE [neoLase; Thi19] was used with four sequentially arranged water-cooled Nd:YVO₄ crystals pumped with fiber coupled pump-diodes at 878 nm [Bod20b].

However, the laser system requirements of future detector generations with optical power levels of several hundreds of watts such as for the European project "Einstein Telescope" (ET) can not be fulfilled by current amplifier architectures [Abe11]. The infrastructure of ET will consist of three arms, each 10 km long, arranged in a triangle [Abe11], where a new development is emerging in which individual interferometers are specially optimized for a certain frequency range of gravitational waves. Stabilization techniques to increase the sensitivity of GWDs at low and high frequencies can not be performed simultaneously [Gro18]. For example, with increased laser output power in the interferometers, the radiation pressure noise increases, which can lead to an impairment of the sensitivity at lower frequencies. Therefore, there will be also included laser systems at longer wavelength (1.5 - 2 μm [Kap20; Var17b]) for the low-frequency system next to the amplifier designs at wavelengths around 1.0 μm . Thereby, in combination with silicon test masses at cryogenic temperatures, the impact of thermal noise in the mirror substrates and coatings can be reduced and will decrease the lower observation frequency limit to <1 Hz [Abe11]. At the high-frequency system for the frequency band between 50 Hz and 10 kHz, a laser system of at least 500 W at 1064 nm in front of the interferometer is desired for a significant reduction of the shot noise level [Abe11].

Typically, GWDs are operated in DC readout [Fri12], which means that power fluctuations and frequency noise of the laser system directly couple to the interferometer readout. Besides, due to the Fabry-Perot cavities inside the interferometer arms, the fundamental Gaussian mode is required for an efficient performance. Therefore, a high power single-frequency (SF) laser beam with the highest possible spatial beam quality and low power and frequency noise levels is needed for suitable GWD sensitivities.

The amplification of such a SF signal with excellent beam quality properties constitutes various challenges to the laser systems, which were previously fulfilled by solid-state laser architectures at the expense of system complexity. Another promising laser technology to fulfill these special requirements and reduce the complexity are fiber-based MOPA systems. Benefiting from the telecommunications sector, the development towards high power amplifier designs with several kilowatt [Zha18a] of continuous-wave (CW) output power has grown steadily over the last decades. However, the amplification process of SF signals is typically limited by the onset of stimulated Brillouin scattering (SBS). As a nonlinear effect, SBS depends on the laser intensity in the fiber core, whose power-limiting effect can be avoided in the simplest form by increasing the core diameter of the fiber. In this way, various additional single-frequency fiber amplifiers with a high power scalability have been developed in recent years. In 2008, Mermelstein et al. presented 194 W output power [Mer08] and in 2011 Zhu et al. demonstrated up to 511 W output power in a fiber-based single frequency system [Zhu11]. In context of the development of laser sources for the next-generation of GWDs, different institutes worked on the integration of fiber amplifiers in such high power laser systems [Bui19; Dix20]. Theeg et al. published an all-fiber SF amplifier prototype with 300 W output power pumped in counter-propagation [The12a]. As an enhancement of this work, Wellmann et al. reported in 2019 a low noise, high power fiber amplifier engineering prototype with a pump power limited output power of 200 W at 1064 nm [Wel19], which fulfills the requirements of GWDs except for the desired power level for ET. The single-frequency output power record is held by Robin et al. with an output

power level of 811 W [Rob14], but 10% of the output power were already propagating backwards because of SBS.

However, due to the physical properties of a conventional step-index fiber, a purely single-mode operation at 1064 nm can be achieved up to a mode field diameter (MFD) of around 21 μm [Kop00], whereby these fiber amplifiers are limited in power scaling by SBS [The12a]. To reduce the impact of nonlinearities and to overcome these limitations, specialty fiber types were developed over the last decades to ensure a single-mode operation also at enlarged MFDs. Especially, the photonic crystal fiber (PCF) has found its way into commercial use due to the large variety of applications and is considered as a prime example of specialty fibers. For example, the highest power level of 811 W by Robin et al. was achieved with such a PCF [Rob14]. However, due to the micro-structured pattern with an arrangement of air holes inside a PCF, these fiber types are only partially suitable for the construction of fiber-based optical components. Here, specialty fiber geometries based on an all-solid design exhibit a significant advantage for the assembly of all-fiber laser systems. A promising specialty fiber concept in this context with an enlarged MFD and an active suppression of higher order modes is the so called chirally-coupled-core (3C[®]) fiber. The research group around Prof. Almantas Galvanauskas has demonstrated that fiber modal properties can be manipulated by introducing a side core near to the signal core by taking the advantage of involving an optical angular momentum to the signal-side core mode interaction [Ma11b]. Thus, even with an enlarged core diameter of 34 μm , the 3C[®]-fiber performs as an effectively single-mode fiber [Ma14].

Consequently, the 3C[®]-fiber concept enables further power scaling of SF fiber MOPA laser sources beyond the limitations of typical large mode area fibers. Such new laser technologies or architectures are necessary in particular to achieve the desired sensitivity level of ET and further next-generation GWDs. Potential concepts such as coherent beam combining have already been successfully tested [Wel21], however, the complexity is also increased again in such systems. Here, 3C[®]-fibers allow output power performance levels of several of hundreds of watts using a single amplifier stage. Additionally, to decrease the system complexity and increase the reliability, compact and stable all-fiber solutions are particularly suitable, but require fiber-based optical components for this purpose. Such SF all-fiber amplifier systems based on 3C[®]-fibers with integrated components in regard to laser sources for the next generation of GWDs have not been developed so far and are the main part of this work.

In this context, Chapter 2 gives a brief overview about the essential fundamentals of optical fibers as waveguides, the basics of SBS and in particular the working principles of 3C[®]-fibers. In Chapter 3, the impact of SBS on the broadband excess noise properties of SF signals is analyzed. Here, the conversion of phase noise to intensity noise plays a major role for the explanation of the characteristic broadband intensity noise spectrum. Chapter 4 consists of the description of integrated optical components in 3C[®]-fibers such as a mode field adapter (MFA), cladding light stripper (CLS) or pump combiner (PC). For the characterization of these components, an S² imaging technique was designed with the opportunity to determine the guided modal content inside the 3C[®]-fiber core in real-time. An all-fiber amplifier prototype with a 100 W SF output beam and the first essential component of a MFA is characterized in Chapter 5. Based on this experimental experience,

the existing all-fiber amplifier system was improved by the integration of a CLS and a PC directly in a single piece of 3C[®]-fiber. The first Section 6.1 of Chapter 6 presents the experimental results of a 170 W SF 3C[®]-fiber amplifier design pumped with two high-power laser diodes. In the second Section 6.2, the available pump power was doubled with the integration of a 4-port PC, so that finally a high-power 300 W SF 3C[®]-fiber amplifier in a spliceless configuration was realized for the first time. Afterwards, the characterization of the beam quality was considered in terms of the requirements of current and further GWDs. Eventually, an interlock system is demonstrated, which significantly decreases the shutdown time of these or other laser systems. In Chapter 7, an overall conclusion is drawn and a potential outlook is given. Especially, the development of 3C[®]-fibers with an even larger MFD opens the door to a completely new power scaling of SF fiber amplifiers beyond the limitations of SBS. In total, this work emphasizes the field of applications of 3C[®]-fibers in high power laser systems for the next generation of GWDs.

CHAPTER 2

Fundamentals of Single-Frequency Ytterbium-doped Fiber Amplifiers

In this chapter the theoretical background of important aspects of SF fiber amplifiers related to the presented work is introduced. At first, the operation principle of optical fibers as waveguides is discussed. Here, it is essential to understand the modal properties of fibers, in order to develop laser systems for applications such as GWDs. The next section provides the fundamentals of power scalability limitations due to stimulated Brillouin scattering. In Section 2.3 the particular fiber design of the chirally-coupled-core (3C[®]) fiber is presented to enable a single-mode operation at an enlarged MFD and to overcome current limitations.

2.1 Characteristics of optical fibers as waveguides

Optical fibers are dielectric waveguides, which guide electromagnetic waves over long distances in a refractive index distribution. Due to the fiber geometry, a transmission of light with an excellent beam quality can be guaranteed and makes it interesting for a variety of optical applications.

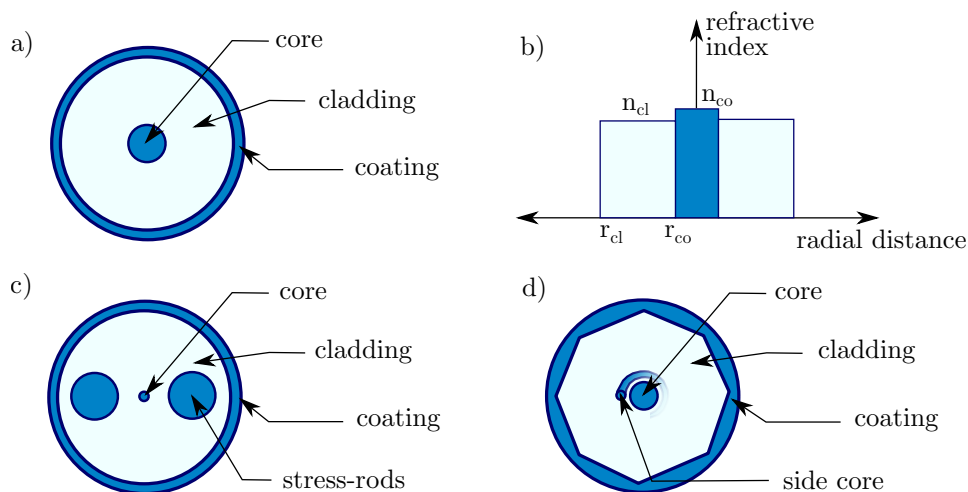


Figure 2.1: Visualization of a cross-section of a typical step-index fiber in a) with the corresponding refractive index profile in b). The parameter $r_{co/cl}$ and $n_{co/cl}$ denote the radius and refractive indices of the core and cladding. In c) a polarization-maintaining fiber is shown in a PANDA configuration. Other fiber designs with additional rotating side cores were developed such as chirally-coupled core fibers in d).

The schematic image of a conventional step-index fiber is depicted in Fig. 2.1 a). In the simplest type, the fiber consists of a signal core with a radius r_{co} and an optical refractive index $n_{\text{co}} > n_{\text{cl}}$ surrounded by a cladding glass cylinder with radius r_{cl} and a slightly lower refractive index n_{cl} [Mar91a]. In principle, all dielectric materials can be used, but, due to the extremely low attenuation in the visible and near infrared spectral range, pure SiO_2 -glass (*fused silica*) is the standard low-cost material [Iza87; Mit05; Oh12]. It should also be mentioned that other materials, e.g. Fluoride [Ada01; Saa09] are interesting for technical systems regarding a corresponding applications. The actual fiber fabrication process consists of a fiber preform production and the drawing of the fiber [Buc04]. In the first step, a cylindrical fused silica preform is fabricated in regard to the relative dimensions of the fiber as well as with their refractive indices. The most commonly used method is the modified chemical vapor deposition (MVCD) [Nag82; Ter14], where a hollow fused silica glass tube is heated up and rotated around its symmetry axis. Injected gas particles are then accelerated towards the walls of the heated tube by thermophoresis for chemical interaction [Tan06]. Due to the temperature gradient between the center of the tube and the wall, pure fused silica layers accumulate on the tube wall. Depending on the fiber parameters, e.g. the core size, the number of layers may vary [Agr01]. After all layers are deposited, the tube is collapsed under high induced heat to form the solid preform. Adjustments of the refractive indices of the core and cladding can be realized by adding dopants to the SiO_2 -host. For that, dopants such as GeO_2 or P_2O_5 are typically used to raise the refractive index, while e.g. B_2O_3 reduces the refractive index [Kyo93; Yeh90]. The combination of new dopants in different concentrations enables new types of fiber compositions, especially, in conjunction with laser-active materials (see Sec. 2.1.1).

In the second process step, the preform is placed at the top of a drawing tower, in which the preform is locally molten and then drawn with the gravitational force [Buc04]. Real-time measurements and feedback control loops of the drawing rate determine and control the fiber diameter. The mechanical stability against external stress is guaranteed by an additional high refractive index polymer coating [Agr01], which is applied in a molten form to the fiber.

The principle guidance properties of fibers are based on the concept of total internal reflections on the optical thinner medium [Glo71a]. The corresponding constant refractive index design within the core and cladding of a so-called step-index fiber is shown in Fig. 2.1b). The index contrast between the core and the cladding determines the important parameter of the numerical aperture (NA) of the core

$$\text{NA} = \sqrt{n_{\text{co}}^2 - n_{\text{cl}}^2} = \sin(\theta_{\text{max}}), \quad (2.1)$$

where θ_{max} corresponds to the maximum angle of incidence light, which can be coupled into the core [Buc04].

Another characteristic is the polarization property of optical fibers. If linearly-polarized light would be coupled into a perfectly circular and isotropic fiber, the polarization state would be maintained during the propagation through the fiber. However, the manufacturing process imprints some anisotropies and asymmetries into the real fiber. In

general, additional mechanical stress is imprinted on the fiber due to fiber bending or twisting, which breaks the circularly symmetric design and the degree of birefringence of the fiber. As a consequence, the refractive indices n_x and n_y slightly change along this axis. This effect can be minimized by using a polarization-maintaining fiber with a strong built-in birefringence, so that the polarization state will be preserved in one of the birefringent axes. In the manufacturing process of the preform, the introduced strong birefringence will be implemented by additional boron-doped stress rods with a modified glass composition (see Fig. 2.1c). Due to different thermal expansion coefficients of the $B_2O_3:SiO_3$ -rods compared to pure silica, the birefringence is induced during the drawing process [Buc04]. A commonly used method based on stress rods with a circular symmetric core shape, is called PANDA (polarization-maintaining and absorption-reducing fiber) [Shi83]. In addition to PANDA-fibers, other variants of geometries such as bow-tie fibers with trapezoidal prism stress rods or geometries with an elliptical core or cladding, where the elliptical form itself implements a birefringence, were introduced [Kum84; Nod86; Ter14; Y80].

The physical principle behind these concepts is the coherent mode coupling. The propagation constants β_x and β_y of the two polarization eigenmodes will evolve differently in both (slow- and fast-) axis of the fiber. The quantity

$$B_m = \frac{|\beta_x - \beta_y|}{k} = |n_x - n_y| \quad (2.2)$$

was defined as a measure of its variation [Kam81] with $k = \frac{2\pi}{\lambda}$ as the free-space wavenumber. A phase relation with the resulting polarization beat-length

$$L_b = \frac{\lambda}{B_m} = \frac{\lambda}{\Delta n_{\text{eff}}} \quad (2.3)$$

between the modes of 2π is accumulated [Fil90; Kam81]. This means that a periodicity of the modal power transfer occurs and the phase relation is restored after integer multiples of L_b . Consequently, here the coupling between the modes is most effective [Buc04].

Along conventional and real fibers, the parameter B_m and therefore L_b are not constant. This effect is most noticeable in PM-fibers used in fiber amplifier or laser systems, where random power fluctuations between the two polarization modes occur with typical beat-lengths in the order of 10 m. However, it is intolerable for applications such as interferometric GWDs, where only a certain polarization state can be used and polarization variations would couple into other noise properties of the entire interferometer.

Polarization-maintaining (PM) fibers suppress the polarization cross-talk between the modes by reducing the beat-length to a few centimeters or even only a few millimeters ($B_m \sim 10^{-4}$) [Buc04; Shi83]. With proper fiber designs, finally cross-talk values of ≥ 30 dB have been achieved [Muk17].

Besides to the stress-rods integrated inside the cladding, the actual fiber design of the cladding plays an important role to extract the power of fiber laser or amplifiers in general. Only the technology of double-clad fibers allows fiber-based high-power lasers or amplifiers in conjunction with multi-mode pump sources. These diodes deliver up to several kW of pump power at different wavelengths [Dil20; Las20a; nLi20], where the pump light is

guided in the first cladding and the high-brightness light in the core of the fiber [Sni88]. Thereby, the first cladding has a significantly larger mode field area compared to the core. The refractive index determines the index profile and accordingly the NA of the cladding, where a large number of propagation modes can be guided. Typically, the polymer coating has a considerable lower refractive index (≤ 1.38 [Tan11]) than pure silica (~ 1.45 [Dig01]) and provides an NA of the cladding of ≥ 0.46 [Tan11]. The geometry of the cladding will usually be designed with diameters of 125 μm , 250 μm or 400 μm [Lie20], but also up to 1 mm and beyond [Nuf20].

There are a variety of different designs of double-clad fibers. In the simplest case, the fiber has a circular pump cladding and a centered core. However, the pump light can propagate on helical rays around the core, so that some significant part of pump light exhibits an incomplete overlap with the core [Zen93]. An implemented asymmetry feature in the cladding prevents this effect and therefore increases the pump light absorption [Kou02; Kou03]. Fig. 2.1 d) shows the fiber cross-section of a design concept with an octagonal cladding [Jav16; Liu04]. Other common design types base on a D-shaped cladding [Zel97] or an off-centered core [Gup20]. The implementation of birefringence in PM-fibers due to the stress rods is usually sufficient to prevent a helical propagation through the fiber. Besides, fiber designs with additional side core or other micro-structures are possible and enable new optical properties. The implementation of an additional side core in Fig. 2.1 d) allows a manipulation of the fiber modal properties for example. In this regard, the special features of these chirally-coupled-core fibers are discussed in more detail in Chapter 2.3.

2.1.1 Ytterbium-doped fibers in laser and amplifiers

In addition to the mentioned dopant materials added to the silica host, laser-active dopants can also be used as laser gain media in fiber-based lasers and amplifiers. The most common rare-earth materials in this context are Ytterbium (Yb^{3+}) [Dig01; Han88; Pas97b], Erbium (Er^{3+}) [Bar91; Kon97; Tan02], Holmium (Ho^{3+}) [Hem14; Wie16] and Thulium (Tm^{3+}) [Mor08; Pas97a] with typical infrared emission wavelengths around 1.0 μm , 1.5 μm and 2.0 μm .

In addition to the demand of Er^{3+} -doped fibers for the telecommunications industry [Dej99], Yb^{3+} -doped fibers have been continuously developed for an increasing demand of such laser systems during the last decades. Especially, the commercial interest in the material processing sector has improved the fiber technology for this spectral range. Therefore, reliable, cost-effective and efficient optical fiber-based components are well-known and widespread nowadays and enable high-power Yb^{3+} -doped (all-)fiber laser or amplifier systems. One of the highest commercially available output power of a single-mode Yb^{3+} -doped fiber laser system is 60 kW [Las20b]. Amplifier architectures with a single-frequency linewidth deliver a reported output power level of up to 800 W in combination with photonic crystal fibers [Rob14].

Such a laser process in Yb^{3+} -doped fibers bases only on two relevant level manifolds for optical wavelengths around 1.0 μm . Thereby, the ground state manifold $^2\text{F}_{7/2}$ consists of four sublevels and the excited state manifold $^2\text{F}_{5/2}$ of three sublevels (see Fig. 2.2 (a)) [Pas97b]. As it is typical for rare-earth doped fibers, the absorption and emission spectra exhibit broadband wavelength spectra, instead of discrete peaks, due to the implementation

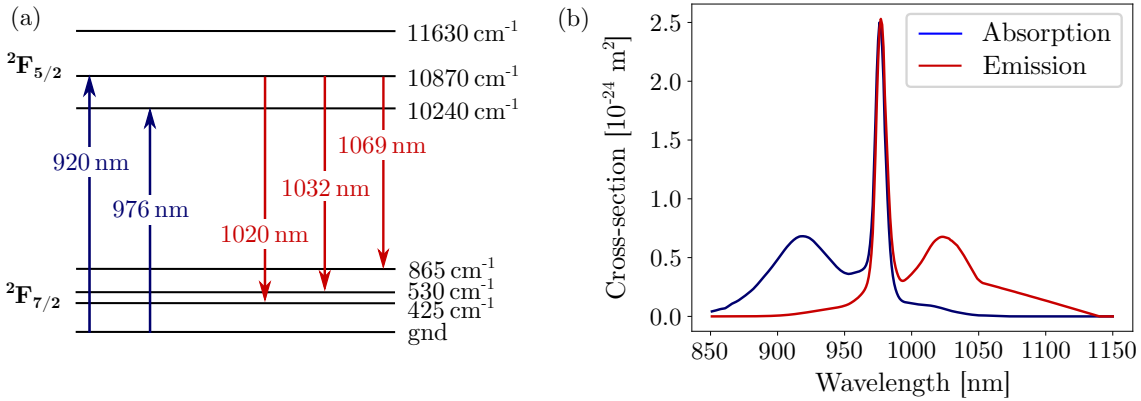


Figure 2.2: (a): Schematic overview of the important energy levels of Yb^{3+} -doped silica as presented in Ref. [New07]. (b): Typical absorption and emission cross-sections of Yb^{3+} -doped silica at around $1.0 \mu\text{m}$ [Pas97b].

Yb^{3+} -ions into the silica matrix. Other reasons for the mentioned broadening are the finite lifetime (about 0.8 ms for the excited ${}^2\text{F}_{5/2}$ laser-level [Pas97b]) of the electronic state and inhomogeneous perturbations of the Yb^{3+} -energy states by presence of the electric field of the glass host [Urq88]. This broadening effect is of particular interest for spectroscopy applications [Col18; Lou16].

The corresponding cross-sections of Yb^{3+} -doped silica in dependence of the wavelength for absorption and emission are depicted in Fig. 2.2 (b). The absorption and emission spectra can also be adjusted through the exact material composition and doping concentration [Pas97c; Pas94]. An efficient emission in the $1.0 \mu\text{m}$ band can be realized by choosing pump wavelengths around the absorption maximum peak at 976 nm. Nowadays stabilized multi-mode high-power pump diodes with emission bandwidths of 1 nm at output power levels over 200 W are commercially available in combination with $105 \mu\text{m}$ pump fibers [nLi20]. Thus, their emission spectrum is within the full width at half maximum (FWHM) bandwidth of the absorption peak ($\sim 10 \text{ nm}$) of Yb^{3+} . Instead of pumping at 976 nm, shorter wavelengths, e.g. 915 nm or 940 nm, reduce the wavelength- and thermal stabilization requirements of the pump sources due to a broader absorption of Yb^{3+} -ions in this range, but increase the required effective fiber length. The so-called off-peak pumping-technique is particularly efficient when using $\text{Yb}^{3+}:\text{Er}^{3+}$ -codoped fiber for laser processes at $1.5 \mu\text{m}$, because of an improved thermal management inside the fiber [Var17a]. Contrary to the cladding pumping concept, core-pumping enables a diffraction limited high-output power beam with shorter fiber lengths, which reduces the threshold of nonlinearities, however with increased requirements on the beam quality of the pump diodes [The16].

In addition to the actual laser process, Yb^{3+} -doped fibers exhibit a loss mechanism due to the upconversion, where the energy of two excited Yb^{3+} -ions is combined resulting in an emitting single photon in the green spectral range [Koc15; Mag94]. At other dopants, such as Er^{3+} -ions, a green fluorescence can be observed [Sch00], while a blue fluorescence is emitted in conjunction with Tm^{3+} -ions [Ung08].

In addition to the luminescence, further spontaneous emission can occur in the laser medium and can be amplified to higher power levels. This spontaneous process starts from vacuum fluctuations [Kle81; Mes08], where photons will be emitted in all spatial directions without a certain phase distribution [Bar99]. The guidance mechanism of fibers imprints a propagation direction along the principal fiber axis - however, in both directions. In (pumped) active doped-fibers, the spontaneous emission will be further amplified and will lead to the effect of amplified spontaneous emission (ASE). Furthermore, the ASE photons exhibit a low temporal coherence, but a larger spatial coherence due to the general waveguiding properties of the fiber [Bla11]. The corresponding emitted optical spectrum is similar to the shape of the emission cross-section (see Fig. 2.2 (b)). However, the shape also strongly depends on the pump wavelength, pump power or other parameters such as fiber length. The optical spectrum does not differ significantly in terms of forward or backward ASE photons, but particularly the power level of the backward propagating ASE light is higher due to the different gain distribution along the fiber [Lee13]. This effect will be used in the following Section 4.1 by introducing an S² imaging technique.

Nevertheless, in fiber laser and amplifier systems, ASE is an undesirable phenomenon and will typically be suppressed. On the one hand, generated ASE photons decrease the usable power of the target signal and on the other hand, parasitic laser processes at certain wavelengths lead to random pulsing of the laser [Agr20; Mun19]. The generated pulse will receive the entire gain and the yielding high intensity-pulse can damage sensitive optical fiber components or the fiber end-facets.

The performance of fiber-based laser systems can be adjusted by the doping concentration of active ions. Even with high Yb³⁺-doping concentrations, the ratio of the doped core to the surface area ensures a higher thermal damage threshold compared to bulk media [Zen93]. In bulk media, the design parameters have to be carefully chosen and are mostly designed for one working point [Kov99; Ott98], which also has a large impact on the beam quality. The beam quality in fiber lasers is exclusively determined by the geometric properties of the fiber and the number of guided modes. This relationship is discussed in more detail in the following Section 2.1.2.

2.1.2 Fiber modes

The guidance mechanism of an optical fiber at a given wavelength allows for a finite number of supported modes in dependence of their propagation constants and spatial electromagnetic field distribution [Agr01]. Especially, the core radius r_{co} and the difference of the refractive indices are important parameters to adjust the number of guided modes. The typical core diameters are in the order of micrometers, so that the propagation through the fiber at small angles dominates. Mathematically, the discrete transverse profiles U of the electric field amplitude can be described by solving the Helmholtz-equation in cylindrical coordinates (r, ϕ, z) :

$$\frac{\partial^2 U}{\partial r^2} + \frac{1}{r} \frac{\partial U}{\partial r} + \frac{1}{r^2} \frac{\partial^2 U}{\partial \phi^2} + \frac{\partial^2 U}{\partial z^2} + n^2 k^2 = 0, \quad (2.4)$$

where n is the refractive index, either of the core or the cladding. Starting from the Maxwell equations, the derivation will be described in detail in several references [Agr01; Buc04; Glo71b; Mar91b]. Taking appropriate boundary conditions into account, the propagation constant β also needs to fulfill [Glo71b]

$$n_{c1}k < \beta < n_{co}k, \quad (2.5)$$

which is also crucial for understanding the principle of the 3C[®]-fibers in Section 2.3. The solutions of different spatial field distributions result in a general fiber mode set [Buc04]. Under the fulfilled weak-guidance conditions, the limited number of electric field distributions that can be guided inside the fiber core, is called linearly polarized LP_{lm} modes, as it possesses only small longitudinal electric and magnetic field components [Glo71b]. The integer subscript 'l' characterizes the symmetry and mode numbers in azimuthal direction and 'm' defines the radial mode numbers. The physical significance of l and m is the number of intensity maxima (or minima) in the azimuthal or radial direction. The lowest-order mode with l=0 and m=1 (LP₀₁) exhibits an intensity profile comparable to the fundamental transverse electromagnetic (TEM₀₀) mode, particularly in cases with not too high V number [Mit10]. Thereby, the calculated overlap factor between the amplitude distribution of the LP₀₁ and TEM₀₀ mode was determined to be 99.7% [Ste15].

Mathematical solutions for Eq. 2.4 and the transverse mode fields of the LP modes can be determined by the separation ansatz

$$U(r, \phi, z) = R(r)\Phi(\phi)e^{-i\beta z} \quad (2.6)$$

with differential equations for the azimuthal field amplitude $\Phi(\phi)$ and for the radial field amplitude $R(r)$ [Rei97]. Compositions of Bessel functions of the first kind of order $J_l(u)$ describe their solutions for the fiber core. The cladding region is mathematically calculated by modified Bessel functions of second kind of order $K_l(w)$. By solving the eigenvalue equation

$$u \frac{J_{l-1}(u)}{J_l(u)} = -w \frac{K_{l-1}(w)}{K_l(w)} \quad (2.7)$$

the propagation constant β_{lm} of the LP modes can be estimated [Glo71b]. The normalized transverse phase is described by u and the normalized attenuation constant by w with the following definitions:

$$u := r_{co} \sqrt{n_{co}^2 k^2 - \beta_{lm}^2} \quad \text{and} \quad w := r_{co} \sqrt{\beta_{lm}^2 - n_{co}^2 k^2}. \quad (2.8)$$

Furthermore, the prefactors of the core and cladding section must be adjusted to realize a continuous core-cladding interface. For $l \geq 1$, there are two 90° azimuthally rotated field distributions, so that two independent polarization states exist for each possible field orientations for the LP_{lm} mode [Rei97].

The parameters l and m are closely linked with the cut-off conditions for different LP_{lm}

modes. From the Eq. 2.8 it becomes clear that its inverse dependence on the wavelength and that there is a *cut-off* wavelength λ_c , at which only the LP₀₁ will be guided in the fiber core. In this regard, a common parameter, called the *normalized frequency* [Mor03], is defined as [Buc04]

$$V = \sqrt{u^2 + w^2} = k \cdot r_{\text{co}} \sqrt{n_{\text{co}}^2 - n_{\text{cl}}^2} = \frac{2\pi}{\lambda} r_{\text{co}} \cdot \text{NA}. \quad (2.9)$$

Therefore, the number of supported modes in the fiber core, next to the wavelength, depends on the core radius and the core-cladding index difference. Besides, every LP_{lm} mode has its own cut-off parameter V_c , whereby a fiber core shows a single-mode operation, when the fiber design is chosen to achieve

$$V \leq V_c = 2.405. \quad (2.10)$$

Below this cut-off value, only the LP₀₁ mode is a solution, where $\frac{u}{w}$ corresponding to the intensity maxima is equal to zero [Rei97]. With increasing core radius more modes are guided by the fiber core, whereby this effect can be minimized by a smaller NA. In state-of-the-art manufacturing processes, the step-index fibers exhibit a typical NA limited to ~ 0.06 [Lie20; Nuf20].

Furthermore, the transverse field distribution of the beam does not coincide with the actual spatial core radius and can be approximated by a Gaussian distribution [Mar77]. In this conjunction, a characteristic of single-mode fibers ($1.2 < V < 2.4$) is the mode field diameter (MFD), which is defined as the $1/e^2$ diameter of the intensity distribution of the fundamental mode. Using Marcuse's empirical equation [Mar77]

$$\omega \approx r_{\text{co}} \cdot \left(0.65 + 1.619V^{-3/2} + 2.879V^{-6} \right), \quad (2.11)$$

the mode radius ω can be estimated from the core radius and the V parameter for a step-index fiber.

2.2 Stimulated Brillouin scattering

The electric field component \mathbf{E} of a propagating electromagnetic wave through a fiber induces a polarization component \mathbf{P} by the interaction with electric dipoles of the glass material. The nonlinear and anisotropic relation between the electric field and the induced polarization is given by [Boy03]

$$\mathbf{P} = \varepsilon \left(\chi^{(1)} \mathbf{E} + \chi^{(2)} \mathbf{E}^2 + \chi^{(3)} \mathbf{E}^3 + \dots \right), \quad (2.12)$$

with the susceptibility tensor $\chi^{(n)}$ and the permittivity ε . The continuation of the Maxwell equations leads, next to the interaction of the temporal and spectral evolution of the electric field, to the coupling of strong electric fields with high intensities and the cause of nonlinear effects. Especially in fiber cores, high intensities can occur due to the small effective mode area and therefore, the nonlinear effects exhibit comparably low thresholds. However, the fiber principle benefits from the fact that silica glass is a centrosymmetric material and

the second order susceptibility tensor is $\chi^{(2)} = 0$, accordingly, second order nonlinearities do not occur [Agr01]. Nevertheless, the nonlinearities of the third order are common side effects in the use of fibers. These effects include the photon-phonon interaction of Raman [Lin06; Ram28] and Brillouin Scattering [Bri22; Ipp72] or the response of the glass material based on the Kerr effect [Kab19; She90]. The intensity I dependence of these processes is caused by the third order susceptibility $\chi^{(3)}$, which induces a contribution to the nonlinear refractive index n_{NL}

$$n_{\text{NL}} = n_2 \cdot |\mathbf{E}|^2 = n_2 \cdot I \quad \text{with} \quad n_2 = \frac{3}{8n_{\text{linear}}} \text{Re} \left(\chi^{(3)} \right) \quad (2.13)$$

based on the second order nonlinear refractive index n_2 of the material.

The Raman as well as the Brillouin scattering are basically based on molecular vibrations in the silica host. Constituting SiO_2 molecule vibrations or rotations change the electric polarization of the molecule due to the dipole moment in a way that an oscillation frequency in the optical range will be yield [Oka06]. In this case, an incoming photon scattered on such a rotation or vibrate molecule experiences typical frequency shift in the range of 13 THz in optical fibers [Agr01].

In contrast to the Raman scattering, inelastic molecular vibrations of the SiO_2 molecule, that do not change the electric dipole moment, are associated with frequencies in the acoustic range [Oka06]. Thereby, the resulting frequency shift is in the GHz-regime and by three orders of magnitude smaller compared to the Raman scattering [Agr01]. The phenomena of Brillouin scattering, and in particular the stimulated process, will be described in more detail in the following.

First observed in 1964, Brillouin scatterings have been extensively investigated and described in the literature [Agr01; Boy03; Chi64; Gar64]. In contrast to the spontaneous Brillouin scattering, the light-scattering mechanism is introduced to be stimulated if the fluctuations are induced by the presence of the light field [Boy03]. The schematic process of the stimulated Brillouin scattering (SBS) is depicted in Fig. 2.3. It bases on the nonlinear interaction between pump light and Stokes wave due to acoustic waves. In Fig. 2.3(a), the generated scattered signal is downshifted by frequency Ω and interferes with the incoming electromagnetic wave of the pump light. The resulting intensity pattern creates a corresponding moving acoustic wave in Fig. 2.3(b) via the effect of electrostriction material density variations inside the fiber (see Fig. 2.3 (c)). Such fluctuations in the material density lead to time-dependent change of the refractive index of the medium in Fig. 2.3(d), which scatters further pump light by the pump-induced index grating and yields to the generation of SBS.

In single-mode fibers, SBS can only occur in backward direction [Agr01], whereby the frequency shift can be calculated by

$$\nu_{\text{B}} = \frac{2n\nu_{\text{A}}}{\lambda_{\text{Signal}}}. \quad (2.14)$$

With a typical refractive index value $n = 1.45$ for silica glass, an acoustic velocity $\nu_{\text{A}} = 5.96 \text{ km/s}$ [Agr01] and a signal wavelength $\lambda_{\text{Signal}} = 1064 \text{ nm}$, the frequency shift can be

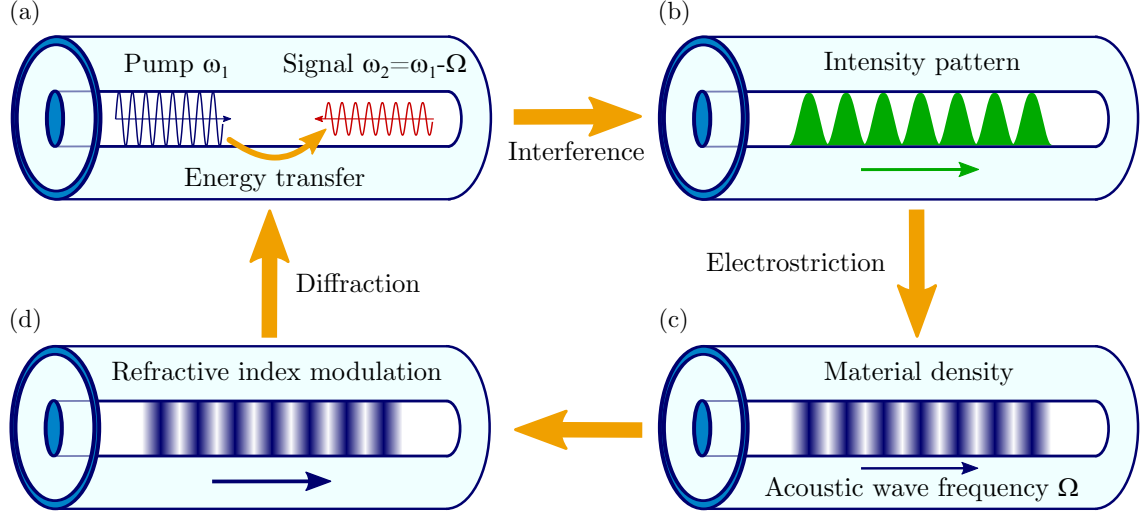


Figure 2.3: Illustration of the phenomena of stimulated Brillouin scattering (a): Schematic energy transfer from the injected pump and frequency-shifted signal wave. (b): Corresponding intensity pattern inside the fiber due to interference of propagating waves. (c): Moving acoustic wave by material density fluctuations. (d): Time-dependent change of the refractive index of the medium, where pump light will be scattered.

determined to be about 16 GHz.

Comparable to the stimulated Raman scattering (SRS), the energy transfer from the pump light to the Stokes wave is characterized by the Brillouin-gain spectrum

$$g_B(\nu) = g_{B_0} \cdot \frac{\left(\frac{\Omega_{BS}}{2}\right)^2}{(\nu - \nu_B)^2 + \left(\frac{\Omega_{BS}}{2}\right)^2} \quad (2.15)$$

with the spectrum-bandwidth Ω_{BS} and the maximum of the material-specific Brillouin gain coefficient g_{B_0} . The bandwidth Ω_{BS} is closely related to the phonon lifetime and the damping time of the acoustic wave of typically < 10 ns [Agr01]. These results in gain bandwidths in the range of a few tens of MHz (~ 10 -50 MHz [Agr01; Hil08]), whereas bandwidths of several THz are common in the case of SRS [Cha04; Sha05]. Assuming the acoustic waves decay as $\exp(-\Omega_{BS}t)$, the Brillouin gain spectrum exhibits a symmetric Lorentzian profile in Eq. 2.15. Fig. 2.4 represents the corresponding mathematical shape.

In contrast to the Raman-gain coefficient ($g_{B_0} \approx 10^{-14}$ m/W [Bro02; Sto73]), the Brillouin-gain coefficient is larger by three orders of magnitude with a value of around $2.4 \cdot 10^{-11}$ m/W [Hil08]. Therefore and in addition to the smaller gain bandwidth $\Delta\nu_{Brillouin} \ll \Delta\nu_{Raman}$ compared to the Raman scattering process, SBS is the typical power scaling limitation for single-frequency ($< \Omega_{BS}$) signals.

Consequently, the mathematical description of the power distribution inside the fiber is useful. The SBS dynamic of the pump intensity I_{pump} and the intensity of the Stokes wave

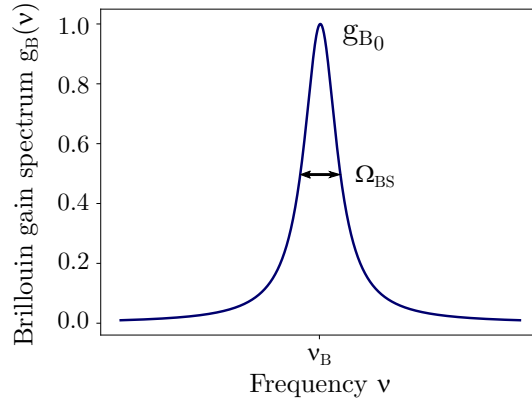


Figure 2.4: Lorentzian Brillouin gain spectrum $g_B(\nu)$ in dependence of frequency in conjunction with the bandwidth Ω_{BS} and the Brillouin gain coefficient g_{B0} at frequency shift ν_B according to Eq. 2.15.

P_{Stokes} along the fiber can be determined by two coupled differential equations

$$\frac{I_{\text{pump}}}{dz} = -g_B I_{\text{pump}} I_{\text{Stokes}} - \alpha I_{\text{pump}} \quad (2.16)$$

and

$$-\frac{I_{\text{Stokes}}}{dz} = g_B I_{\text{pump}} I_{\text{Stokes}} - \alpha I_{\text{Stokes}}, \quad (2.17)$$

where all intrinsic fiber losses are conveniently assumed by the absorption parameter α . If the power level of the signal wave exceeds a certain threshold, the output power of the Stokes light increases significantly. The estimate of the stimulated Brillouin threshold can be applied by using $I_{\text{pump}}(z) = I_{\text{pump}}(0) \cdot \exp(-\alpha z)$ in Eq. 2.16 and the integration over the fiber length L [Agr01]. The exponential growth of the Stokes intensity starting with a Stokes intensity at $z = L$ provided by spontaneous Brillouin scattering can then be determined by

$$I_{\text{pump}}(0) = I_{\text{pump}}(L) \cdot \exp(g_{B0} P_0 L_{\text{eff}} / A_{\text{eff}} - \alpha L) \quad (2.18)$$

with the effective mode area $A_{\text{eff}} = \pi \cdot \omega^2$ from Eq. 2.11 and the input power $P_0 = I_{\text{pump}}(0) \cdot A_{\text{eff}}$. The nonlinear interaction in conjunction with the $\chi^{(3)}$ -susceptibility in fibers requires an adjustment of the effective fiber length L_{eff} , which is defined as

$$L_{\text{eff}} = \frac{1 - \exp(-\alpha L)}{\alpha}. \quad (2.19)$$

Consequently, the power threshold P_{SBS} in passive fibers at which the Brillouin scattering

becomes stimulated can be expressed by

$$P_{\text{SBS}} = \frac{C_{\text{SBS}} \cdot A_{\text{eff}}}{g_{\text{B0}} \cdot L_{\text{eff}}}. \quad (2.20)$$

Therein, C_{SBS} is an empirical factor that depends on fiber parameters and is generally taken to be 21 [Agr01; Hil08; Smi72]. For modern telecommunication fibers it is rather 19 [Bill99]. In laser-active doped fibers, the doping concentration causes an inhomogeneity of the refractive index and therefore a change of the speed of the acoustic waves in the fiber [Eng14] in addition to a change of the Brillouin frequency shift. Thus, the modified optical and acoustic wave-guide properties influence the SBS process and in conclusion, the SBS threshold itself. In general, this fact must be taken into account in the design of high-power amplifiers, but has no significant implication on the statements of this work.

2.3 Chirally-coupled-core fibers

The power scaling concepts of fiber-based laser and amplifier architectures to extract at least a few watts out of such systems, are closely connected with the invention of double clad fiber structures (see Sec. 2.1) and the feature of large mode area (LMA) with an increased mode field diameter. Thus, the resulting intensity distribution inside the fiber core will be reduced [Mac04], which leads to an increased threshold for the onset of nonlinear effects, e.g. the SBS threshold. Indeed, the accompanying increased V parameter enables the guidance of higher order modes in conventional step-index fibers. The guidance properties of such modes can be modified by different methods, e.g. by coiling the fiber [Fer98; Kop00] allowed by the mode specific bend losses [Mar76; Sak78]. Commercial available LMA fibers provide core diameters up to 30 μm with a corresponding mode area of $\sim 2800\mu\text{m}^2$ [Nuf20]. At such large core diameters, the fiber has to be coiled very tightly to guarantee a high fundamental mode content [Che06]. However, the effective MFD of the LP_{01} mode will also be reduced in this case [Mac04], which leads to additional losses.

Different other approaches with special fiber design were developed in the last decades to enable a pure single-mode operation in LMA fibers. A promising fiber concept, which is already widely used in research institutions and commercial laser systems, is Photonic crystal (PCF) fibers pioneered by S.J. Russell [Rus06]. PCFs base on a micro-structured arrangement of periodic capillary lattice in the fused silica [Kni03]. In the simplest type of a PCF, a solid core is surrounded by a triangular pattern of air holes, where the core has a higher effective refractive index [Sai05]. Thus, the guidance properties can be understood similar to the behavior in a conventional fiber. In addition to the category of high index guiding PCFs, there is also the group of low index guiding PCFs. The so-called photonic bandgap fibers (PBG fibers [Cre99]) exhibit a totally different guiding mechanism, where light at certain wavelengths can only propagate at defect regions resulting from the photonic bandgap [Bir95]. The core of such PGB fibers can even be hollowed with an equivalent refractive index of close to 1, called hollow core fiber [Rus14]. The large variety of possible applications in conjunction with the photonic crystal fiber types enabled these explorations and attracted a huge interest in industry and research.

In this context, the design concept of the so-called chirally-coupled core fiber (3C[®]-fiber)

was promoted and was invented by the group of Professor Galvanauskas in the period around 2007 [Liu07b; Ma11b]. The concept bases on the interaction of guided modes with each other involving their optical angular momentum [All03] and allows a single-mode operation despite a very large core diameter. The conceptual understanding of the 3C[®]-fibers will be described in the following Section.

2.3.1 Conceptual understanding of 3C[®]-fibers

The fiber design concept of chirally-coupled-core fibers consists of a weakly-guided waveguide system. The step-index structure exhibits a signal core, which is additionally chirally surrounded by one or more side cores in optical proximity. A schematic 3D geometry of such a fiber is depicted in Fig. 2.5 with one additional side core. To obtain a helical fiber structure, the preform is spun during the drawing procedure. The preform itself can be produced conventionally with both cores running straight through it [Ma11a]. Due to the twist of the fiber in the drawing process, the cladding surface has a slightly wavy structure, which influences the manufacturing of optical components and which will be discussed in Chapter 4.

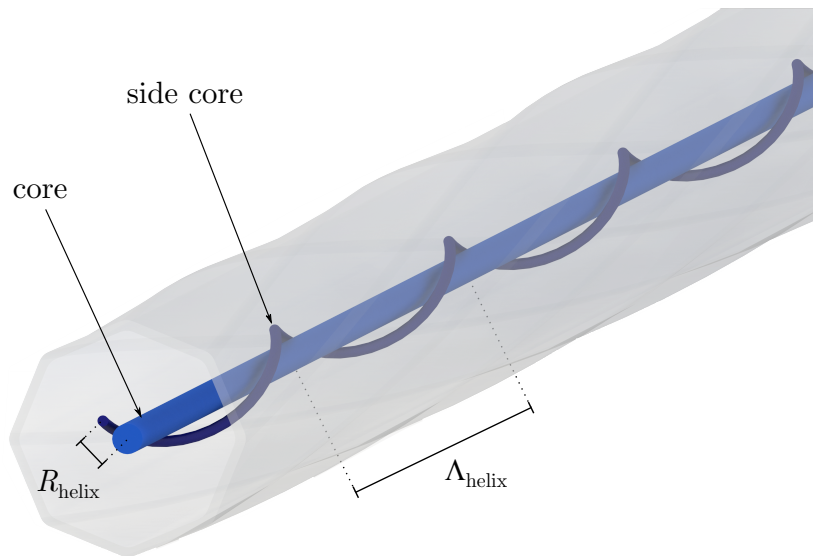


Figure 2.5: Schematic 3D geometry of the 3C[®]-fiber structure with a single side core with a constant helix pitch Λ_{helix} and helix offset R_{helix} .

The signal core is centered in the cladding with a typical core diameter of $34\ \mu\text{m}$ or $55\ \mu\text{m}$ and runs straight along the fiber axis. Doped with laser-active materials, the guided light can be amplified according to conventional fibers.

The additional side core follows a helical path with a constant helix pitch Λ_{helix} and helix offset R_{helix} along the fiber. The interaction of modal properties between signal and side core involving the angular momentum carried by each mode can be controlled by adjusting these parameters. Generally, the diameter of the side core(s) are with $\sim 10\ \mu\text{m}$ significantly smaller than the signal core.

In conventional step-index fibers with straight and parallel cores, the eigenmodes only interact with each other, when their phase velocities are matched [Oka06]. At different core designs in core size or refractive indices of the parallel waveguides, phase matching conditions for each interacting modal pair can only be fulfilled at a certain wavelength. Namely, when the dispersion curves of the two waveguides cross each other [Pes95]. The concept of a 3C[®]-fiber bases on the compensation of the phase difference of one modal pair at a single particular wavelength by an additional phase shift. This phase shift is provided by rotating one of the waveguides around the other waveguide and the corresponding accumulation of different amounts of angular momentum of the modes [All92; Bet36]. Due to the helical side core in 3C[®]-fibers, the differences in β can be adjusted [Liu07a] and groups of mode-coupling resonances occur, which are equally separated by the helix rotation rate $K = 2\pi/\Lambda$ [Ma11b]. These resonances were experimentally measured in the spectral domain of a broadband super-continuum laser source after a 1.5 m-long passive 3C[®]-fiber [Ma11b] and verify the compensation of the phase-velocity mismatch by angular momentum differences. Also for balancing the linear momentum, such an interaction is referred as quasi-phase-matching (QPM) [Ma11a]. The QPM is reflected by the fact that phase matching of HOMs between the signal and the side core of 3C[®]-fibers occurs, which results in high losses for selected modes [Liu07b]. In terms of a physically intuitive picture, the HOMs are "pulled" out of the signal core, so that a single-mode operation in the signal core can be realized.

Traditional cylindrical step-index fibers exhibit an independent rotational and linear translational symmetry due to their fundamental cylindrical fiber design. The helical-symmetry of 3C[®]-fibers is not degenerate anymore and the rotational and linear translational symmetry are coupled [Ma11a]. Cause of the broken degeneracy, only modes that are simultaneously invariant to translation along and rotation around the axis can interact with each other [Kar13]. Correspondingly, the modal field vectors distribute and rotate at the same time and complete a full rotation within each oscillation. Fig. 2.6 presents the evolution of the circular polarized electric field with such a modal field vector distribution. Ma et al. called the rotation of the simultaneously propagating modal field spin angular momentum (SAM) [Ma11a], which is directly associated with the circular polarization of the light. Thereby, the amplitude of the electric field on the z-axis leads to

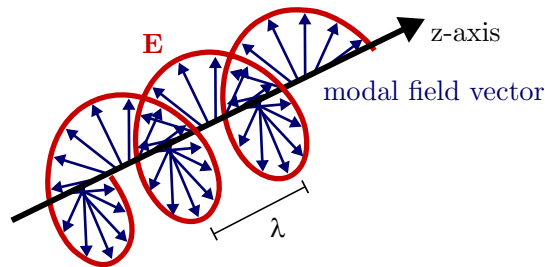


Figure 2.6: Visualization of the spin optical angular momentum (SAM) with the modes wavelength in fiber's propagation z-axis and the electric field vector \mathbf{E} corresponding to a circular polarized field in a Cartesian coordinate system according to [Ma11a].

the 'optical vortex' [Bas95; Nye74].

On the other hand, the rotation and propagation of the scalar distribution of the modal field at the same time corresponds to the physical picture of the simultaneous rotating and propagating phase front of the electric field, which is called orbital angular momentum (OAM) [Ma11a]. The analogous evolution of OAM is visualized in Fig. 2.7. The wavefront described as helical modes consists of $|m|$ interwoven surfaces in the x-y-plane so that the azimuthal phase rotates $|m|$ times 2π around the optical vortex [Baz90; Mar06], where the integer m is called orbital helicity of the beam [Mar06]. Consequently, OAM can be understood as the quantized z-component of angular momentum of each photon associated with a helical mode given by $m\hbar$ [All92].

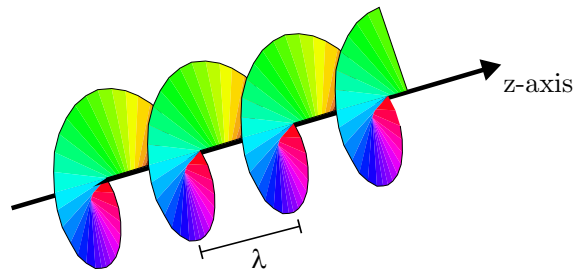


Figure 2.7: Visualization of the orbital optical angular momentum (OAM) with the modes wavelength in fiber's propagation z-axis and the electric field vector \mathbf{E} corresponding to the phase front of the electric field rotates and propagates at the same time according to [Ma11a]. The azimuthal phase completes a full 2π rotation in the transverse plane.

In the following, a more intuitive and physical picture will be introduced of how the QPM is achieved using LP-modes carrying OAM [Ma11a]. According to this, a fundamental mode LP_{01} will be assumed in the signal core and a LP_{11} -mode in the side core. Withal, the quantum number of OAM is directly connected to the mode number $|l|$ of the $LP_{||m}$ -mode, so that for example the LP_{01} -mode carries an OAM with $l=0$ and $l=\pm 1$ for the LP_{11} -mode. The evolution of the phase front is visualized in Fig. 2.8 and Fig. 2.9 with two different conditions at a matched and unmatched phase-velocity. In Fig. 2.8, a $3C^{\circ}$ -fiber is illustrated, where the phase velocities are completely matched between the modal field of the LP_{01} -mode in the core and the modal field of the LP_{11} -mode in the side core. Hence, the phase front reproduces itself after each optical cycle. At different spatial positions on the fiber, the modal field distributions are exactly the same due to the identical phase velocity. However, Ma et al. presented that the overlap integral with the boundary condition of $\beta_{LP_{01}} - \beta_{LP_{11}} = 0$ between the both modal fields is not equal and varies over different angles as shown in Fig. 2.8 [Ma11a]. In spite of an identical phase velocity, the relative phase shift among the modes changes with propagation by the relative rotation between the signal and side core. Therefore, the principle of a phase matching is not fulfilled.

In Fig. 2.9, a concept is illustrated, where the phase velocities are not matched between the signal and side core. However, the phase mismatch between $\beta_{LP_{01}}$ and $\beta_{LP_{11}}$ can be balanced by the correct rotation velocity of the side core helix Λ_{helix} . Comparable to Fig. 2.8, the evolution of the modal field distribution of the individual modes is visualized at

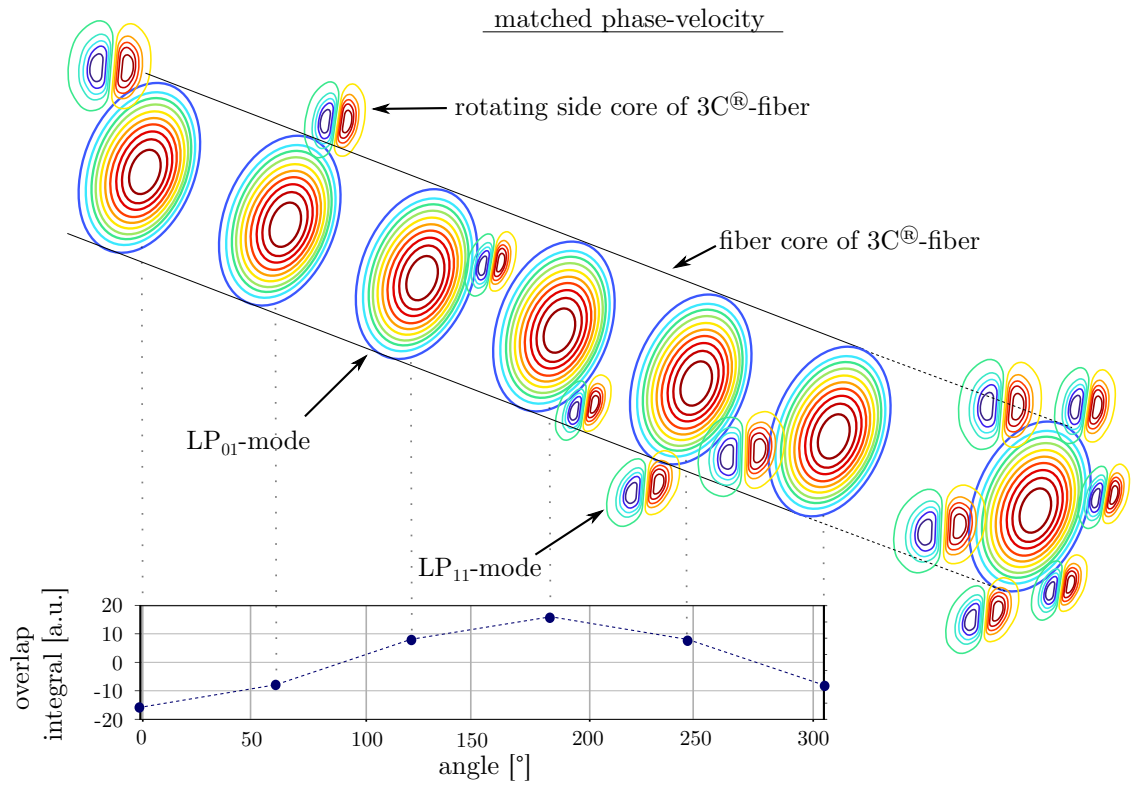


Figure 2.8: Simplified physical illustration in a case of matched phase-velocity between the LP₀₁- and the LP₁₁-mode in a 3C[®]-fiber. The plot presents the corresponding overlap integral of the modes at different rotation angles.

different spatial positions on the fiber. In contrast to the previous concept, the modal distribution of the LP₁₁-mode in the side core exhibits an OAM of $+\hbar$ or $-\hbar$ [Ma11a]. The corresponding overlap integral between the modes considering the boundary conditions of $\beta_{\text{LP}_{01}} - \beta_{\text{LP}_{11}} = A_{\text{helix}}$ is constant (see Fig. 2.9) and the condition of phase matching is fulfilled.

It can be summarized that for an efficient interaction of the signal and the side core in 3C[®]-fibers, the 3C[®]-eigenmodes should be equal to the angular momentum and the QPM can be achieved due to an angular momentum compensation [Ma11a].

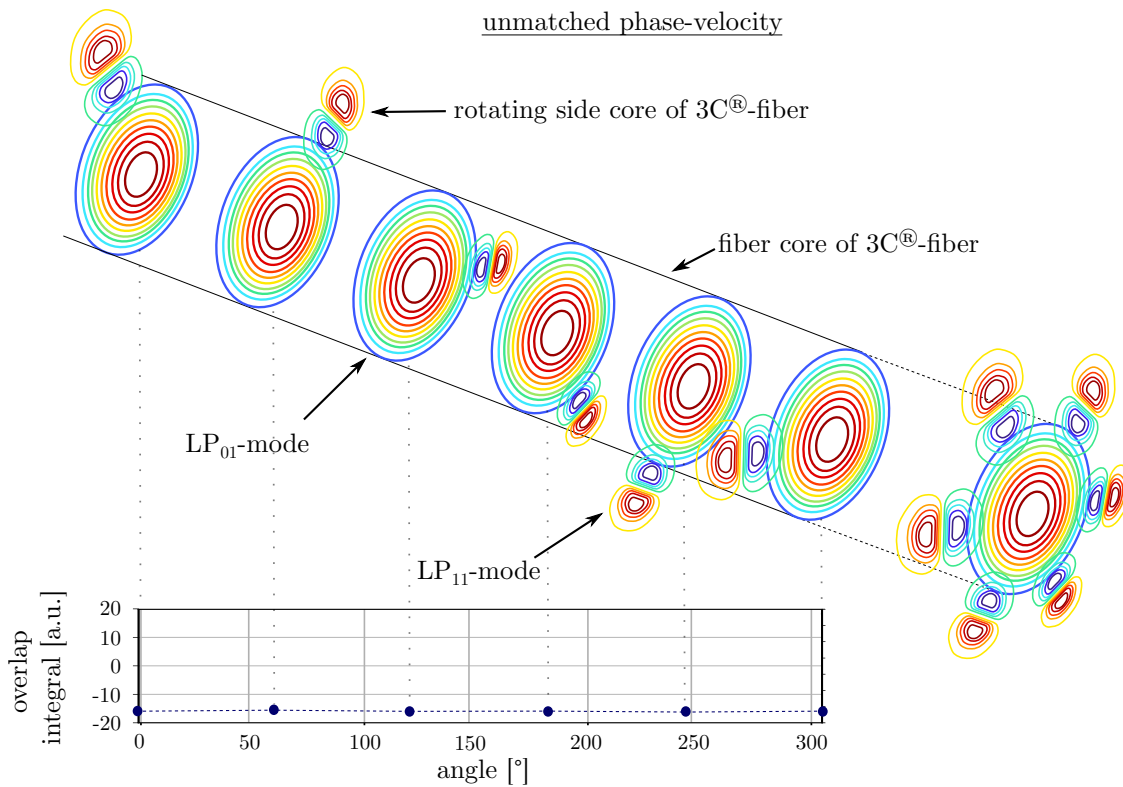


Figure 2.9: Simplified physical illustration of QPM in a case of unmatched phase-velocity between the LP₀₁- and the LP₁₁-mode in a 3C[®]-fiber. The plot presents the corresponding constant overlap integral of the modes at different rotation angles.

2.3.2 3C[®]-fibers in fiber amplifiers architectures

The implementation of the promising 3C[®]-fibers in fiber amplifier systems was a logical conclusion to overcome current power scaling limitations. For classification of this work in the scientific context, laser systems based on this fiber type are presented below. In general, these differ in systems in CW and in pulsed operation, but so far exclusively in the wavelength range around 1 μm .

The effect of chirality of guided waves in chiral optical fibers was already examined by Qiu and Lu in 1994 [Qiu94]. However, these investigations are not directly related to the innovation of 3C[®]-fibers. The first experimental investigations with 3C[®]-fibers were done by Liu et al. in 2007 [Liu07b]. Here, the single-mode guidance properties were demonstrated at 1064 nm and 1550 nm with a fiber sample, but not in a laser or amplifier system. The first fiber laser system based on a pulsed amplifier architecture using a Yb-doped 3C[®]-fiber was demonstrated by Liu et al. again in 2009, where an average power above 100 W with a pulse duration of 10 ns was achieved in a pure single-mode operation [Liu09b]. Further power scaling experiments of this fiber-based laser up to an optical power level of 250 W were shown by Huang et al. already in the same year [Hua09]. In the following years, several further publications with 34 μm 3C[®]-fibers were published in pulsed-operated laser systems

[Che10; Lef13; Lef11; McC14]. Laser or amplifier designs in CW operation have not been investigated until 2013 due to the missing optical applications in industry or research. In context of the development of laser sources for GWDs, Karow examined the performance of a MOPA system using a 3C[®]-fiber [Kar13]. At an output power level of 230 W, the amplifier system exhibited a TEM₀₀-mode content of ~80% and was limited by transverse mode instabilities. This amplifier system was free-space pumped by fiber-coupled laser diodes at a wavelength of 976 nm and used a 3C[®]-fiber prototype sample from the group of Prof. Galvanauskas with 34 μm and 55 μm core diameters. However, this early fiber designs were not optimized during the production process and not suitable for high power operation due to enormous heat contribution. Therefore, the amplifier concept with a 3C[®]-fiber was not appropriate for an application in GWDs at this point. The induced heat distribution inside the 3C[®]-fiber and the impact on modal suppression properties was afterwards investigated by Zhu et al. [Zhu19].

Since 2015, *nLight Inc.* has been producing the 3C[®]-fibers and has always worked on the further development of this fiber type in cooperation with Prof. Galvanauskas. The 3C[®]-fiber samples used in the context of this work are based solely on these improvements and were made available by *nLight Inc.* The impact of these developments on the suitability of 3C[®]-fibers for GWDs is part of this work and will be investigated in the novel MOPA systems in the following chapters.

CHAPTER 3

Impact of Stimulated Brillouin Scattering on Noise Properties of Single-Frequency Signals

Stimulated Brillouin scattering (SBS) is one of the predominant limitations for fiber-based narrowband or single-frequency lasers, amplifiers or passive transmission links. Additionally to the output limitations due to a periodic refractive index modulation along the fiber core, SBS imprints a broadband excess intensity noise on the signal. Such a broadband noise is also a limiting factor for many applications such as telecommunication links, LIDAR or especially gravitational wave detectors. Several theoretical models have been reported to explain the observed excess noise in the transmitted signal: Stokes and anti-Stokes Brillouin scattering process [Hor97] or a conversion from phase to intensity noise [Per99; Zha05]. Hereby, the transition from spontaneous to stimulated Brillouin scattering is directly connected to the Brillouin gain spectrum. The conversion from phase to intensity noise returns to the idea of an asymmetric Brillouin gain spectrum. This chapter demonstrates new and consistent experimental studies, which suggest the phase-to-intensity conversion of the transmitted signal as origin of the excess noise due to such an asymmetric Brillouin gain spectrum. In this context, the results have been published in Ref. [Hoc20a].

In Section 3.1, the general idea and the conceptual understanding of the conversion from phase to intensity noise is described. Therefore, the intuitive illustration of a phasor diagram is introduced for the explanation of the physical phenomenon. The basic idea of this concept is an asymmetric Brillouin gain spectrum. An experimental layout and measurement method to investigate such a gain spectrum is represented in Section 3.2, where a heterodyne measurement technique was chosen. The experimental results of the gain spectra are discussed in Section 3.3. The impact of an asymmetric gain spectrum is directly apparent in the eigenfrequencies of the overall fiber system and will be investigated in the following. In Section 3.4, the reconstruction of the excess intensity noise is theoretically demonstrated and compared with the experimental results.

3.1 Conceptual understanding of the conversion from phase to intensity noise

The modulation of light amplitude can be visualized with a phasor diagram. The graphical interpretation of an amplitude and phase modulation is shown in Fig. 3.1. Here, the carrier (red arrow) as well as sidebands (blue arrows) are represented by rotating vectors on a complex plane. The amplitude of the carrier field is given by the length of the vector, which rotates clockwise with the rate ω . The sideband vectors rotate in opposite directions among themselves with the rotation-frequency of the carrier field. The sum of these three vectors yields a complex vector, where the projection on the real axis represents the modulation of

the amplitude of the light.

Fig. 3.1a) represents the amplitude modulation (AM). The vector sum of the modulated sidebands is always in phase with the carrier field such as the time-dependent projection onto the real axis including the AM. This is depicted to the left of the phasor diagram. In case of a phase modulation (PM) in Fig. 3.1b), the vector sum of the sidebands oscillates at 90° , i.e. $\pi/2$, phase shift with respect to the carrier. Thus, the resulting modulated oscillation vector has the same length as the carrier field vector. The subsequent pure-PM oscillation without any AM is depicted to the right of the diagram.

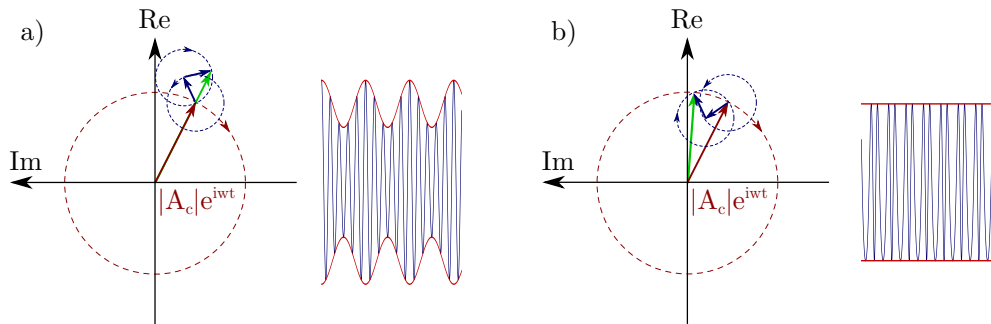


Figure 3.1: Phasor diagram for amplitude (a) and phase (b) modulated light with the carrier field (red arrow) and the sideband vectors (blue arrows). The resulting modulated oscillation is shown in a green arrow. The time-dependent projection of the electric field is depicted to the right of the corresponding phasor diagram.

The idea of a conversion from phase to intensity noise based on an asymmetric Brillouin gain or an asymmetric loss spectrum for the transmitted signal has first been reported by Zhang and Phillips [Zha05]. Numerical simulations of the overlap between acoustic and optical modes have provided a potential explanation of such an asymmetric gain spectrum [Per99].

Fig. 3.2 presents the impact of an asymmetric Brillouin gain spectrum and the resulting asymmetric phase shift on the modulated oscillation vector of the light for a pure input PM. In the case of a symmetric Brillouin gain spectrum, the sidebands of the transmitted signal, inherently present due to the frequency noise of the laser source, experience an identical phase shift with opposite sign. Thus, their vector sum does not change its phase. If now an asymmetric Brillouin gain spectrum with an asymmetric phase distribution is assumed, the sidebands experience a differential loss and different phase shifts. In the sum of the vectors, the modulated oscillation does not have the same length as the carrier. Thus, the resulting electrical field is also modulated in its amplitude now. This induced amplitude modulation scales directly with the phase modulation it was generated from.

In general, assuming the Maxwell wave equations with material equations and nonlinear polarization, SBS is governed by coupled amplitude A_j equations for the pump ($j=p$) and the Stokes wave ($j=s$), such that $|A_j|^2$ represents the power [Agr01]. For example, the evolution of the pump wave is given by:

$$\frac{dA_P}{dz} = -\chi(\nu)|A_S|^2 A_P, \quad (3.1)$$

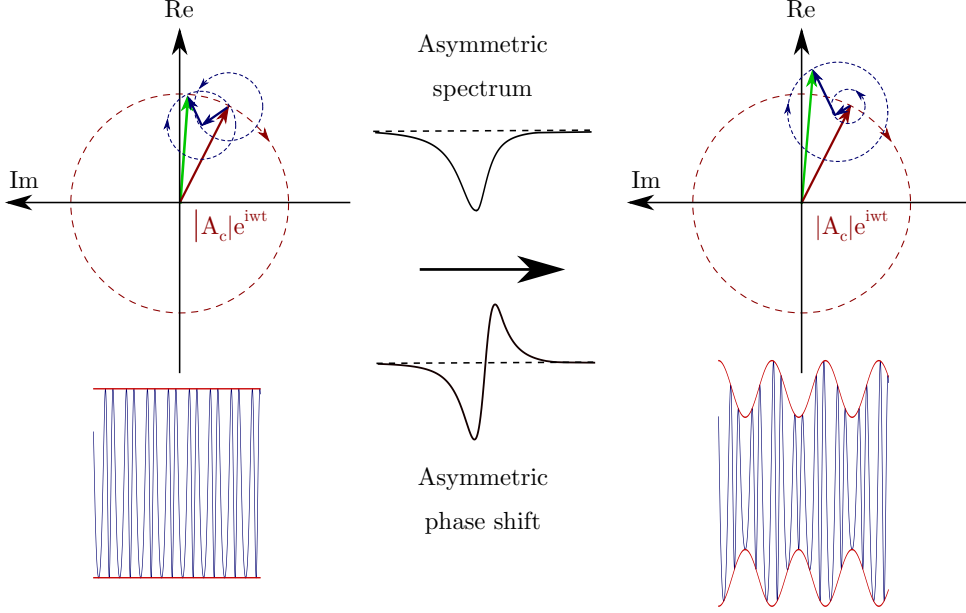


Figure 3.2: Principle of the conversion from phase to intensity noise based on an asymmetric Brillouin loss and a corresponding asymmetric phase shift for the transmitted signal. A symmetric gain or loss spectrum has no influence on the amplitude and the sidebands experience a pure PM. Due to an asymmetric spectrum (right), the sidebands experience a differential loss and phase shift and the pure phase modulation is converted into a mixture of amplitude and phase modulation.

where $\chi(\nu)$ is the frequency-dependent susceptibility. Under steady-state conditions, applicable for a CW pump signal and a spectral pump-linewidth much smaller than the SBS bandwidth, the coupled mode equations can be simplified to the following equations for the power evolution along the fiber [Agr01]:

$$\frac{|A_P|^2}{z} = -g_B(\nu)|A_P|^2|A_S|^2 - \alpha_P|A_P|^2, \quad (3.2)$$

$$-\frac{|A_S|^2}{z} = g_B(\nu)|A_P|^2|A_S|^2 - \alpha_S|A_S|^2 \quad (3.3)$$

with the frequency-dependent Brillouin gain coefficient $g_B(\nu) = -2 \cdot \text{Re}(\chi(\nu))$. For further simplification and due to the short fiber lengths, fiber losses are neglected in the following, i.e. $\alpha_P = \alpha_S = 0$.

Using Eq. (3.1) the frequency-dependent phase shift can be derived as a Hilbert transformation of the real part of the susceptibility $\chi(\nu)$ with the Stokes power P_{Stokes} and the mode field diameter of the fiber core:

$$|A_P(z=L)| = |A_P(z=0)| \cdot e^{\text{Re}(\chi)|A_S|^2 L} \cdot e^{-i\mathcal{H}(\chi)|A_S|^2 L}, \quad (3.4)$$

$$\Phi = \mathcal{H}(\chi) \cdot |A_S|^2 \cdot L = \mathcal{H}(\text{Re}(\chi)) \cdot \frac{P_{\text{Stokes}} \cdot L}{\pi \cdot \text{MFD}^2}. \quad (3.5)$$

It was assumed that the power of the Stokes light $|A_S|^2$ is constant. The Brillouin gain coefficient $g_B(\nu)$ exhibits a frequency dependence, which is assumed here as a modified Lorentzian profile with peak-gain g_{B_0} and the Brillouin frequency shift ν_B :

$$g_B(\nu) = g_{B_0} \cdot \frac{\left(\frac{\Omega_{BS}}{2}\right)^2}{(\nu - \nu_B)^2 + \left(\frac{\Omega_{BS}}{2}\right)^2} \cdot \left(\frac{\nu}{\nu_B}\right)^n. \quad (3.6)$$

The bandwidth Ω_{BS} of the gain spectrum is related to the phonon lifetime $T_{BS} = \Omega_{BS}^{-1}$ of typically < 10 ns [Agr01]. The term $\left(\frac{\nu}{\nu_B}\right)^n$ introduces an asymmetry, where n indicates the level of imbalance ($n = 0$ corresponds to a normal Lorentzian profile).

3.2 Experimental layout and measurement method

As a test signal, a single-frequency non-planar ring oscillator (NPRO, Innolight Mephisto 2000NE, see Fig. 3.3) with a narrow laser linewidth (< 1 kHz) was used. The NPRO emitted 2 W output power of continuous-wave at 1064 nm and is a common laser system for the challenging application of GWDs. The MOPA system consisted of a free space part and an amplification stage based on a rare-earth doped fiber. A 3 m polarization-maintaining large mode-area ytterbium doped fiber (Nufern, PLMA-YDF-10/125) allowed an amplification of the NPRO test signal up to 20 W preserving its narrow linewidth and further optical properties. The pump light for the amplification was supplied by two high-power laser diodes (II-VI, BMU30-975-01-R02) emitting at 976 nm at a maximum power of 30 W and was injected into the cladding of the active fiber via a pump combiner (PC). Any residual pump light of the counter-propagating configuration was removed by an in-house fabricated cladding light stripper (CLS) [Wys18]. The detailed description and development of such fiber-based components in 3C[®]-fibers is also part of the following chapters.

The SBS signal was generated in a single-mode fiber (*Raman*-fiber from OFS Fitel) with a measured 4 μm core diameter and different fiber lengths (2.5 m, 5 m, 7.5 m and 20 m).

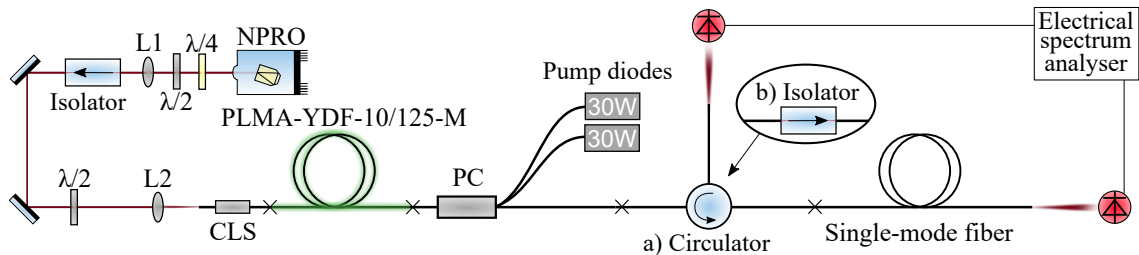


Figure 3.3: Experimental setup for intensity noise measurements of the transmitted light above the SBS threshold. The system consisted of an NPRO for the signal beam, a monolithic fiber amplifier and a single-mode fiber for the generation of SBS. The connection between the MOPA stage and the single-mode fiber was either a high power fiber isolator (at higher signal power b)) or a circulator (at lower signal power a)) to measure the Brillouin gain spectrum. CLS: cladding light stripper, PC: pump combiner, L_i : lens. Splices are represented by x.

Due to the small effective mode area of the fiber ($30\text{-}50\ \mu\text{m}^2$), nonlinear effects already set in at lower power levels. Any potential back reflection into the fiber amplifier was suppressed by a circulator (see Fig. 3.3 a)) or a high-power fiber isolator (see Fig. 3.3 b)). The basic structure of a circulator enabled the advantage to couple out the returning light into another fiber port and to investigate this port separately. After the amplifier system, the noise of the transmitted signal was measured with an InGaAs-photodiode (Thorlabs, PDA10CF-EC) with a bandwidth of 150 MHz and was analyzed with an electrical spectrum analyzer (Agilent, E4440).

The SBS signal and the backwards propagating Rayleigh scattering of the signal beat together and enable a heterodyne detection of the gain spectrum in a monolithic fiber system by a fast amplified photodiode with a bandwidth of 45 GHz (Newport Corp. 1014 and Newport Corp. 1421) at the output port of the circulator.

3.3 Experimental results

Using the presented measurement method of Section 3.2, the Brillouin gain spectrum was investigated. Fig. 3.4a) presents such a measured gain profile at a frequency shift of around $\nu_B = 14.7\ \text{GHz}$ after 20 m of single-mode fiber. Instead of a symmetric Lorentzian profile, the measured profile exhibits an asymmetric characteristic, which can be expressed by $n = 210$ (see Eq. (3.6)) and a bandwidth of $\Omega_{BS} = 21\ \text{MHz}$ based on a corresponding fit (Fig. 3.4a, dashed red). In addition, further asymmetric broadening can be identified at different signal power (see Fig. 3.4 b)).

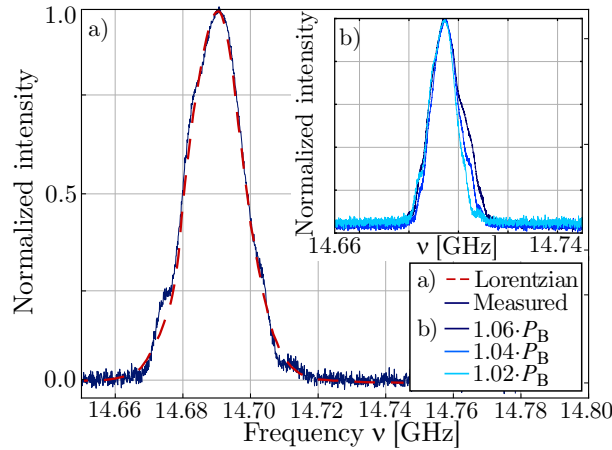


Figure 3.4: Measured stimulated Brillouin scattering gain spectrum: a) Spectrum of a 20 m single-mode fiber at a frequency shift of around 14.7 GHz and a fitted asymmetric Lorentzian profile. b) Gain profile at different signal power levels with a 20 m single-mode fiber.

The measured intensity noise of the amplified NPRO signal after the single-mode fiber for a fiber length of 20 m is shown in Fig. 3.5. The measurement below the SBS threshold P_B is shown in black. An increase of the pump power above the SBS threshold resulted in a characteristic excess intensity noise up to 50 MHz. Additionally, above a certain signal

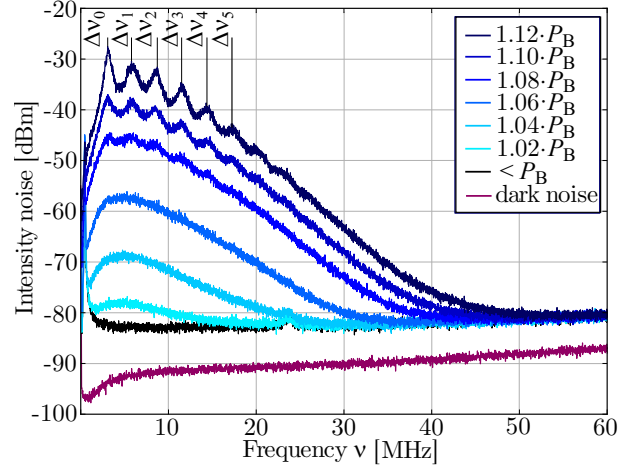


Figure 3.5: Intensity noise spectrum of the transmitted signal below and above the SBS threshold P_B for a fiber length of 20 m. The differences of the eigenfrequencies are marked as $\Delta\nu_i$.

power ($> 1.10 \cdot P_B$) corresponding resonances occurred in the intensity noise spectrum. Due to small back reflections at the fiber end facets, the setup corresponds to a resonator with a low Q factor. One would assume that the resonator eigenfrequencies are given by the fiber length and the refractive index of the optical medium [Sté02]. The resonances in the intensity noise spectrum correspond to the beating between the carrier and the eigenfrequencies or between the upper and lower eigenfrequencies among themselves. However, the measured resonances do not match with the corresponding fiber length, i.e. $\Delta\nu_0 = 2.9$ MHz would correspond to a fiber length of 35 m instead of 20 m (see Fig. 3.5). Previous explanations by modulation instabilities [Tak95] can not explain this behavior for two reasons: On the one hand, modulation instabilities only occur in the intensity noise if they are also visible in the gain spectrum and on the other hand, the absolute frequency separation $\Delta\nu_i$ will always be larger than $2c/nL$ [Tak95], but here it decreases with increasing output power.

Here, the total phase shift of one round trip Φ_{RT} with the refractive index n_0 of the fiber is given by:

$$\Phi_{RT}(\nu) = \frac{4\pi n_0 L}{c} \cdot \nu + \mathcal{H}(g_B(\nu)) \cdot \frac{P_{Stokes} \cdot L}{\pi \cdot MFD^2}, \quad (3.7)$$

where the second term is the additional phase shift due to the SBS effect. The Stokes power P_{Stokes} is estimated via the missing output power in the transmitted signal.

Fig. 3.6 illustrates the resulting effect of the phase shift of the round trip without (red dashed line) and with an additional phase shift due to SBS (blue line). A phase shift of 2π corresponds exactly to the distance between two longitudinal modes or an equivalent change of the frequency $\Delta\nu_i$, where the change is consistent with $\Delta\nu_i = \nu(\Phi_{RT} = (n + 1)2\pi) - \nu(\Phi_{RT} = n2\pi)$ with $n = 0, 1, 2, 3, \dots$

The insert in Fig. 3.6 visualizes the case for the shifted round trip of 2π and 4π with a corresponding eigenfrequency of 2.8 MHz and 5.7 MHz.

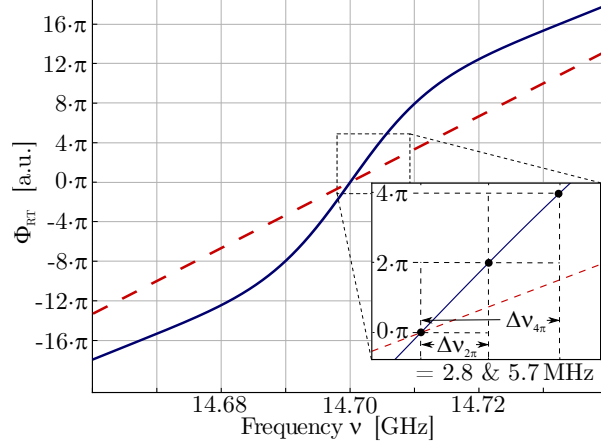


Figure 3.6: Shift of the phase of the round trip without (red dashed line) and with an additional phase shift due to SBS (blue line). The insert visualizes the case for the shifted round trip of 2π and 4π with a corresponding eigenfrequency of 2.8 MHz and 5.7 MHz.

The measured eigenfrequencies in the intensity noise spectrum can be well predicted by Eq. (3.7). Table 3.1 gives an overview of the measured and calculated resonances at different fiber lengths:

Table 3.1: Measured and calculated resonator eigenfrequencies at different fiber lengths

Fiber length	$\Delta\nu_{2\pi}$ [MHz]	Eq.(3.7) [MHz]	$\Delta\nu_{4\pi}$ [MHz]	Eq.(3.7) [MHz]
(2.5 ± 0.2) m	6.6	(6.9 ± 0.7)	19.3	(19.4 ± 3.1)
(5.0 ± 0.2) m	5.8	(6.0 ± 0.6)	15.2	(14.5 ± 2.1)
(7.5 ± 0.2) m	4.9	(5.0 ± 0.5)	12.3	(11.2 ± 1.7)
(20 ± 0.2) m	2.9	(2.8 ± 0.4)	5.8	(5.7 ± 1.1)

The results confirm the parameters of the Lorentzian profile fit (see Fig. 3.4), where the uncertainties are determined especially by the accuracy of the length of the single-mode fiber.

Additionally, the evolution of the resonator eigenfrequencies at 15 MHz is presented in Fig. 3.7 in detail for a fiber length of 20 m. Due to the asymmetric gain profile and the corresponding phase shift, the beat frequencies between the upper and lower eigenfrequencies with the carrier are not equal, which becomes noticeable in a splitting of the resonator peaks in the intensity noise spectrum. Consequently, these results are a further first and new experimental evidence for an asymmetric gain profile.

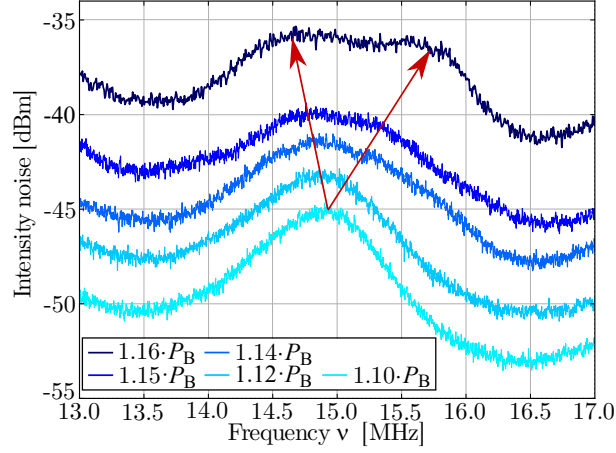


Figure 3.7: Intensity noise of the transmitted signal above the SBS threshold P_B in a frequency range from 13 to 17 MHz. The splitting of the resonances expressed by the red arrows indicates an asymmetric gain profile.

3.4 Reconstruction of the low-frequency excess intensity noise

In the following it will be demonstrated that the results of the fitted asymmetric SBS gain profile can be used to reconstruct the characteristic shape of the excess intensity noise quite well. Behind the fiber the entire electric field E_{total} can be represented by:

$$E_{\text{total}}(t) = |A_C|^{\text{in}} \cdot e^{i\omega t} + i \cdot |A_S|^{\text{in}} \cdot g_B^+ \cdot e^{i(\omega+\omega_B)t} \cdot e^{i\phi^+} + i \cdot |A_S|^{\text{in}} \cdot g_B^- \cdot e^{i(\omega-\omega_B)t} \cdot e^{i\phi^-}, \quad (3.8)$$

where the term $|A_C|^{\text{in}} \cdot e^{i\omega t}$ describes the carrier and the other two terms are the sidebands with frequency shifts of $\pm\omega_B$ corresponding to Fig. 3.2. The gain or loss due to the SBS spectrum is described by g_B^+ and g_B^- and the phase shift by ϕ^+ and ϕ^- .

In addition, several assumptions have been made in the following. The frequency noise of the NPRO shows a $1/\nu$ -characteristic [NPRO] and only the contribution of the beating of the sidebands with the carrier is significant at MHz-frequencies, because the sideband-sideband interaction is too weak and will not be considered further. Then, it follows for the intensity:

$$\begin{aligned} I(t) &= E_{\text{total}} E_{\text{total}}^* & (3.9) \\ &= 1 + 2|A_S|^2 + 2|A_S|g_B^+ \cos(\omega_B t + \phi^+) - 2|A_S|g_B^- \cos(-\omega_B t + \phi^-) \\ &= 1 + 2|A_S|^2 + 2|A_S| \left[g_B^+ \sin\left(\omega_B t + \phi^+ + \frac{\pi}{2}\right) - g_B^- \sin\left(\omega_B t - \phi^- + \frac{\pi}{2}\right) \right] \\ &= 1 + 2|A_S|^2 + 2|A_S| \sqrt{(g_B^+)^2 + (g_B^-)^2} - 2g_B^+ g_B^- \cos(\phi^+ + \phi^-) \cdot \sin(\omega_B t), \end{aligned} \quad (3.10)$$

where the amplitude of the sidebands is scaled with the amplitude of the carrier. In the case of a symmetric gain spectrum, where $g_B^+ = g_B^-$ and $\phi^+ = -\phi^-$, Eq. (3.10) shows no AM as expected.

The shape of the excess intensity noise is then given by the AC term of Eq. (3.10) with a

scale factor κ (to be fitted) and the $1/\nu$ -frequency noise characteristic of the NPRO:

$$M(\nu) = \sqrt{(g_B^+)^2 + (g_B^-)^2 - 2g_B^+g_B^- \cos(\Omega)} \cdot \frac{\kappa}{\nu} \quad (3.11)$$

with $\Omega = \phi^+ + \phi^-$.

Fig. 3.8 presents three intensity noise measurements at different signal power levels above the SBS threshold P_B (blue) and one measurement below the threshold (black) on a logarithmic frequency scale. Similar to Fig. 3.5, the spectrum exhibits an increase of the broadband noise in the MHz-frequency range up to 50 MHz with increasing output power. At lower frequencies the NPRO relaxation peak at 450 kHz overlaps the broadband noise and at higher frequencies, the measurement is shot noise limited. For the three measurements and the corresponding fitted Lorentzian profile (see Fig. 3.4(b)) the model $M(\nu)$ was calculated analytically with Eq. (3.10). The fit was only scaled according to the measured noise level with the parameter κ . For more asymmetric profiles, the influence of the differential phase shift distribution increases, so that in a regime of 10 MHz an excess noise can be observed. This regime correlates with the frequency range of the maximum of the phase shift. The frequency range from 1 to 10 MHz shows a discrepancy between the model and the experimental data. One possible explanation is the small phase difference around the inflection point near the carrier of the phase shift and the corresponding low intensity modulation (see Fig. 3.6). Another more flexible model, like a modified Gaussian fit, could optimize the results. In summary, Fig. 3.8 shows the reconstruction of the characteristic shape of the excess intensity noise by SBS for the first time.

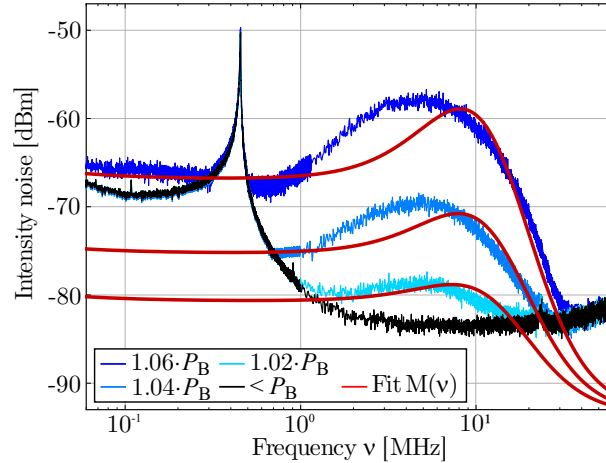


Figure 3.8: Intensity noise spectrum of the transmitted light above and below the SBS threshold P_B . A model of the noise for three measurements based on an asymmetric Lorentzian gain spectrum and a conversion from phase to intensity noise is shown in red.

3.5 Conclusion

Due to the limiting properties of SBS for fiber laser or amplifier systems, the knowledge of the excess intensity noise above the SBS threshold conduces to the comprehension of noise properties of such laser systems and can be useful for further laser stabilization methods. Therefore, this chapter focused on the impact of the excess broadband intensity noise by the conversion from phase to intensity noise. The basis of this physical effect is an asymmetric Brillouin gain spectrum.

Using a heterodyne measurement technique, an asymmetric gain spectrum was experimentally observed and an assumed modified Lorentzian equation was used to describe the measured profile. Other measurements at a fiber amplifier system at 1.5 μm showed similar results, which have not been further investigated yet. Based on these results and the parameter of the mathematical fit, the total phase shift of one round trip in the SM-fiber system was calculated to explain the observed eigenfrequencies in the intensity noise spectrum. Only through the addition of a phase shift term caused by SBS, the resonator eigenfrequencies can be mathematically described correctly. For the verification, the experiments were repeated with different fiber lengths in the setup. Besides, a splitting of the resonator peaks in the intensity noise spectrum was observed and also explained by the additional phase shift due to an asymmetric Lorentzian profile. This theoretical model was verified by experimental investigations of intensity noise spectra at different power levels above the SBS threshold. These new and consistent results suggest the conversion from phase to intensity noise and confirm the parameter of the fitted and modified Lorentzian profile. In the scientific context, the presented measurements continue the idea of Peral and Zhang [Per99; Zha05] and open up a new perspective on the impact of the Brillouin gain spectrum to the nonlinear effect of SBS.

For the first time, the shape of the excess intensity noise was reconstructed based on the parameter of the asymmetric Brillouin gain spectrum. At different power levels above the SBS threshold, the gain spectra were measured and the fitted profile was used to describe the characteristic shape of the intensity noise.

For fiber-based narrowband or single-frequency lasers, amplifiers or passive transmission links, SBS is still one of the predominant limitations for power scaling or low-noise applications. Therefore, the investigations and understanding of this nonlinear effect has a large impact for optimizing future laser or amplifier systems based on fiber architectures and the increase of the SBS threshold.

A comparatively simple method to increase the threshold is described in more detail in the following Chapters 4, 5 and 6 with the use of 3C[®]-fibers with enlarged effective mode areas.

CHAPTER 4

Integrated Optical Components in 3C[®]-Fibers

In the recent decades, the development of fiber laser and fiber-based MOPA systems has proven to be a promising laser technology to fulfill the special requirements for the steadily growing fields of applications. Especially, high-power fiber laser systems can benefit from the realization of compact and efficient monolithic architectures. Therefore, the effort of integrating all-fiber components into such systems has been increased more and more [Mac07; The12b].

Optical fiber components can be broadly classified depending on the area of application. For telecommunication links for example, efficient elements such as de- and multiplexer are mainly used. This work relates exclusively to the development of fiber-based components required for high-power MOPA systems. The manufacturing process of such units with standard fibers has been continuously improved in recent years. However, the use of new fiber types in the existing process is associated with a large effort for adapting the manufacturing parameters. And this effort already relates to standard fibers and is even larger when using specialty fibers. However, these specialty fibers open up new possibilities of power scaling in high-power laser systems. The common PCFs are only partially suitable for the construction of fiber-based components due to the micro-structured air holes inside this fiber type. The air holes would collapse during the manufacturing process and negatively affect the guidance properties. Here, specialty fiber geometries based on an all-solid design exhibit a significant advantage. A promising specialty fiber concept in this context with an enlarged MFD is the mentioned 3C[®]-fiber.

For the combination of the advantages of the 3C[®]-fibers for further power scaling and compact, reliable and efficient all-fiber amplifier systems, the development of integrated optical components in 3C[®]-fibers is essential. Such devices do not exist yet and are presented in this work for the first time. The following chapter describes the development in more detail.

In addition to the manufacturing process, the characterization of optical components is important for the later laser performance. Therefore, Section 4.1 presents an all-fiber characterization concept of an S²-imaging technique with the potential of real-time measurements. Based on this technique, the used 3C[®]-fibers and components were investigated. In Section 4.2, a device to adapt the mode area from a SM-fiber to a 3C[®]-fiber is introduced with the development of a mode field adapter. Further components integrated in 3C[®]-fibers such as end caps and cladding light strippers are presented in Section 4.3 and Section 4.4.

For further power scaling, a highly integrated signal and pump combiner is the key

component. Common fused tapered fiber bundles are not suitable so that the side-pumping technique was chosen for the manufacturing process with 3C[®]-fibers. In Section 4.5, the development of such a device is introduced and a detailed investigation of the combiner performance is shown. Further improvements of the combiner are also discussed in the following. These details were also published in Ref. [Hoc21].

4.1 Characterization concept of an S²-imaging technique

During the development of optical components for optical systems such as all-fiber amplifiers, it is essential to characterize single components as well as the complete system. Therefore, corresponding measurement techniques are necessary, which provide statements about the quality of each manufactured component. An essential point when describing the quality of a component is the beam quality of the light after propagating through the corresponding device.

According to ISO Standard 11146 [ISO11146], a common measure of the beam quality of a laser beam is called M^2 factor [Sie93]. The parameter is defined as the beam parameter product divided by λ/π :

$$M^2 = \frac{\pi}{\lambda} \cdot \theta \omega_0, \quad (4.1)$$

where θ is the half-angle beam divergence and ω_0 the beam radius at the beam waist. As the M^2 factor compares the laser beam with a Gaussian beam, a diffraction-limited beam has an M^2 factor of 1. In a physical picture, the M^2 factor limits the degree of the possibility of focusing a laser beam for a given beam divergence angle. However, the factor does not provide any information about the fundamental mode content of the laser beam and even with a large amount of optical power contained in HOMs to be as high as 30%, it is still possible to achieve a low factor of M^2 [Wie07; Yod06]. Pointing instabilities in the far field by changing the relative phase of the modes are not determined by the M^2 factor either.

Therefore, Nicholson et al. developed an advanced measurement technique capable of simultaneously imaging multiple, coherent, HOMs propagating in large mode area fibers [Nic08]. The method spatially and spectrally (S² imaging) resolves the interference of various fiber modes due to different group velocities.

The S² technique is based on the idea that the spectral interference pattern via the different group delay, as well as the spatial interference pattern between the fundamental mode and HOMs inside the fiber, can be identified by a broadband source propagating through the fiber. These two physical properties enable the simultaneous imaging of multiple modes propagating in the fiber.

The conceptual setup of a S² imaging to determine the propagating HOMs content in fibers is shown in Fig. 4.1(a). For this, a broadband light source is launched into a fiber under test, usually with a large mode area. After the fiber, the laser beam is collimated with an appropriate lens and imaged onto a cleaved single-mode fiber end facet, which is directly connected with an optical spectrum analyzer (OSA). For the implementation of a spatial resolution, the single-mode fiber is moved on a grid pattern at different x and

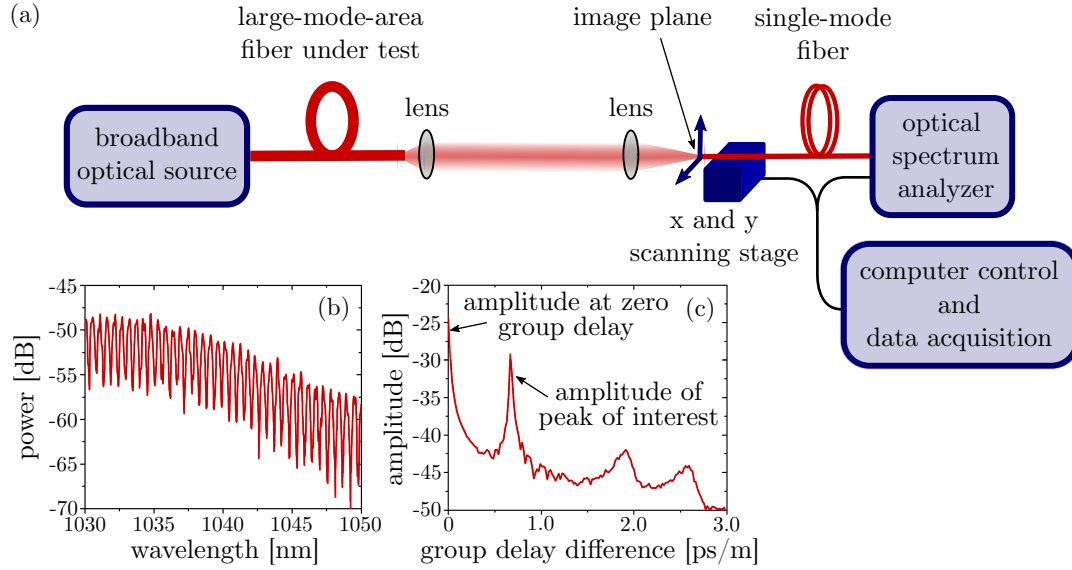


Figure 4.1: (a) Visualization of a S² imaging setup. (b) Typical optical spectrum measured at an arbitrary (x,y) point and (c) the Fourier transform of the optical spectrum by (b) showing multiple beat frequencies according to Ref. [Nic08].

y positions. At each (x,y) position of the beam profile, an optical spectrum is measured, which is plotted as an example in Fig. 4.1(b). The optical spectrum exhibits a spectral interference pattern, when two different modes overlap spatially in the fiber under test at that (x,y) point. Due to the Fourier transform, the optical spectrum is converted into the frequency domain, where the x-axis of the Fourier transform is scaled by the fiber length to obtain the group delay difference between the modes in the unit of ps/m [Nic08]. The corresponding Fourier transform of the optical spectrum is shown in Fig. 4.1(c) and includes several different beat frequencies at particular group delay differences.

The ratio of the power level P_1 and P_2 of two various modes is defined as the multi-path-interference (MPI) [Nic08]

$$\text{MPI} = 10 \cdot \log \frac{P_2}{P_1}. \quad (4.2)$$

For the calculation of the relative power levels of the modes, Nicholson et al. assumed two modes with spatially and frequency dependent amplitudes $A_1(x,y,\omega)$ and $A_2(x,y,\omega)$ related by a wavelength independent constant $\alpha(x,y)$ [Nic08]. Consequently, the corresponding intensity is

$$I_2(x,y,\omega) = \alpha^2(x,y)I_1(x,y,\omega). \quad (4.3)$$

Based on the assumption that the group delay difference between the modes is independent of the frequency, the spectral intensity resulting from the interference between two modes

can be determined as

$$I(x,y,\omega) = I_1(x,y,\omega) [1 + \alpha^2(x,y) + 2\alpha(x,y) \cos(\tau_b\omega)] \quad (4.4)$$

with the beat frequency τ_b . Based on these considerations, the Fourier transform of the spectral intensity can be described by

$$B(x,y,\tau) = [1 + \alpha^2(x,y)] B_1(x,y,\tau) + \alpha(x,y) [B_1(x,y,\tau - \tau_b) + B_1(x,y,\tau + \tau_b)], \quad (4.5)$$

in which the Fourier transform of the optical spectrum of a single mode is determined by $B(x,y,\tau) = \mathcal{F}\{I_1(x,y,\omega)\}$. Then, the constant α can be calculated by the ratio $R(x,y)$

$$R(x,y) = \frac{B(x,y,\tau = \tau_b)}{B(x,y,\tau = 0)} = \frac{\alpha(x,y)}{1 + \alpha^2(x,y)} \quad (4.6)$$

of the amplitude of the Fourier transform of the spectral intensity at the group delay of interest at a given point (x,y) with the amplitude without any group delay. Consequently, the constant α can simply be expressed as

$$\alpha(x,y) = \frac{1 - \sqrt{1 - 4R^2(x,y)}}{2R(x,y)}. \quad (4.7)$$

The wavelength range of the measured optical spectrum is significantly larger than the beat frequency, so that the total intensity of two modes measured in the OSA at a given (x,y) point reflects the incoherent sum of the individual modes intensities. With the total integrated intensity $I_T(x,y) = I_1(x,y) + I_2(x,y)$ at a given (x,y) point, the intensity of a single mode is given by [Nic08]

$$I_1(x,y) = I_T(x,y) \frac{1}{1 + \alpha^2(x,y)}, \quad \text{respectively} \quad (4.8)$$

$$I_2(x,y) = I_T(x,y) \frac{\alpha^2(x,y)}{1 + \alpha^2(x,y)}. \quad (4.9)$$

Accordingly, the calculations of Eq. 4.7, 4.8 and 4.9 must be executed for all measured (x,y) points, so that finally the total can be calculated from

$$\text{MPI} = 10 \cdot \log \left[\frac{\int \int I_2(x,y) dx dy}{\int \int I_1(x,y) dx dy} \right]. \quad (4.10)$$

This measurement technique is a meaningful alternative method for characterizing propagating modes in large mode area fibers and determine the beam quality, where the measurement process can be fully automated. However, the process itself requires a certain amount of time due to the measurement of individual optical spectra at each (x,y) point. Depending on the spatial resolution of the x-y-stage, but also on the spectral resolution of the OSA, the total scanning process of a beam profile using a broadband input spectrum requires up to several minutes. The fastest commercial S² imaging system (FMA-100) is

offered by *Interfiber Analysis*, which complements the measurement in < 1 minute [FMA]. Usually, it is desirable to verify the beam quality in real-time. For example, the manufacturing process of optical components can profit from a faster evaluation of the beam quality, so that adjustments can be directly integrate during manufacture. Therefore, in the following Section 4.1.1 the concept and the experimental layout of an advanced S^2 imaging technique will be introduced.

4.1.1 Experimental layout

A variety of applications would benefit from the ability of S^2 measurements in real time. In 2016, D. R. Gray et al. introduced the concept of an implementation of the S^2 technique for the first time, which has an increased repetition speed enabling the ability to measure the mode content in real time [Gra16]. In contrast to used broadband optical source with a fixed specified spectral bandwidth, where the temporally (slow) change in the spatial position is determined experimentally, this concept is based on the spectral variation of a tunable laser source (TLS) and a charged coupled device (CCD) or a common complementary metal–oxide–semiconductor (CMOS). The TLS with an optical bandwidth $< \tau_b$ is scanned across the target wavelength range, where at each spectral adjustment of the TLS a 2D spatial intensity profile is captured by a CMOS sensor as a function of wavelength (see Fig. 4.2). The evaluation of the data does not differ between the two methods. Gray et al. have used a commercial TLS (Agilent 81940A) and the experience of the telecommunications branch at $1.5 \mu\text{m}$ range for the development of an advanced S^2 technique [Gra16]. This device is based on typical known nonlinear effects, which are commonly used in such devices.

In order to investigate the properties of the propagating light at the target wavelength

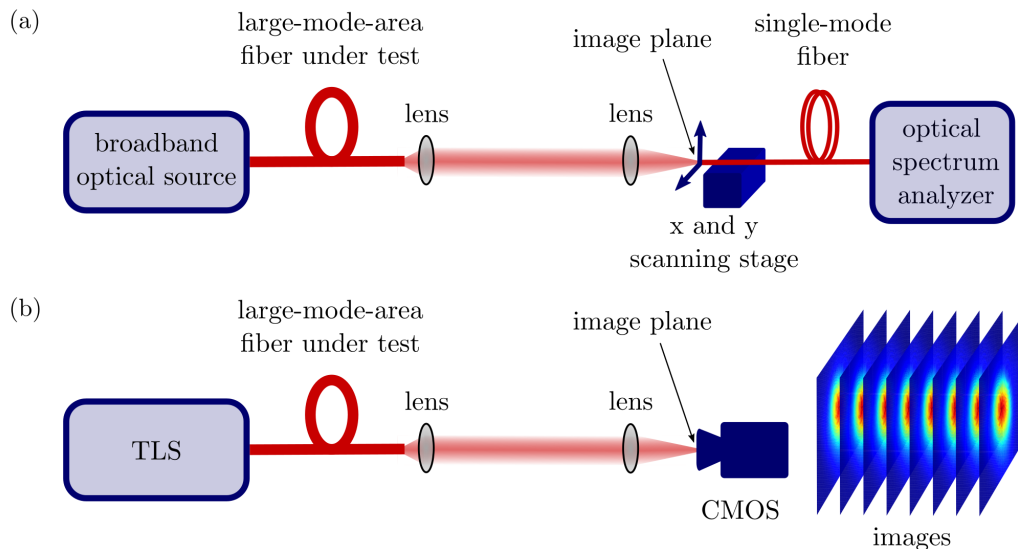


Figure 4.2: Schematic comparison between a conventional S^2 imaging setup in (a) and an approach of a S^2 technique for real time measurements in (b) [Gra16].

around $1\ \mu\text{m}$ in a fiber under test and to use the advantages of an all-fiber setup, a new TLS architecture has been developed. The key component is a fiber-based high-speed optical tunable filter consisting of a Fabry-Perot cavity without guiding optics or optical collimation from *Micron Optics*. The schematic setup with two parallel coated fiber end faces is presented in Fig. 4.3(a).

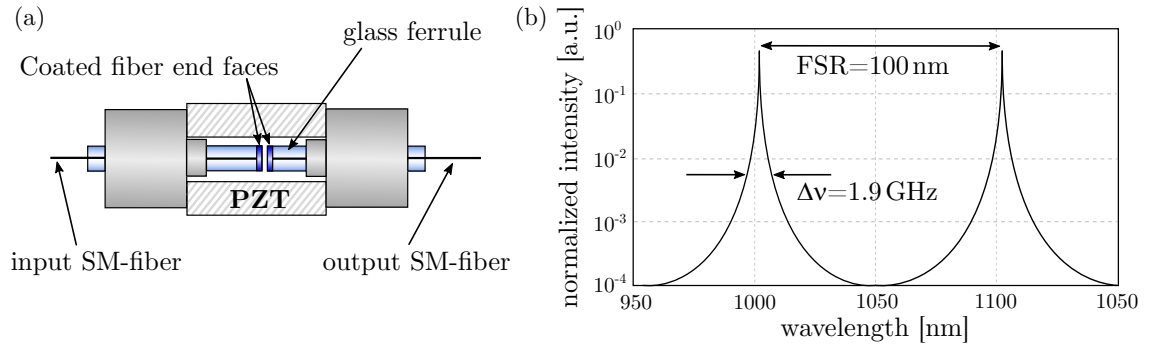


Figure 4.3: Setup of an all-fiber tunable fiber filter based on a Fabry-Perot cavity (FFP-TF) in a). The transmission spectrum of the normalized intensity in dependence of the wavelength is shown in b).

Due to the simple lensless all-fiber construction, the Fiber Fabry-Perot Tunable Filter (FFP-TF) allows for a compact package by achieving a high finesse and maintaining low losses. Thus, misalignment and environmental sensitivities can be minimized and long-term stability and reliability can be increased. By minor changes in the distance between the fiber end faces, the conditions of the resonator frequencies were changed, which were achieved by integrated piezo elements.

Fig. 4.3(b) presents the normalized transmitted intensity in dependence of the wavelength. In the wavelength range around $1\ \mu\text{m}$, the FFP-TF exhibited a free spectral range (FSR) of 100 nm and an optical bandwidth of 1.9 GHz according to a relatively high finesse of $\sim 14,000$. Here, the input power was limited to 2 mW. The FFP-TF was driven with an external supply voltage up to a maximum voltage of 70 V. In this voltage range, the transmitted intensity can be tuned with a tuning range of 6 V/FSR through several FSR. With a continuous scanning mode at up to 50 kHz, the FFP-TF is able to realize S^2 -real-time measurements. For an overview, the specifications of the used FFP-TF are listed in Tab. 4.1:

The input signal of the FFP-TF bases on amplified spontaneous emission (ASE) light generated in an Yb^{3+} -doped fiber (SM-YDF-5/130-VIII, *Nufern*) with a core diameter of $5\ \mu\text{m}$, in which the required pump energy was provided by a single-mode laser diode (*Bookham*) with a maximum output power of 300 mW at 976 nm (see Fig. 4.4). A commercial fiber-based isolator (IO-F-980, *Thorlabs*) protected the laser diode against possible back reflections and a first subsequent wavelength-division multiplexer (WDM) guided the light into the active fiber. As the whole laser system was based on a core-pumped architecture, the backward propagating ASE-light could be separated from the pump light by the WDM. Here, the effect of a substantially larger ASE-light in backward direction (opposite to the pump light) than for the forward direction due to the effective gain-distribution along

Table 4.1: Relevant specifications of the corresponding FFP-TF

FFP-TF-1000-1100-1.94G14000-4-065-000	Parameter
Operating wavelength	1000 - 1100 nm
FSR	100 nm
Optical Bandwidth $\Delta\nu$	1.9 GHz
Finesse	$\sim 14,000$
Scanning mode	up to 50 kHz
Voltage range	0-70 V
In-/output fiber	HI 1060
Insertion loss	4 dB
Max. input power	2 mW

the fiber was used and the forward-propagating light was used for monitoring the optical power. Afterwards, the transmitted ASE spectrum was modified by a second WDM to achieve an as-flat-as-possible optical spectrum. The output fiber of the second WDM was directly connected with a FC/APC connector interface to the FFP-TF, where a maximum optical power of 2 mW has not been exceeded.

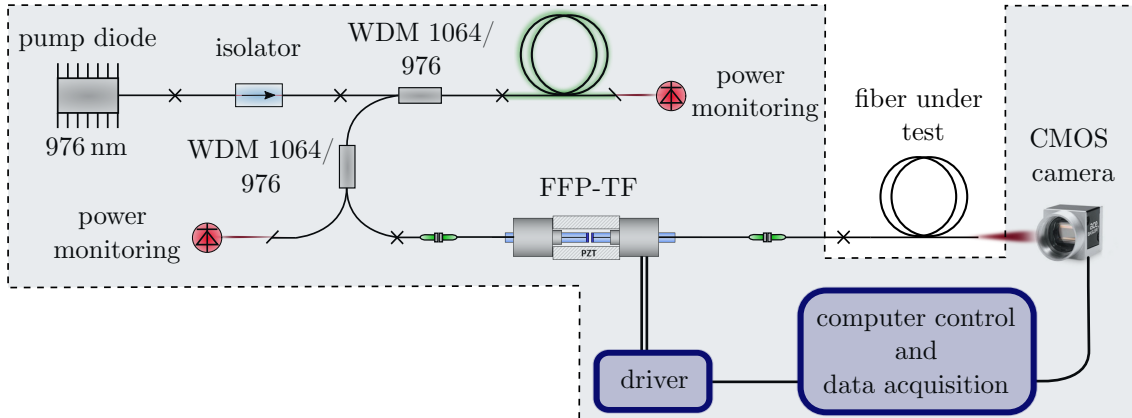


Figure 4.4: Setup of an S^2 -measurement including an all-fiber tunable fiber laser based on a Fiber Fabry-Perot tunable filter (FFP-TF) and a high-speed CMOS camera. WDM: wavelength-division multiplexer.

The input ASE spectrum of the FFP-TF is shown in Fig. 4.5 in black and the transmitted narrow-band spectra at correspondingly different voltages $V_{\text{FFP-TF}}$ at the filter in color. Here, the spectrum in purple corresponds to a wavelength of ~ 1015 nm ($V_{\text{FFP-TF}}=13.5$ V) and the spectrum in dark-red to a wavelength of ~ 1015 nm and ~ 1105 nm ($V_{\text{FFP-TF}}=19$ V). The fact that the resonance conditions were fulfilled twice at 19 V was avoided in the later measuring operation.

After the FFP-TF, a fiber under test can be spliced to the FC/APC connector and

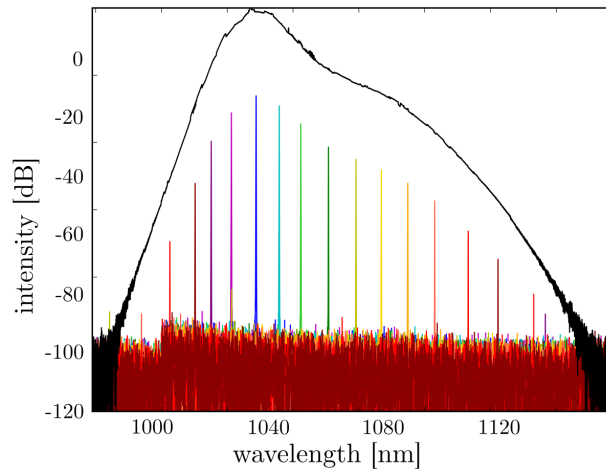


Figure 4.5: Optical spectrum of the ASE input signal in front of the Fiber Fabry-Perot tunable filter in black and the narrow-band transmission afterwards at different voltages applied to the filter in color.

subsequently, the beam profile of the propagated light was imaged on the chip of a CMOS camera. In addition to the implementation of the described fast tunable laser source, the realization of a fast detection of the optical beam profile is also crucial for the application. Therefore, a camera based on the CMOS architecture with a sufficient frame rate was chosen. One difficulty was that these chips, which are mostly based on silicon, are not sensitive enough in the near infrared range around 1 μm . This was compensated by an appropriate coating on the chip to increase the sensitivity. The used 12-bits CMOS camera was fabricated by *Basler* (ace-acA2000-165um-NIR) and had a maximum resolution of 2048x1088 pixel with a pixel size of (5.5x5.5) μm . At an exposure time of 100 μs and a pixel-width and -height of 100 pixel, a sufficient frame rate of more than 1500 frames can be achieved. Due to the CMOS technology, the frame rate is independent on the number of the pixel-array. In summary for an overview, the specifications of the used CMOS camera are listed in Tab. 4.2:

Table 4.2: Relevant specifications of the CMOS camera (ace-acA2000-165um-NIR). W: width, H: height.

ace-acA2000-165um-NIR CMOS camera	Parameter
Resolution (WxH)	2048x1088
Pixel size (WxH)	(5.5x5.5) μm
Sensor size (WxH)	(11.3x11.3) mm
Pixel bit depth	up to 12 bits
Scanning mode	up to 50 kHz
Color	Mono
Interface	USB 3.0

Later on, the frame rate as well as the all-fiber TLS were not the limiting factor for a real-time S²-measurement, but the processing and evaluation of the data. This circumstance is examined in more detail in the measurement method in the following section.

4.1.2 S²-measurement of a 3C[®]-fiber

The maintenance of the beam quality is an important characteristic of a 3C[®]-fiber. Therefore, the beam quality of the in the following chapter used 3C[®]-fiber was investigated with the presented advanced S²-setup.

The parameters of the 3C[®]-fiber under test, which were provided by *nLight Oy*, are listed in Tab. 4.3. A cross-sectional microscope image of such a 3C[®]-fiber is presented in Fig. 4.6, where an efficient single-mode operation can be enabled by a single-side core close to the core.

Table 4.3: Parameters of the 34/250DC-3C provided by *nLight Oy*.

34/250DC-3C	Value
Core diameter	34 μm
NA	0.065
Mode field diameter	27.5 μm
Cladding diameter	250 μm
Number of side cores	1
Side core diameter	$\sim 10 \mu\text{m}$
Side core spacing	$\sim 4 \mu\text{m}$

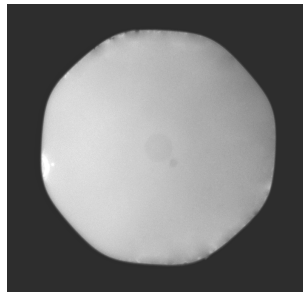


Figure 4.6: Cross-sectional microscope image of the 34/250DC-3C fiber. The 34 μm core is surrounded by a single side core.

For these experiments, a 3 m piece of such a 3C[®]-fiber coiled on a 30 cm spool was spliced to the connector of the S²-imaging setup. Induced losses by an insufficient splice were not observed here. Due to the scanning process of the TLS over the complete optical bandwidth and capturing the beam profiles through the CMOS camera, an optical spectrum could be reconstructed. The beam profile, obtained by integrating the detected images at each point (x,y), is shown in Fig. 4.8. Information about the interference between the LP₀₁ mode and HOMs and the corresponding beat frequencies could be achieved by the sum of Fourier transforms of all measured optical spectra at each spatial point, which is presented in Fig. 4.7 in red. In this case, no significant beat frequencies-peaks are

noticeable, which can be explained by a low amount of guided HOMs in the 3C[®]-fiber core. In comparison, this measurement was repeated with a typical used LMA fiber from *Nufern* (PLMA-GDF-25/250-M), whose result is shown in Fig. 4.7 in light blue. Here, a considerable peak at a group delay difference of ~ 1 ps/m with an MPI value of -23.6 dB (see Eq. 4.10) could be indicated.

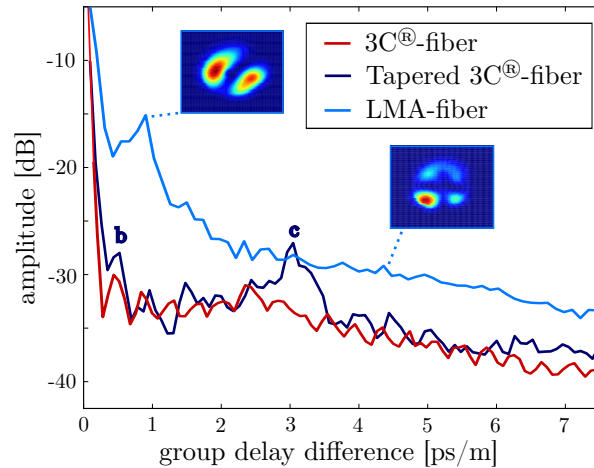


Figure 4.7: Comparison of the S²-imaging results of 3C[®]-fiber, a tapered 3C[®]-fiber and a standard LMA fiber. The reconstruction of the corresponding modes at b and c is presented in Fig. 4.8.

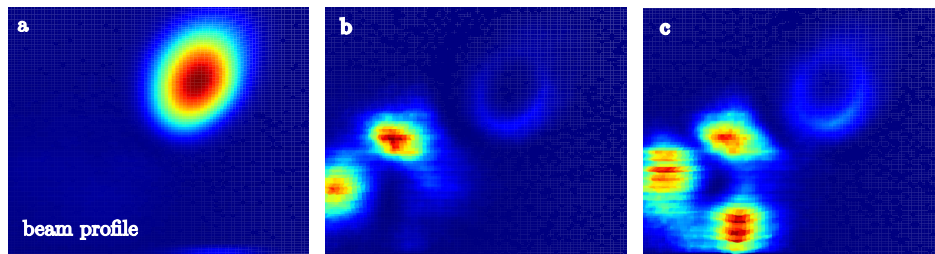


Figure 4.8: Reconstruction of the optical modes (b+c) guided in the side core of a tapered 34/250DC-3C fiber. a): Entire beam profile captured with a CMOS camera.

Taking into account the matrix of the constant α at each spatial point from Eq. 4.7 and Eq. 4.9, the analogous HOM could be reconstructed and the LP₁₁ mode could be identified. At a higher group delay difference of 4.4 ps/m, the LP₂₁ mode could be determined as well, although the beat frequency-peak is not very pronounced. Additionally, in this measurement of the LMA fiber, it is noticeable that the overall sensitivity is lower than the measurement with the 3C fiber, despite the same measurement parameters such as averaging, etc. were used. The beat frequency-peaks may be smeared with a higher amount of HOMs and an increased number of interferences inside the core and form a broader Fourier spectrum.

In the manufacturing of fiber-based optical components, the fibers will be locally heated and slightly tapered. Therefore, it is of interest to examine this influence on the 3C[®]-fiber for the first time. As heat source for tapering the 3C[®]-fiber, a hydrogen-oxygen microflame and two precisely controlled motor stages for an accurate alignment were applied to reduce the cladding diameter from 250 μm to 125 μm . Appropriately, the MFD was scaled down from 27.5 μm to a calculated diameter of 12.6 μm . The tapered 3C[®]-fiber was then characterized with the S²-technique. The results are presented in Fig. 4.7 in blue. In comparison with the actual untreated 3C[®]-fiber, an additional significant beat-frequency peak at ~ 3 ps/m could be determined. The reconstruction of the corresponding mode is shown in Fig. 4.8c, whereby the reconstruction cannot be assigned to any typical LP_{lm} mode. The same applies to the reconstruction in Fig. 4.8b, whereby it is close to a LP₁₁ mode. These results show the excellent beam quality with a minor amount of HOMs of the 3C[®]-fiber again, even when these are tapered, compared with typical LMA fibers. Based on these results, the 3C[®]-fibers are basically suitable for the manufacturing of optical components. Especially this fact makes it also interesting for a use in applications such as GWDs. Thus, optical components integrated in 3C[®]-fiber were developed and described, which is shown in the following Section.

4.2 Mode field adapter

The development of LMA fibers opens up on the one hand the possibility of power scaling of fiber laser systems. But on the other hand the coupling of light into such fibers is typically connected with the excitation of higher modes. Also a standard splice between two different fiber geometries can lead to the degradation of the beam quality by an increased HOM content. The mode matching from the LP₀₁-mode from a SM-fiber to a LMA fiber can be efficiently realized by the expansion and alignment of the mode field areas, which led to the development of the optical component of a mode field adapter (MFA). In principle, such devices use an adiabatic taper between the two fibers and are bidirectional usable, but are commonly integrated in laser systems in the direction of propagation towards the larger mode area fiber. Consequently, in all-fiber laser or amplifier systems, a MFA is a key component to enable a high-power operation at the best possible beam quality.

In general compared with typical LMA fibers, specialty fibers such as PCFs or 3C[®]-fibers have a significantly larger mode field diameter [Kni03; Liu07a; Rus14]. Here, the importance of an efficient MFA is to be assessed even higher. The use of MFAs in combination with specialty fibers is the current state of research and has only been investigated in a few laser systems. Zhao et. al designed a high-power all-fiber ultra-low noise laser at a power level of 100 W with an integrated MFA connected to a PCF suitable for GWDs [Zha18b]. In addition, Qi et al. characterized a high-power all-fiber supercontinuum generation source with such a MFA [Qi18]. However, as a result of the manufacturing, the micro-structured PCFs collapsed during this process and the light guidance was negatively influenced. On the contrary, the all-solid 3C[®]-fiber shows no noticeable change in the internal fiber structure due to the induced heat.

The design of such a device is illustrated in Fig. 4.9. For the first time, a MFA was constructed with a passive 3C[®]-fiber (34/250DC-3C). For that, the 3C[®]-fiber was inserted

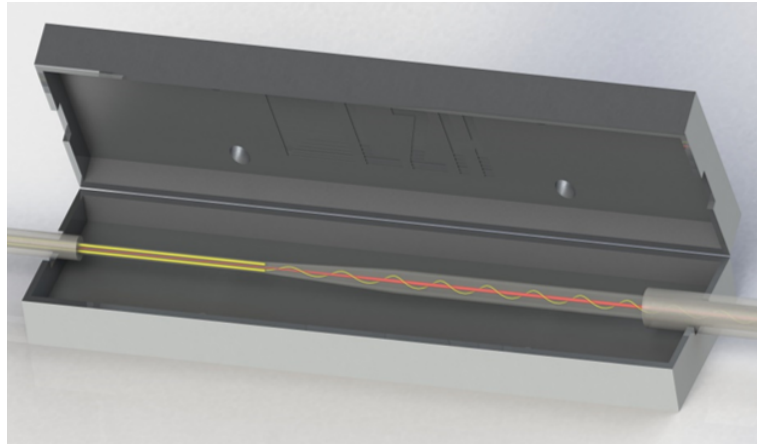


Figure 4.9: Illustration of the designed mode field adapter with a standard polarization-maintaining SM-fiber (PLMA-GDF-10/125-M, *Nufern*) and a 3C[®]-fiber (34/250DC-3C).

on two precisely controlled motor stages with a heat source located in the center of both stages. Afterwards, the fiber was heated up between the annealing and softening temperature of fused silica by a hydrogen-oxygen micro-flame and tapered with a pulling speed of about $60 \mu\text{m/s}$ per motor stage and a fiber tension of about 10^{-2}N . After a distance of 20 mm, the heating and drawing process was stopped and a taper of the fiber diameter from 250 to $125 \mu\text{m}$ was achieved. At the waist of the taper, the 3C[®]-fiber was precision cleaved with a typical fiber cleaver and spliced to a standard polarization-maintaining SM-fiber (PLMA-GDF-10/125-M, *Nufern*). The image of such a splice is shown in Fig. 4.10.

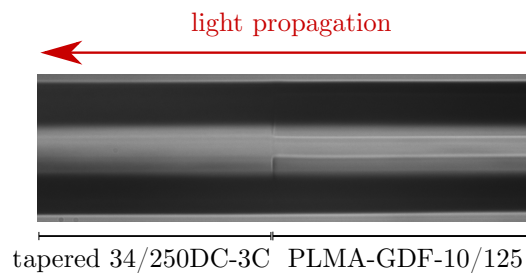


Figure 4.10: Image of a splice of the MFA between a standard polarization-maintaining SM-fiber (right side: PLMA-GDF-10/125-M, *Nufern*) and a tapered 3C[®]-fiber (left side: 34/250DC-3C).

For the characterization of the beam quality, the presented S²-imaging setup was used (see Fig. 4.4). Thereby, the measurement method did not differ from that in the previous sections and the corresponding results are represented in Fig. 4.11 compared to an untreated and tapered 3C[®]-fiber and a typical LMA fiber (PLMA-GDF-25/205-M, *Nufern*). The Fourier transform of the optical spectrum of the MFA differs from the untreated 3C[®]-fiber only in the beat-frequency peak b at a group delay difference of 0.9ps/m . In addition to the

beam profile integrated across the optical spectrum in Fig. 4.12, the reconstruction of this mode can be clearly assigned to the LP_{11} -mode, which has a MPI value of 30.1 dB. Thereby, only the fundamental mode is guided in the core and the LP_{11} -mode was coupled due to the fulfillment of the quasi-phase matching condition into the sidecore and can only be identified there. Due to the higher NA of the sidecore, the image of the LP_{11} -mode is shown larger than the LP_{01} -mode in Fig. 4.12. The S^2 -imaging method illustrates impressively the working principle of the $3C^{\circledR}$ -fiber, so that in the end a guided fundamental mode content of over 99% can be determined in the core. This value was calculated by the ratio between the integrated sum of HOMs at each group delay differences compared to the amount of the LP_{01} -mode.

Due to the active suppression of the HOM by the $3C^{\circledR}$ -fiber, the quality of the MFA is determined by the transmission of the optical light through the component. By splicing an LMA fiber with a $25\ \mu\text{m}$ directly onto the $3C^{\circledR}$ -fiber, a fundamental mode fraction of >98 was also measured, but the optical transmission after the $3C^{\circledR}$ -fiber was only in the range of 50-60%. Due to the integration of a MFA, the optical transmission was increased to $\sim 90\%$. For an amplifier system, this means a more efficient amplification process due to the higher possible seed power and the reduction of non-linear limitations such as SBS or ASE.

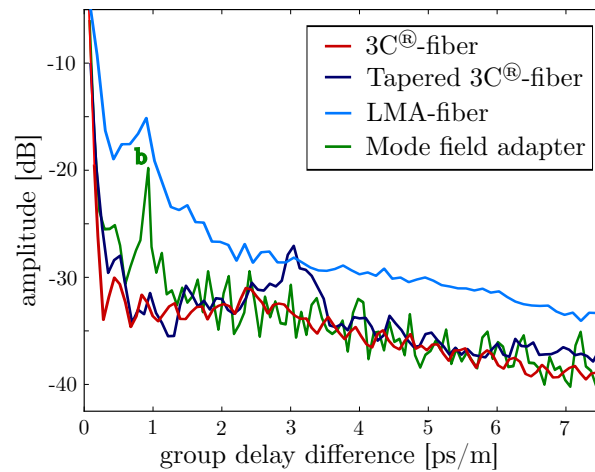


Figure 4.11: Results of the S^2 imaging technique: Fourier transforms of the optical spectrum of a $3C^{\circledR}$ -fiber-MFA compared with an untreated and tapered $3C^{\circledR}$ -fiber and a typical LMA fiber (PLMA-GDF-25/205-M, *Nufern*). The corresponding beam profile and the reconstruction of the mode at the beat-frequency (b) at $0.9\ \text{ps/m}$ is shown in Fig. 4.12.

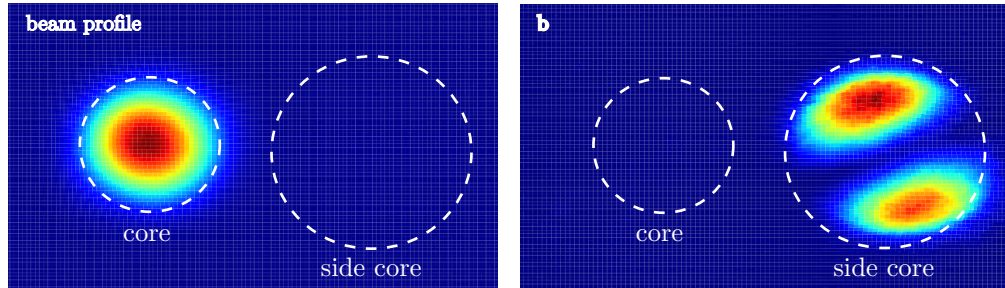


Figure 4.12: Left: The beam profile integrated across the optical spectrum after the 3C[®]-fiber of the MFA. Right: Reconstruction of the LP₁₁-mode, which is exclusively guided in the sidecore.

4.3 End cap

The power scaling of optical fiber applications in the typical spectral range from ultraviolet (UV) to infrared has become more and more common. However, especially using fibers in the UV and lasers in pulse operation, the power levels reach a critical point, where the fiber can be destroyed. It is mainly restricted by the power density at the fiber end-faces, when neglecting non-linear or other effects. In this context, the use of end caps extends the range of high-power lasers. Additionally, these end caps correspond to an output interface which improves the mechanical stability.

A general end cap is a coreless material, typically fused silica, without any waveguide properties, which enables an even expansion of the incoming light. Thus, the intensity at the air-to-glass interface can be significantly reduced by more than one order of magnitude to prevent a potential damage such as scorching of the end-face or photo-contamination by the generation of a dipole trap [Kni17]. As a non-waveguiding material, the mode field diameter of the beam already starts to diverge within the end cap. The resulting power densities at the end-face are not dependent from the wavelength, e.g. in the UV range, anymore as without an end cap [Kni17]. The surface of these end caps can be also coated by AR-layers to minimize reflections.

With these components, the realization of high-power fiber amplifiers was enabled such as presented in the following Chapter 6.

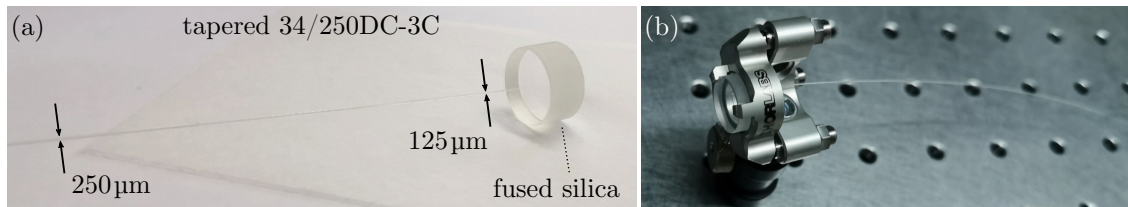


Figure 4.13: (a): Image of the tapered 3C[®]-fiber, where the cladding diameter is reduced to 125 μm and spliced on an end cap. (b): Image of the mount for the end cap including the tapered 3C[®]-fiber.

4.4 Cladding light stripper

In fiber laser or amplifier systems, optical fiber-based components are typically protected against undesired propagating light in the core by a fiber-based isolator. However, if the light is guided in the cladding either by intentional pump light or by disturbing signals caused by splice losses, geometric mismatch and bending losses, a sufficient suppression of counter-propagating light using an optical isolator is not guaranteed and the used component can be damaged. In addition, depending on the fiber design, the light in the cladding can be guided through the entire system, which can lead to interference phenomena and thermal instabilities in the laser system.

In the fiber technology, this issue was solved by the development of a cladding light stripper (CLS). The physical background behind this application is the interruption of the guiding properties of the optical fiber, which can be achieved through different approaches. By using an adhesive or gel with a higher refractive than the cladding material, the total reflection of cladding-light on the glass surface of the fiber can be interrupted and a significant amount of light is coupled out of the fiber. With this technique, an optical attenuation of more than ≥ 20 dB can be achieved. However, this gel is not well suited to dissipate the resulting heat. Thus, the performance in continuous operation in high-power laser systems is not

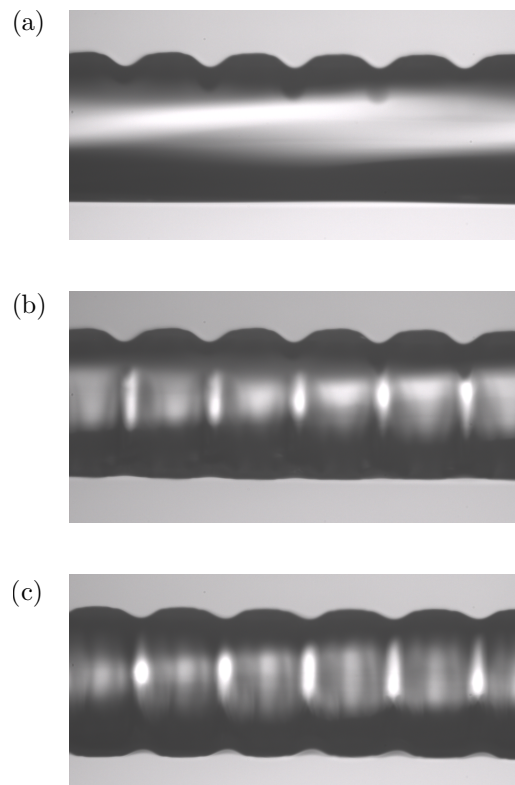


Figure 4.14: Image of a fabricated cladding light stripper integrated in a 3C[®]-fiber with micro-structured grooves on a single side in (a), on two sides in (b) and on three sides in (c).

qualified.

In an etching technique, acid is applied to the fiber cladding to create small but effective imperfections on the glass surface, which also interrupts the guiding properties of the fiber. Such a CLS can be fabricated for a use in high-power laser architectures of several hundred-watts with typical cladding light attenuation of ~ 20 dB [Yin17]. However, the method is associated with a high production effort and the use of hazardous substances. In addition, some of them do not meet the highest requirements (e.g. out-gassing or bio-compatibility) of some applications.

Another method with no additives such as glue or acid is the manufacturing of CLS using a CO₂-laser. The surface of the fiber is modified by micro-structured grooves such that the light guidance is significantly influenced [Wys18]. For the first time, such a CLS was directly integrated in a 3C[®]-fiber (34/250DC-3C), which does not change the basic structure of the 3C[®]-fiber with a groove-depth of 30 μ m and thus retains the functionality. Fig. 4.14 presents the micro-structured 3C[®]-fiber with inscribed grooves on a single side in (a), on two sides in (b) and on three sides in (c).

The characterization of the cladding light attenuation of the fabricated CLS was executed with a fiber-coupled laser diode (BMU30-975-01-R02) with a maximum optical output power of 30 W at 976 nm (see Fig. 4.15(a)). Because of the fiber geometry of the multimode 105/125-fiber of the laser diode, the fiber was directly spliced to the 34/250DC-3C fiber to achieve a sufficient coupling efficiency. The optical output power was compared after a fiber length of 10 m coiled in a diameter of 30 cm between the 3C[®]-fiber with and without a CLS. The corresponding results are presented in Fig. 4.16, where the output power is plotted in dependence of the initial pump light. At an initial pump light of 10 W, ~ 120 mW was detected after the 3C[®]-fiber with the CLS, which corresponds to an optical attenuation of 19 dB. This parameter is comparable to typical CLS devices integrated in standard fibers [Wys18; Yin17].

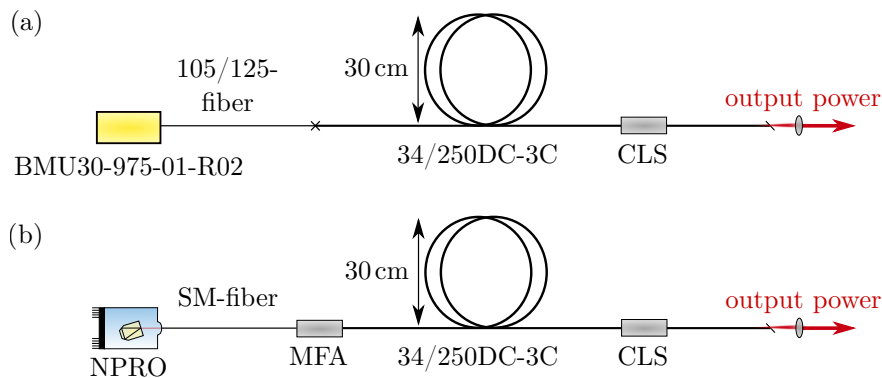


Figure 4.15: Experimental setup for the characterization of the cladding light stripper. In a), a 30 W pump diode was spliced to the 3C[®]-fiber to measure the attenuation by the CLS. In b), the light of an NPRO was guided through the core of the 3C[®]-fiber to determine the impact of the CLS on the core light. Afterwards, the optical output power was measured with a thermal power head.

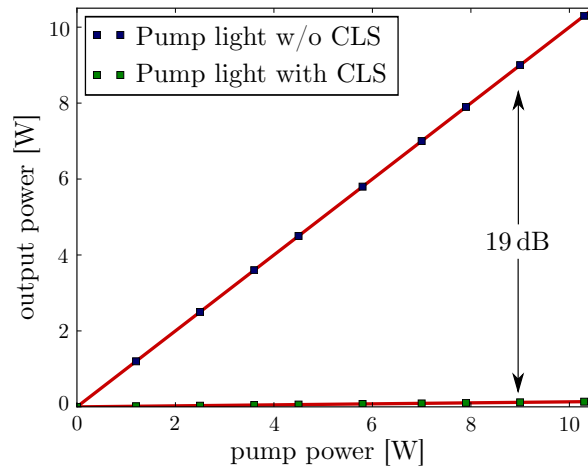


Figure 4.16: Cladding light attenuation of the first in-house cladding light stripper directly integrated in a 3C[®]-fiber with an optical suppression of ~ 19 dB, which is comparable to components based on standard fibers.

The induced losses for the signal light in the fiber core were investigated by the signal of a single-frequency non-planar ring-oscillator coupled into a SM-fiber. The core of the SM-fiber is then adapted to the 3C[®]-fiber via a MFA to ensure a single-mode signal at a wavelength of 1064 nm in the 3C[®]-fiber core. Because the groove depth with ~ 30 μm is not deep enough to influence the side- or core structure or interacts with the propagating electrical field, the difference in the optical output power after the 3C[®]-fiber with a CLS is below the verifiable accuracy compared to the results without a CLS. The experimental results are represented in Fig. 4.17.

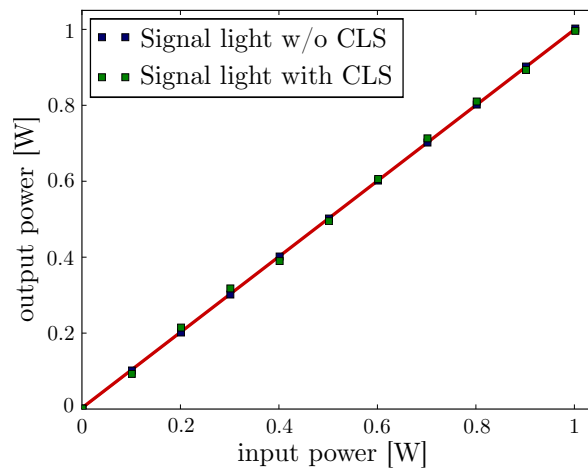


Figure 4.17: The signal light attenuation of the in-house designed cladding light stripper directly integrated in a 3C[®]-fiber is below the verifiable accuracy.

Because of the advantage of not using additives such as glue, this technology is also suitable

for high-power operation. This is demonstrated in a following chapter, where such a CLS was integrated directly into an active Yb³⁺-doped 3C[®]-fiber. In addition to their use in 3C[®]-fibers, other specialty fibers such as PCFs could also benefit from this process, where new, interesting areas of application could arise.

4.5 Signal and pump combiner

The demand for compact, reliable and efficient monolithic high power laser systems has been increased in recent years [Mac04; Wel19]. For further power scaling of all-fiber lasers or amplifiers, a highly integrated signal and pump combiner is a key component. Fused tapered fiber (TFB) bundles are the most common type of fiber combiner [DiG99; Hea05] and are based on the fiber end face pumping technique. The capability of handling several hundred watts of pump power makes a TFB practicable for a variety of fiber applications [Zhe18]. However, a TFB consists of a tapered signal fiber and several tapered multi-mode fibers, where the numerical aperture (NA) of the pump light and the mode field diameter (MFD) of the signal light are changed by the taper process. The necessary optical mode matching and the fusion splice to the output standard double-clad fiber lead to several drawbacks of the TFB architecture. On one hand, the flexibility in the choice of input fibers matching to the output DC fiber is reduced and on the other hand, a slight mismatch or misalignment degrades the beam quality significantly in conjunction with signal insertion loss. In the case of counter-pumped fiber lasers or amplifiers, signal light induced by insertion losses (up to 10%) can couple into the pump diodes and damage them due to their insufficient isolation against the amplified light. Specialty fibers can theoretically be used in a backward propagating TFB design, whereby they are practically not utilized due to the unwanted use of a standard LMA fiber in the high-power part of the setup. In principle, the SBS threshold and the corresponding reachable output power of counter-pumped single-frequency fiber amplifiers can be increased compared to co-pumped systems significantly.

A more promising approach to overcome these problems is a side-pumping technology [The12b], where the coupling of the pump light can be achieved via the outermost cladding surface into the signal fiber. The key advantage of this technology is an uninterrupted core of the signal fiber, which is a significant advantage for the use of specialty fibers in this combiner architecture. However, micro-structured air holes such as used in PCFs collapse due to the manufacturing process, but all-solid designs such as 3C[®]-fibers are not affected. Furthermore, the need for an additional fusion splice in conjunction with signal mode matching can be avoided.

A schematic view of the side-pumped combiner consisting of a pump fiber (PF), a coreless intermediate fiber (IF) and a 3C[®]-fiber is shown in Fig. 4.18.

The incoming pump light was guided in the PF and propagates through the tapered portion of the IF. The IF was fusion spliced to the PF with a commercial filament splicing system and a hydrogen-oxygen micro-flame was applied as heat source for tapering. The temperature adjustment was controlled by variation of the vertical distance between the fiber and the flame. Additionally, two precisely controlled motor stages were installed to allow accurate alignment and tapering of the IF. Due to the tapering process, the NA of the input pump light approximately increases by a factor of the taper ratio (TR) [The12b],

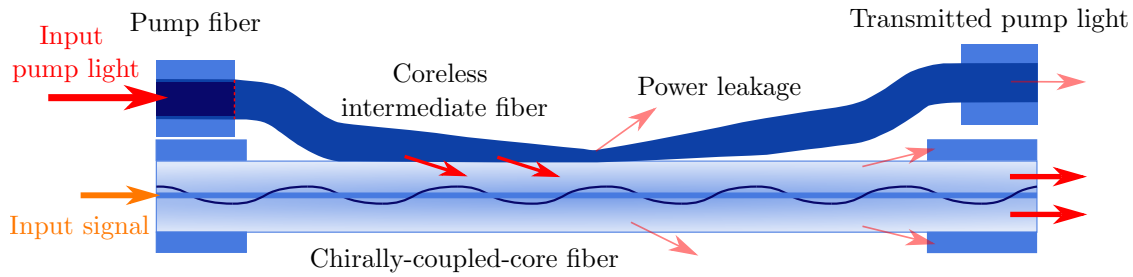


Figure 4.18: Schematic side view of a side-pumped 3C[®]-fiber including important ray paths. The pump fiber is spliced to a tapered coreless intermediate fiber, which enables an efficient pump light coupling to the 3C[®]-fiber.

which is defined as the ratio of the original fiber diameter to the diameter of the taper waist. After tapering, the IF is twisted once around the 3C[®]-fiber, which ensures that the converging taper portion remains in contact during lateral fusing. The overlap area between the 3C[®]-fiber and the IF is defined as the fusion zone. Due to the tapering process the NA of the guided pump light is increased. The pump light propagating at higher NAs couples into the 3C[®]-fiber in the fusion zone. The final lateral fusion process along the fusion zone was carried out at temperatures, which allow sufficient softening of the tapered IFs and only slight softening of the 3C[®]-fiber. It results in a weakly fused component without any thermally induced damage of the core and the sidecore(s) of the 3C[®]-fiber. Compared to the manufacturing process of combiners with typical standard fibers, the fusion process was temporally extended to increase the coupling efficiency of the final 3C[®]-combiner. Pump light that does not couple into the 3C[®]-fiber remains in the IF (transmitted pump light, see. Fig. 4.18) or emerges from the fiber as power leakage into the housing of the combiner. For the manufacturing process of the signal and pump combiner a variety of fiber types are used. An overview of the used fiber parameters was already presented in Table 4.3.

In high power all-fiber laser and amplifier systems, it is typically required to provide multiple pump ports due to the limited output power and brightness of commercial available fiber coupled pump diodes. Therefore, a 3C[®]-fiber combiner with up to four pump ports was developed to provide the required pump power. The first designed combiner was directly integrated in a passive 3C[®]-fiber (34/250DC-3C) and four fiber coupled pump diodes each with an output power of 150 W at 976 nm were spliced with a matched core diameter of 106.5 μm on the input pump fibers of the pump combiner. The setup is illustrated in Fig. 4.19, where the combined pump light in the 3C[®]-fiber and the residual light in the IFs were afterwards detected with a power head.

The experimental results are presented in Fig. 4.20 and show the combined pump power (red diamonds) and the residual transmitted pump light (red circles) with respect to the total diode power (red squares). At the maximum total diode power of 600 W a corresponding combined pump power of 465 W was measured, which corresponds to a coupling efficiency

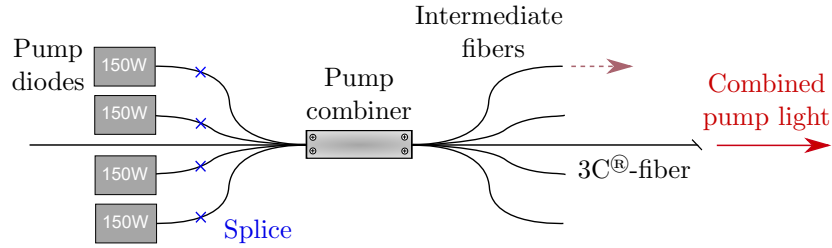


Figure 4.19: 3C[®]-fiber (34/250DC-3C) combiner with up to four fiber coupled pump diodes (150 W each at 976 nm).

of 78% (blue down-triangle). Previous developed side-pumped combiners with standard commercially available large mode area (LMA) fibers achieved a coupling efficiency of up to 93% in theoretical simulations and 92% in experimental components [The12b]. However, this is the very first demonstration of a pump combiner in a 3C[®]-fiber taking advantage of the described benefits of the side-pumping technology. The low coupling efficiency can be accepted, as this device enables for the first time the realization of an all-fiber amplifier setup with 3C[®]-fibers. Possible reasons for the lower efficiency are explained in the following Section 4.5.1. The amount of the pump light in the IFs (blue up-triangle)

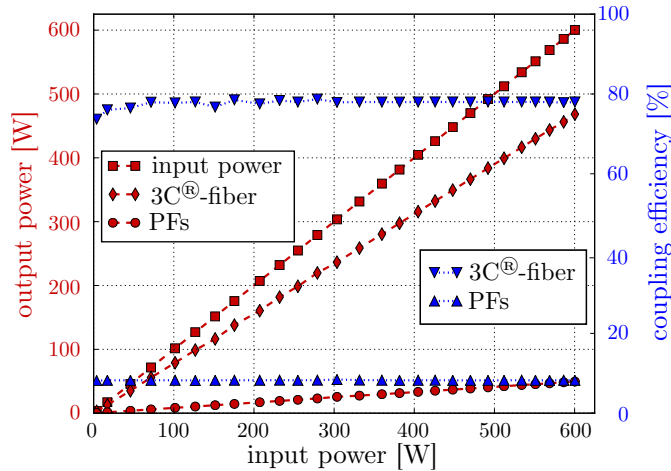


Figure 4.20: Experimental output power results (red) of the combined pump power for a 4+1x1 high-power fiber combiner integrated in a 3C[®]-fiber. The corresponding coupling efficiency of total diode power to the 3C[®]-fiber is shown in blue in percent.

was 8.4% compared to the total diode power. Accordingly, the residual pump light was lost in ways as described above, which led to elevated temperatures of the combiner housing ($\sim 50^{\circ}\text{C}$). The insertion loss for backwards propagating pump light into one of the pump input fibers was measured to be $\sim 10\%$. I.e., in a case of a bidirectional pumping system even if a low pump absorption of only 10 dB is assumed, only 1% would couple back into the laser diodes. Thus, such a device is well suited for a bidirectional pumping system.

4.5.1 Detailed investigations of a multi pump-port 3C[®]-fiber combiner

Possible reasons for the reduction of the coupling efficiency of the 3C[®]-fiber signal and pump combiner compared to standard LMA components is considered in more detail in the following.

To achieve an improved pump absorption, the 3C[®]-fiber has an octagonal cladding structure. In the drawing process of the 3C[®]-fiber, the fiber is twisted to achieve the helical design with rotating sidecores. Thus, the cladding surface shows a slight wavy structure along the fiber. To investigate the influence of the octagonal structure and the additional pattern of the surface on the coupling efficiency, an additional combiner integrated in a fiber with an identical octagonal cladding structure (Passive-250DC-O, *LIEKKI*) but without the twist was manufactured under the same conditions. The measured performance of this 2+1x1 fiber combiner with octagonal cladding structure is presented in Fig. 4.21. At an input pump power of 114 W a combined output power of 102.7 W was measured, which corresponds to a coupling efficiency of 90.1%.

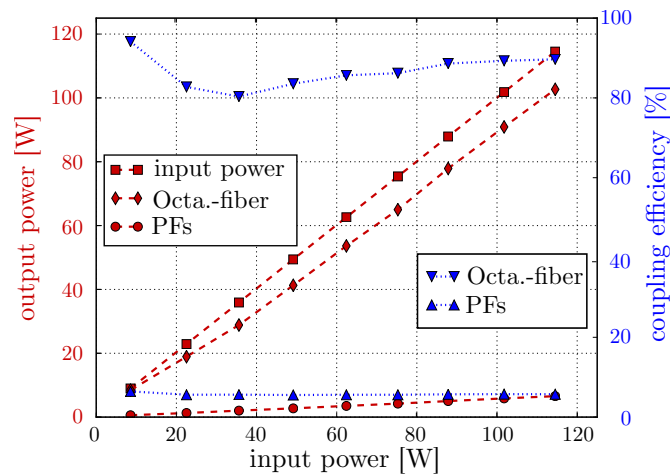


Figure 4.21: Experimental output power results (red) of the combined pump power for a 2+1x1 high-power fiber combiner integrated in a standard fiber with a octagonal structure. The corresponding coupling efficiency of total diode power to the signal fiber is shown in blue in percent.

Thus, it appears that the rotation of the octagonally shaped cladding (or a combination of the resulting longitudinal pattern and the octagonal cladding structure) prevents similar coupling efficiencies of the 3C[®]-fiber pump combiner compared to standard fiber combiner. For a closer examination of the detailed construction of each combiner, X-ray computer tomography pictures were made.

The images in Fig. 4.22 reveal the direct composition of the component and the overlap of the IFs and the signal fiber. In Fig. 4.22 a) - c) a pump combiner is shown integrated in a 3C[®]-fiber and in d) - f) integrated in a standard fiber with an octagonal cladding structure. In the pump combiner with the octagonally shaped fiber, the IFs are always attached on the signal fiber. This enables a successful coupling of the pump light into the signal fiber with an efficiency of 90.1% (see Fig. 4.21).

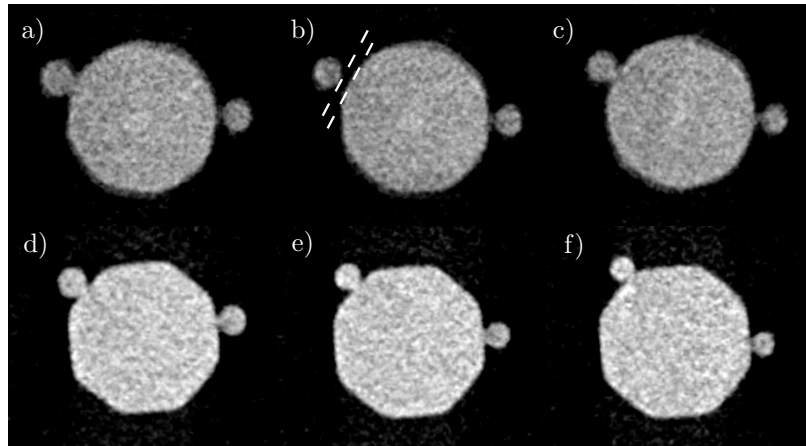


Figure 4.22: Cross-section images of a two port 3C[®]-fiber pump combiner in a)-c) and of a pump combiner based on a fiber with octagonal cladding structure in d)-f) at different positions in the combiner. The two PFs are at all time in contact with the octagonal fiber, whereas the IF is not permanently attached on the 3C[®]-fiber.

In the case of the 3C[®]-fiber, there is not always a spatial contact with the IFs. Especially, the image in Fig. 4.22 b) shows a significant gap between the 3C[®]-fiber and the IF. These gaps lead to an inefficient coupling of the pump light to the signal fiber and an increase of internal losses. These investigations lead to the conclusion that the modification of this pattern towards a flat surface is a promising task for further investigations and will be taken into account for further improvements of the 3C[®]-fiber combiner.

4.6 Conclusion

For the realization of fiber-based high-power MOPA systems in compact and efficient monolithic architectures, the development of optical components is indispensable. In this work, the design and characterization of completely new fiber-based components based on 3C[®]-fibers is presented for the first time.

In this context, a novel implementation of an S²-imaging technique was developed to realize beam quality investigations up to real time measurements. The technique uses an all-fiber tunable filter to enable a spectral data acquisition and a CMOS camera for required spatial information. In a compact setup, the modal content of the guided optical modes in a 3C[®]-fiber and in corresponding components was determined. This method can be integrated in existing manufacturing facilities of fiber-based components and allows a quick and meaningful quality control of the respective device.

In the following, the development of a mode field adapter, an end cap, a cladding light stripper and a pump combiner was presented. All these components were used for the high-power amplifier systems in the subsequent Chapters 5 and 6 and are essential features. Especially, the highly-integrated signal and pump combiner was implemented for the first time in 3C[®]-fibers and is the key component of fiber-based high-power MOPA systems.

Using the proven side-pumping technology, an uninterrupted core of the 3C[®]-fiber ensured a maintained beam quality and the design properties of the specialty fiber. So, the realized optical fiber component avoided an additional fusion splice in conjunction with signal mode matching as it is needed for fused tapered fiber bundles. With four fiber coupled pump laser diodes at 976 nm, a maximum power handling of 600 W was achieved with a coupling efficiency of 78% and enabled a high power signal transmission in forward and backward direction. In the scientific context, the achieved coupling efficiency was lower than the coupling efficiencies with >90% achieved with typical standard fibers reported earlier [The12b]. Therefore, this combiner with the current efficiency value does require a proper thermal management. However, no reliability issues and no direct impact on amplifier performance was determined during operation.

The special design of the 3C[®]-fiber also allows opportunities for further improvements of the coupling efficiency. For that, some kind of mechanical modification of the outer fiber shape will be necessary to achieve a flat and round surface. In this context already different methods were experimentally tested, whereby processing the 3C[®]-fiber with a CO₂-laser is the most promising technique. This method was already successfully tested in first experimental investigations.

Finally, the presented optical components in 3C[®]-fibers open the door to a completely new development of fiber-based high-power MOPA systems. For the first time, the combination of all-solid specialty fibers such as 3C[®]-fibers and optical components was realized to overcome the limitations of current SF laser architectures. Due to the now possible all-fiber designs, such compact and robust all-fiber amplifier systems with specialty fibers are also of interest for special areas of application as GWDs. The subsequent Chapters 5 and 6 refer to this context in detail.

CHAPTER 5

Prototype of a 100 W all-fiber Single-Frequency 3C[®]-Fiber Amplifier

The previous Chapter 4 represented the development of highly-integrated optical components in 3C[®]-fibers. The integration of such special devices in monolithic fiber amplifier or laser systems is accordingly the next logical step. Therefore, this Chapter 5 demonstrates the prototype of an all-fiber amplifier system based on a 3C[®]-fiber for the first time. Thereby, this setup allows the verification of the power scaling capabilities of such laser designs.

As mentioned in Chapter 2.3.2, a 3C[®]-fiber was already used in previous amplifier designs. Such experiments were also carried out at LZH in the past [Kar13]. However, these systems were free-space pumped by appropriate laser diodes. For an improved reliability and compactness, this work concentrates on the development of monolithic and all-fiber architectures with 3C[®]-fibers, to adapt these systems to the challenging requirements of GWDs. Therefore, the novel all-fiber amplifier concept based on the combination of standard fibers and 3C[®]-fibers is presented here. These results were also published in Ref. [Hoc20b].

In Section 5.1, the experimental setup is visualized in detail, where the key component of a MFA was installed between a standard polarization-maintaining fiber and an active Yb³⁺-doped 3C[®]-fiber. The subsequent Section 5.2 shows the experimental characterization of the prototype of an 3C[®]-fiber amplifier. For this purpose, the optical to optical slope and the corresponding PER was examined. Additionally, the behavior of the laser system in long-term operation over several days was investigated. One of the most important parameters of laser sources for GWDs is the beam quality. Therefore, the modal content was analyzed by a scanning ring-cavity of a diagnostic breadboard. Subsequently, the optical beam was characterized for the impact of SBS and the limitations of this prototype were determined.

5.1 Experimental layout

The realized fiber amplifier system consisted of a Yb³⁺-doped 3C[®]-fiber in MOPA configuration. For this purpose a single-frequency non-planar ring oscillator (NPRO, *Innolight* Mephisto 2000NE) with a narrow laser linewidth (< 1 kHz over 100 ms) was used as master oscillator. The particular NPRO seed source technology has proven low frequency- and intensity-noise properties at a continuous-wave output power of 2 W at 1064 nm and is illustrated in the experimental setup in Fig. 5.1.

After an in-coupling stage including lenses and waveplates, an optical power of ~ 1.5 W is guided in a standard passive PM-fiber. The used fiber (PLMA-GDF-10/125-M, *Nufern*) had a core diameter of 10 μm and enables a single-mode operation with a V parameter

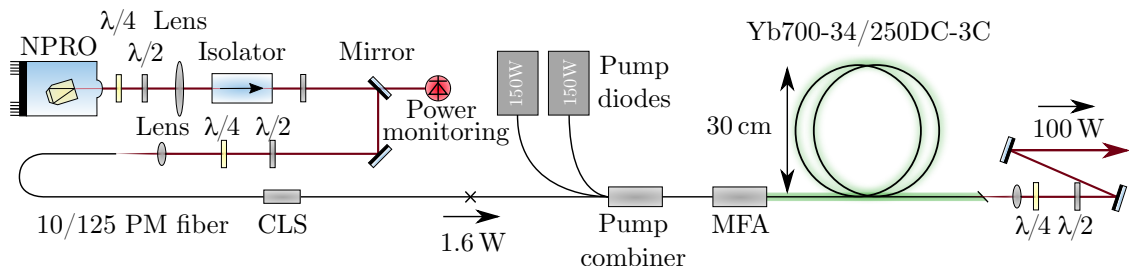


Figure 5.1: Experimental setup of a monolithic amplifier based on a 3C[®]-fiber. The system consists of a non-planar ring oscillator (NPRO), a cladding light stripper (CLS) and a pump combiner integrated in a single-mode fiber. The Yb-doped 3C[®]-fiber is adapted to the single-mode fiber via a mode field adapter (MFA). x: splice.

of $2.19 < 2.4$. Due to the double clad characteristic of the fiber, a cladding light stripper was used to remove any residual light from the cladding. This CLS was fabricated by the technique described in Chapter 4.4, so that the guidance properties of the core were not influenced. The fiber of the CLS was spliced to a matched fiber of a pump combiner, which was the only splice in the system for the signal light and which was in a non-critical low-power area of the laser system. Two pump diodes with an output power of up to 150 W each at 976 nm (K976DN1RN-150.0W, *BWT Beijing Ltd*) delivered the required pump power integrated on a pump-combiner based on the proven side-pumping technology. Here, pump fibers with a core diameter of $106.5 \mu\text{m}$ and a NA of 0.22 were used to achieve a sufficient coupling efficiency ($>90\%$) of the device. The signal and the pump light are guided through the MFA specially developed for this purpose to the 3C[®]-fiber. The designed architecture is required to adapt the mode field area of the 3C[®]-fiber to that of the single-mode fiber. Therefore, this MFA is a key component to enable an all-fiber architecture and determines the transversal mode content excited in the 3C[®]-fiber.

The 3C[®]-fiber (Yb700-34/250DC-3C, *nLight*) had an Yb³⁺-doped core with a diameter of $34 \mu\text{m}$ and a single side core spirally surrounding the main core. The further fiber parameters are the same as presented in Table 4.3 of the passive 3C[®]-fiber version. The fiber length was 2.7 m with a nominal absorption of 2.15 dB/m at 920 nm and it was installed on an aluminum spool with 30 cm diameter for passive cooling.

The linearly polarized light from the seed laser is converted into a polarization state such that the most stable polarized light propagates through the 3C[®]-fiber. After the amplifier, the polarization state is converted back to a linearly polarized light with a quarter and half wave plate. For suppression of polarization effects and a conservation of the polarization stability, previous works injected circularly polarized seed light in the amplifier system [Ma11b; Sto11]. Recent research results also investigated the influence of linearly polarized light propagating through a 3C[®]-fiber. It turns out that the winding of the 3C[®]-fiber without mechanical torsion is critical for the optical performance regarding the stability of the polarization state.

5.2 Beam quality characterization

This Section 5.2 presents the experimental characterization of the optical parameters of the first prototype of a SF all-fiber amplifier based on a 3C[®]-fiber. These investigations contain the optical slope, the polarization extinction ratio, long-term measurements, the modal content analysis, the impact of SBS and the temperature behavior of the system.

5.2.1 Optical Slope and polarization extinction ratio

The measured optical amplifier output power versus the absorbed pump power and a corresponding linear fit are shown in Fig. 5.2. At an absorbed pump power of 143 W in this co-propagating amplifier design, the amplifier system achieves a maximum output power of 103 W at a signal wavelength of 1064 nm. The corresponding optical slope efficiency was 71%, which is comparable with standard Yb³⁺-doped fiber amplifiers pumped at 976 nm [Wel19]. Whereas at smaller pump power level a slope efficiency of around 30% was measured due to the wavelength shift of the pump diodes away from the absorption peak at 976 nm. Additionally, no decrease of the slope efficiency at high pump power levels was observed, which can be typically caused on the one hand by the onset of SBS or by an excessively increasing Yb³⁺-ASE level [Jeo05; Jeo07]. These effects are also not to be expected at such output power levels.

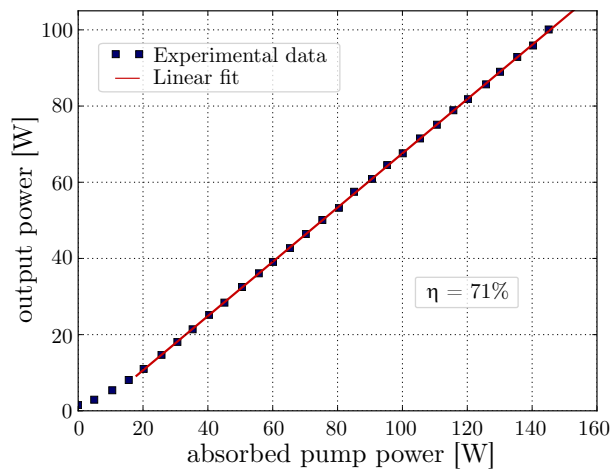


Figure 5.2: Slope of the 3C[®]-fiber amplifier prototype with measured data (blue squares) and a linear fit (red line). The slope efficiency of the absorbed pump power to optical output power is calculated to be 71%.

Laser sources for GWDs must provide these power levels over a longer period of time and are optimized by integrated stabilization systems, where the design of such systems depends on the free-running behavior of the actual laser source. Therefore, the optical output power of the free-running 3C[®]-fiber amplifier was monitored with a L50(150)A-PF-35 thermal sensor (*Ophir*) over a period of 3 and a half days. The experimental result is presented in Fig. 5.3. After a warm-up time of a few hours, the optical output power achieved a stable level of 102.4 W with power fluctuations less than $\pm 0.4\%$, which is significantly

below the specified accuracy of the used power head ($\pm 3\%$). An additional heat up of the used spool by the quantum defect inside the 3C[®]-fiber could not be observed. Besides to the inherently low heat input by using Yb³⁺-fibers compared to co-doped Er:Yb systems [Var17b], the large diameter of 30 cm of the aluminum spool and the resulting large surface area favor the heat transfer to the environment.

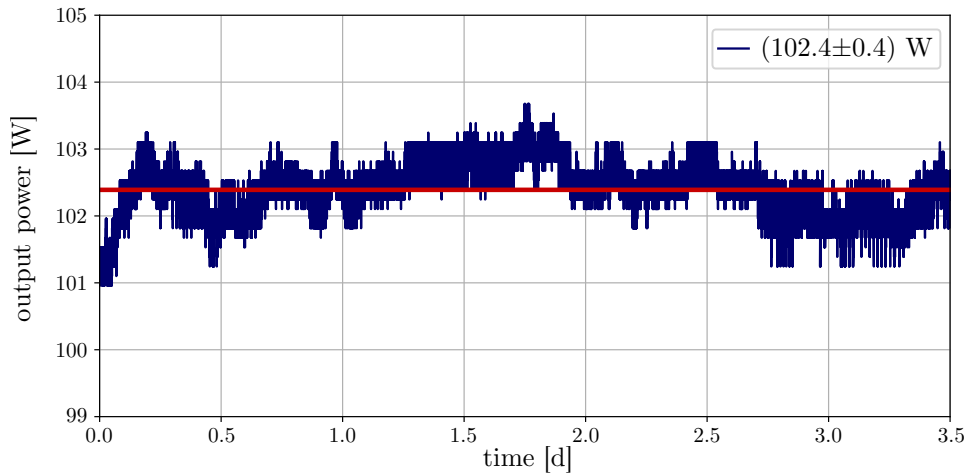


Figure 5.3: Evolution of the optical output power of the amplifier system over 3.5 days.

The linearly polarized light of the seed source is converted into a polarization state such that polarization maintaining properties inside the 3C[®]-fiber were achieved. After the amplifier, the polarization state is converted back to a linearly polarized light due to a quarter and half wave plate. However, the exact orientation of the polarization state inside the fiber is unknown, because the PER was optimized exclusively by considering the best possible power level and stable ratio of the s- and p-polarized light. Hence, the electromagnetic field could also have a state between a circular and linear polarization. In particular, the influence of the PM fiber in the amplifier should be mentioned in this context. However, it has no negative impact on the long-term stability at these considered time scales on this amplifier performance. Because this can probably lead to stability fluctuations of the PER in the long term, this potential issue is avoided by an improved setup in the following chapter.

Nevertheless, this 3[®]-fiber amplifier system achieved a PER of 17.9 dB at the maximum output power level of 103 W. The evolution of the PER at different power levels is shown in Fig. 5.4(a), where the PER in all cases could be determined in the range between 17.9-19.8 dB. Fig. 5.4(b) represents the evolution of the PER at the maximum output power after a warm-up time over a timescale of 5 hours. Here, the PER decreases slightly from a starting value of 19.2 dB and asymptotically approached a value of 17.9 dB. After the long term test shown in Fig. 5.3, a PER of 17.2 dB was measured. This PER value corresponds to an optical loss of 1.7 W, which would not be available for an application of GWDs.

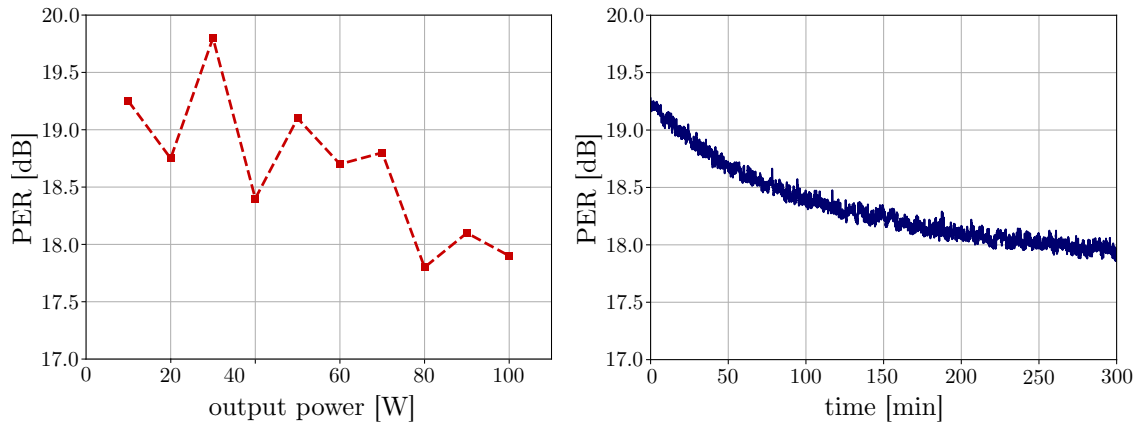


Figure 5.4: Evolution of the polarization extinction ratio at different output power levels in (a) and the evolution of the PER over 5 hours at the maximum output power of 100 W in (b).

5.2.2 Modal content analysis

In Chapter 4.1, the most common methods for beam quality characterizations such as the M^2 and S^2 -imaging technique have already been introduced. Other conventional characterizations procedures use the physical properties of the wavefronts of the beam [Pau12] or are additionally employing, e.g., computer generated holograms [Kai09] to analyze the beam quality. With the exception of the S^2 -technique, these methods require the accurate knowledge of the fiber properties for the calculation of the modal power content. Furthermore, in the application of GWDs the TEM_{00} mode is explicitly required and none of the above mentioned methods is able to directly characterize the TEM_{00} mode content of the beam.

In the case of a beam with a SF linewidth the investigation of the beam quality in terms of the modal decomposition can be realized by a nonconfocal scanning ring cavity. Introduced by Kwee et al., the overlap of the TEM_{00} mode can be directly determined, if the eigenmodes of the ring cavity are equal with the free-space TEM_{nm} modes [Kwe07]. The corresponding cavity used in the following experiments is schematically represented in Fig. 5.5. It had a free-spectral range of 715 MHz and a finesse of 200 at 1064 nm for p-polarized light. The frequency of the eigenmodes of the cavity can be changed by scanning the piezoelectric transducer (PZT) attached to one of the mirrors. By injecting a ramp signal to the PZT, a resonant eigenmode can be selected and is transmitted, while all other TEM_{nm} modes are reflected. By injection a SF signal, only the transmission of one distinct transverse mode corresponding to the resonant length differs due to their Gouy phase [Sie86]. Afterwards, the transmitted optical power depending on the mirror's position is then measured with a photodiode.

Additionally, a lens-combination with suitable focal lengths was installed in front of the measuring setup to enable a sufficient mode-matching to the fundamental Gaussian mode of the cavity. The required low power (<100 mW) of the linearly-polarized beam was adjusted by a power tuning stage via a wedge in the high-power beam and a half wave

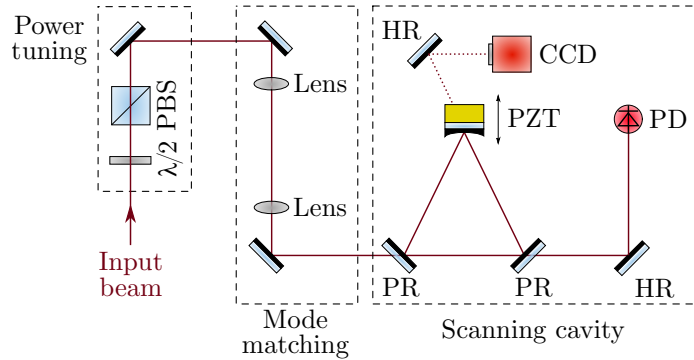


Figure 5.5: Modal content measurement setup with scanning ring-cavity. The input power is adjusted by a power tuning stage and two lenses enable the mode matching to the cavity. PBS: Polarization beam splitter; PZT: Piezo.

plate and a polarization beam splitter (PBS).

For the determination of the fundamental Gaussian mode content of the prototype 3C[®]-fiber amplifier, the cavity transmission was measured in dependence of the frequency over one FSR of the cavity. The resulting mode scan is shown in Fig. 5.6, where the normalized intensity is plotted with respect to the FSR on a logarithmic scale. Due to the comparison with a fundamental Gaussian beam considering a perfect mode matching into the cavity, the mode overlap for a pure TEM₀₀ mode is presented by the peaks at 0.0 and 1.0 FSR. In Fig. 5.6 the fundamental Gaussian mode is represented by a green line. However, a real laser beam can fulfill the conditions for different frequencies of the eigenmodes of the cavity by a slight misalignment, mode mismatching or an actual HOM content of the beam. The real measurement is shown in red and was fitted by the blue curve for the comparison with the fundamental Gaussian mode. The ratio between the overall fit and the fundamental Gaussian mode determines the relative TEM₀₀-mode content.

The impact of misalignment or mode mismatching can be visualized by the rise of particular peaks in the measurement. Especially, the peaks at 0.15 FSR and 0.65 FSR in Fig. 5.6 emerge from the relative misalignment in the vertical and horizontal direction, whereas the peak at 0.3 FSR indicates a mode mismatching. By a manual scanning over the FSR, the peak at 0.5 FSR could be allocated to the HG₀₁ mode, which agrees with the results from the S²-imaging measurement of the previous chapter. Finally, at an output power level of 103 W the 3C[®]-fiber amplifier showed an excellent TEM₀₀ modal content behavior with 98.9% of the power in the fundamental mode.

This measured mode content is very close to the theoretical upper limit of the measurable TEM₀₀ mode content given by its overlap with the fundamental fiber LP₀₁ mode. This value can be calculated by considering the electric fields of these modes described in several textbooks [Rei97]. With the ansatz from Eq. 2.7 and Eq. 2.8 and proper fiber parameters, the overlap integral can be determined and reaches a value of 99.7% [Kar13; Ste15]. Thus, the measured TEM₀₀ mode content is below the theoretical limit.

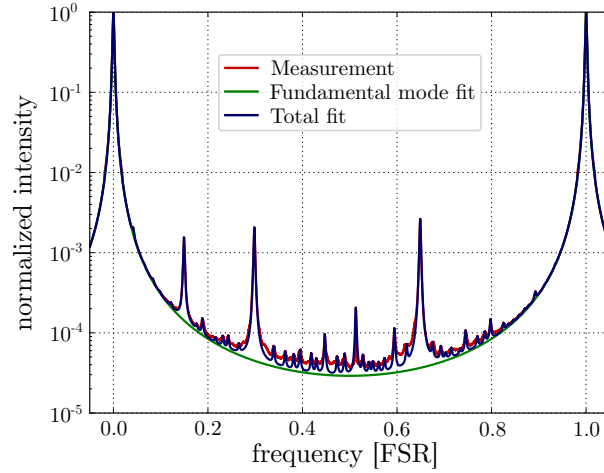


Figure 5.6: Mode scan at an output power of 103 W with a fundamental mode content of 98.9%. The normalized intensity is shown in dependence of the frequency over one free spectral range of the cavity.

In comparison to other amplifier systems and especially to those under development for GWDs, to my knowledge, this 3C[®]-fiber amplifier has the highest measured fundamental mode content with 98.9% up to an output power level of ~ 100 W. Thus, this laser system exhibits a better beam quality than, for example, the *neoVAN-4S-HP* amplifier design with only 2.9% HOM content at an optical power of 114 W [Thi19] or the engineering fiber amplifier prototype with an HOM content of 2.5% at 125 W [Wel19]. With regard to an excellent beam quality, these results demonstrate the potential of 3C[®]-fiber amplifiers as laser sources for the next generation of GWDs.

5.2.3 Stimulated Brillouin scattering

For single-frequency fiber amplifiers, stimulated Brillouin scattering is the dominant limitation as soon as a certain power level is exceeded [Hil08]. In addition to the output power limitation, SBS imprints a broadband excess intensity noise on the signal. The physical origin was investigated in more detail in Chapter 3.

In the scientific community, there are several definitions to determine the SBS threshold. Typically, the slope of the amplifier either in forward or backward direction is considered. For this purpose, the following definition was introduced in addition to Eq. 2.20 [Eng14]:

$$P_S(L) = \mu_{\text{th}} P_P(L) = \mu_{\text{th}} P_{\text{SBS}}. \quad (5.1)$$

For the mathematical derivation in [Smi72], a numerical value of the threshold power ratio $\mu_{\text{th}} = 1$ was used. In fact, despite this assumption, there is a usable approximation with $\mu_{\text{th}} \approx 10\%$ of this SBS threshold in fibers with strong attenuation. In various applications, e.g. in the telecommunication, even smaller reflected power components can disturb the overall performance. Therefore, in [Bay90] a threshold power ratio $\mu_{\text{th}} \approx 1\%$ was introduced to define the SBS threshold. Regardless of this definition, the detection of an increase in

the intensity noise is the most sensitive identification and thus the most relevant indicator regarding an application in GWDs [Hil08].

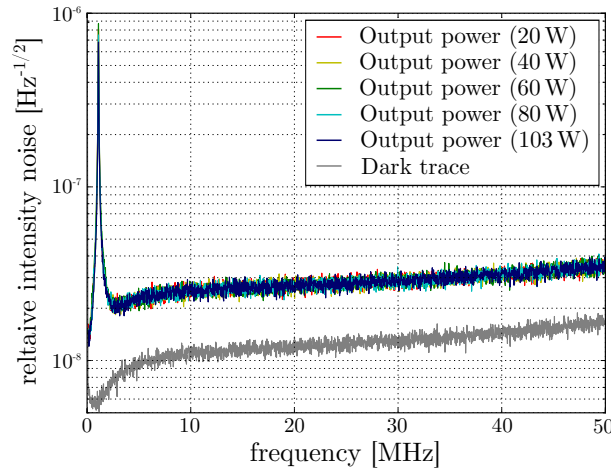


Figure 5.7: Relative intensity noise of the optical amplifier output at different power levels up to 103 W with no onset of SBS.

Fig. 5.7 presents the relative intensity noise of the output signal up to a frequency of 50 MHz at different power levels up to 103 W measured with a spectrum analyzer E4440A (*Agilent*) and a photodiode (*Thorlabs*, PDA10CF-EC). The peak below 1 MHz corresponds to the relaxation oscillation peak of the NPRO and at higher frequencies the measurements were shot noise limited. At all measured power levels no increase of the intensity noise above the shot noise could be detected. In comparison to Fig. 3.5, a measurement was shown, where a significant increase of the intensity noise could be detected above the SBS threshold. Hence, in the 3C[®]-fiber system, there was no onset of SBS and the amplifier operated SBS-free up to its maximum optical output power of 103 W.

5.2.4 Temperature behavior

In the current amplifier design, the MFA has a critical impact on the performance of the system, because the pump light and signal beam both propagate through it and because of the splice to an active fiber. Even low optical losses in the device would lead to a heating of the fiber and the housing. At a certain temperature the fiber, especially the coating, can be damaged irreversibly, which can lead to the destruction of the optical component and the entire amplifier system. The evolution of the temperature at the housing of the MFA with respect to the output power is shown in Fig. 5.8. Despite an active water cooling on the housing, the component reached a temperature of over 80 °C at the maximum output power limiting a further robust power scaling. At this temperature level, a critical point has been exceeded and the MFA has been irreversibly damaged. However, the MFA was designed exclusively for an optimal light propagation in the core and not for the guiding of pump light in the cladding. Therefore, further optimization of the MFA can certainly reduce the

optical losses and, consequently, the heat generation. Thus, a further power scaling should be feasible. Nevertheless, this prototype of a 3C[®]-fiber amplifier in a monolithic design was not limited by available pump light or parasitic laser effects, but by the key component of the MFA.

Instead of a simple improvement of the current MFA architecture, the next Chapter 6 will focus on the development of integrating directly a pump combiner in the 3C[®]-fiber. Due to such a component, the pump light does not have to propagate through the MFA, whereby the heat generated in the MFA is significantly reduced.

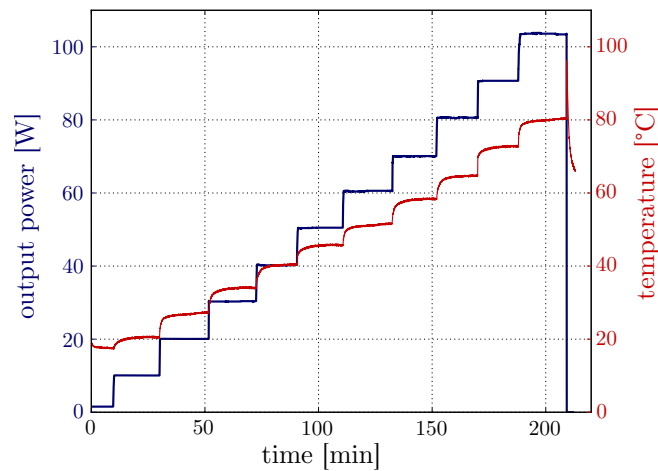


Figure 5.8: Evolution of the temperature of the MFA at different output power levels and time.

5.3 Conclusion

The development of laser sources for the next generation of GWDs has to fulfill challenging requirements regarding the optical output power levels. These are far above the technical specifications of current laser systems. Therefore, new technologies must be taken into account in this context. One possibility is the use of 3C[®]-fibers in monolithic fiber amplifier systems.

This chapter presented the first prototype of an SF all-fiber amplifier based on a 3C[®]-fiber in a compact laser system. This system was initially designed to validate the functional feasibility and the optical parameter of such amplifier architectures. Finally, the 3C[®]-fiber amplifier system achieved an optical output power of 100.1 W in a linearly polarized TEM₀₀-mode. The measured fundamental mode content of 98.9% is the highest value demonstrated for an output power level of around 100 W. Additionally, the system exhibited a stable operation for several days with no onset of SBS or other parasitic effects.

This world's first prototype served as a successful demonstration of an all-fiber design and its polarization and beam quality capabilities using 3C[®]-fibers in monolithic amplifier architectures. With respect to the excellent beam quality, this work emphasizes the high potential of fiber amplifiers based on 3C[®]-fibers as laser sources for the next generation of GWDs in general.

In the following chapter, an improved amplifier design based on these experimental results and the limitations of the current amplifier architecture, the fiber amplifier design was revised and further optical components were integrated in the 3C[®]-fiber. In this improved design, no pump light propagates through the MFA, and, thus, further power scaling is possible by using a highly-integrated 3C[®]-fiber signal and pump combiner. These results are presented in the following Chapter 6, where the laser requirements of GWDs are also explicitly discussed.

CHAPTER 6

High-power spliceless 300 W Single-Frequency 3C[®]-Fiber Amplifier Module

The high precision measurement technique of GWDs demands very stable and robust laser systems with a linearly-polarized single-frequency output beam [Abe11; Hil09]. Most probably, the next generation of GWDs will be using a continuous laser source at 1064 nm around an output power level of 500 W for the high-room temperature, high-frequency interferometer [Abe11]. Despite of the availability of significantly more efficient pump laser diodes and improved optical components, it is still a challenge to amplify a single-frequency signal with a linewidth of only around 1 kHz to the required optical power level maintaining the excellent beam quality. A potential approach was developed by Theeg et al. in form of an all-fiber single-frequency amplifier with an output power of at least 200 W [The15], which was transferred afterwards to an engineering prototype by Wellmann et al. [Wel19]. The stabilization of such a fiber based laser system was also investigated by Oppermann et al. [Opp17].

Due to the technical and physical fiber geometry of typical used standard step-index LMA fibers in such all-fiber amplifier architectures, i.e., as their core diameters with sufficient modal performance are limited to 25 μm , the output power level is commonly limited by the nonlinear effect of SBS. Although the SBS threshold can be increased by suitable techniques, the desired performance will not be achieved. Therefore, the focus of this chapter was set on the advanced fiber technology of 3C[®]-fibers and for the first time the integration in proven all-fiber designs.

In Section 6.1, a first prototype of an all-fiber single-frequency amplifier using a 3C[®]-fiber with an integrated pump combiner with 2 pump ports will be presented. This design serves primarily as a first approach to investigate the optical performance. Afterwards, the corresponding experimental results of the beam quality characterization of this system are discussed in Section 6.1.2 and are used for the following improvements.

The setup of the final high-power spliceless 300 W single-frequency 3C[®]-fiber amplifier module is presented in Section 6.2 and its actual characterization in Section 6.3. Especially, the investigation of the excited HOM content inside the 3C[®]-fiber core with the 34 μm diameter at this power level is important for an application in GWDs. Additionally, the polarization properties are particularly considered. Furthermore, potential limitations such as SBS, thermal issues, parasitic lasing processes due to ASE or TMI were investigated. In addition to excellent beam quality, laser systems designed for GWDs have to exhibit a robust and reliable laser architecture, where the undesirable downtime due to disruptions should be reduced to a minimum. An automatic interlock system was developed to avoid

long-term and cost-intensive failures, which is demonstrated in Section 6.4. As a result, the required pump laser diodes can be switched off within a microsecond so that a permanent damage can be avoided and the resulting reliability of the amplifier system can be increased.

6.1 Prototype of an 170 W single-frequency all-fiber 3C[®]-fiber amplifier

As aforementioned in Chapter 4.5, the development of pump combiners was initially investigated with a passive 3C[®]-fiber with 2 pump ports using a multi-mode 106.5/125 fiber. A passive 3C[®]-fiber was chosen on the one hand because of the higher availability of this fiber type and on the other hand because of the simpler test conditions at the non-absorbed test-wavelength of 976 nm. Such a combiner was afterwards used to determine the performance of all-fiber 3C[®]-fiber amplifier pumping in a counter-propagating system. The experimental layout will be presented in the following Section 6.1.1.

6.1.1 Experimental layout

The experimental setup is separated into two amplifier stages in MOPA configuration. The first stage consists of a pre-amplifier based on a standard step-index fiber and is shown in Fig. 6.1(left). After an in-coupling stage including lenses and waveplates similar to the layout in Section 5.1, the optical beam was coupled into a SM Yb³⁺-doped PM-fiber (Yb1200-10/125DC-PM, *nLight*). The complete pre-amplifier was based on a single piece of such a 3 m long fiber and was operated in the proven counter-propagating configuration. However, it should be noted that the desired power level could be also achieved in a co-propagating architecture without an onset of SBS. The CLS based on the micro-structured cladding produced with the CO₂-laser was used to remove any residual cladding light and was directly integrated in the Yb³⁺-doped fiber enabling a cladding light suppression of typically 20 dB [Wys18]. Instead of the most common type of fiber combiner, which is based on the fiber end face pumping technique, the pump combiner was designed by using

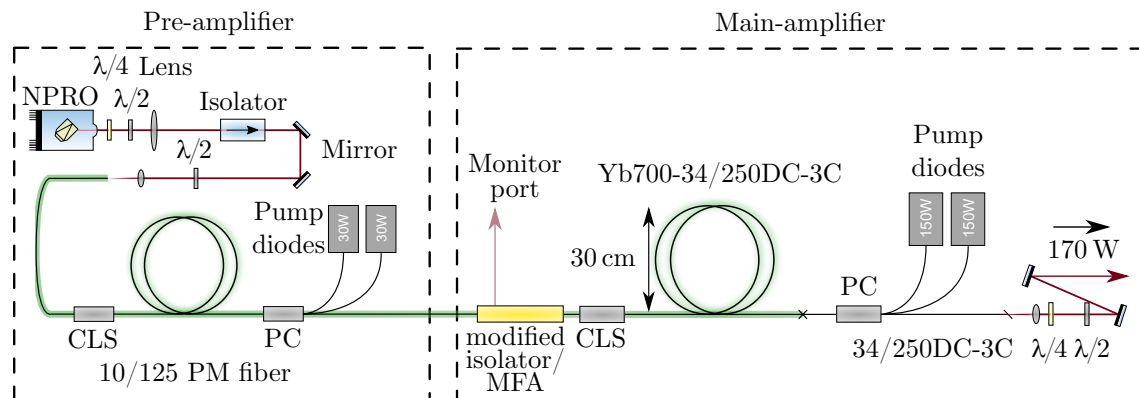


Figure 6.1: Experimental setup of an all-fiber amplifier based on a 3C[®]-fiber. The system consists of a non-planar ring oscillator (NPRO), a cladding light stripper (CLS) and a pump combiner integrated in a single-mode fiber. The Yb-doped 3C[®]-fiber is adapted to the single-mode fiber via a mode field adapter (MFA). x: splice.

the mentioned side-pump technology (see Section 4.5). Here, the light of two fiber-coupled pump diodes (BMU30-975-01-R/R02, *II-VI*) with 30 W each at 976 nm was coupled to the side of the active signal fiber. The seed signal was amplified by this pre-amplifier up to a power level of 15 W.

The interface between the pre- and main-amplifier was a home-made compact Faraday isolator with robust fiber interfaces to protect the system from backward propagating light. A detail description of this device is given in the following Subsection 6.1.1.

The main-amplifier based on a 3 m Yb³⁺-doped 3C[®]-fiber with the core diameter of 34 μm (Yb700-34/250DC-3C, *nLight*) (see Fig. 6.1(right)). The fiber had an integrated CLS produced with the CO₂-laser to ensure a sufficient pump light suppression of the counter-pumping amplifier architecture. For an efficient thermal management and maintaining beam quality, the 3C[®]-fiber was coiled on a 30 cm-diameter aluminum spool. The active 3C[®]-fiber was afterwards spliced to a passive 3C[®]-fiber with an integrated PC. Fig. 6.2 shows in (a) the alignment of the active and passive 3C[®]-fiber by a filament fusion splicer and the actual critical splice of the system is presented in Fig. 6.2(b). The alignment of the rotation of both 3C[®]-fibers to each other was achieved through the optical structure inside the fiber with an accuracy of approx. $\pm 1^\circ$.

The fiber length after the PC was chosen as short as possible taking into account technically necessary minimum parameters for the manufacturing process. The final fiber length was ~ 20 cm and the fiber end facet was angle-cleaved (see Fig. 6.2(c)).

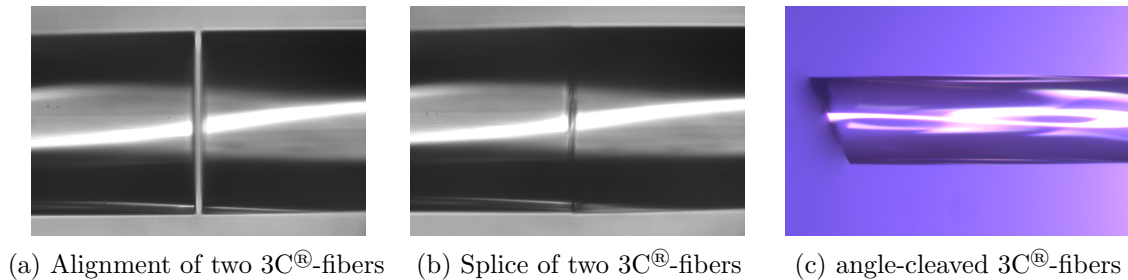


Figure 6.2: Image of the alignment of two cleaved 3C[®]-fibers in (a) and the subsequent splice in (b). In (c) an image of an angle-cleaved 3C[®]-fiber is shown.

Advanced interface device

The interface between multiple fiber amplifier stages is usually implemented by fiber-based Faraday isolators, which protects the previous amplifier stage from undesirable reflections [Tur81]. However, these devices are typically not completely fiber-based, but contain a free-space path including micro-optics inside. This proven concept was also used in the following design for an advanced 3C[®]-fiber isolator and MFA.

The component contained the 10/125 μm Yb³⁺-doped fiber from the pre-amplifier as input- and a 3C[®]-fiber as the output fiber. AR-coated fiber end caps were used as high-power connector interfaces to the isolator and were directly fused to the fibers using a CO₂-laser and are illustrated in Fig. 6.3. Such end caps protect the fiber end facets mechanically and do not degrade the beam quality. This plug-in design allowed for an easy replacement

of the main-amplifier and an integration of almost any other amplifier architecture. The actual device has the dimension of $(12.5 \times 9) \text{ cm}^2$ and consists of typical components of a fiber-based Faraday isolator: half wave plates, Faraday rotator, polarization beam splitter (PBS) and focusing optics for the coupling into the fiber (see Fig. 6.3). Additionally, two mirrors were included to enable optimization of the coupling-efficiency by the required beam walking and a quarter wave plate was added for improved polarization properties (see Section 6.3.3). Besides, the isolator had two extra monitor ports to measure the performance of the pre-amplifier and the back-scattered light from the main-amplifier. For the minimization of the excitation of higher order transversal modes, the 3C[®]-fiber was tapered similar to a mode field adapter, cleaved at the taper waist and spliced to the end cap. Therefore, the input- and output-fiber of the isolator had the same mode field area so that a 1-to-1 imaging of the beam within the isolator could be realized. The short tapered area of the 3C[®]-fiber did not show any effect of a degradation of beam quality, even if the filter effect of the side cores was minimized in this area.

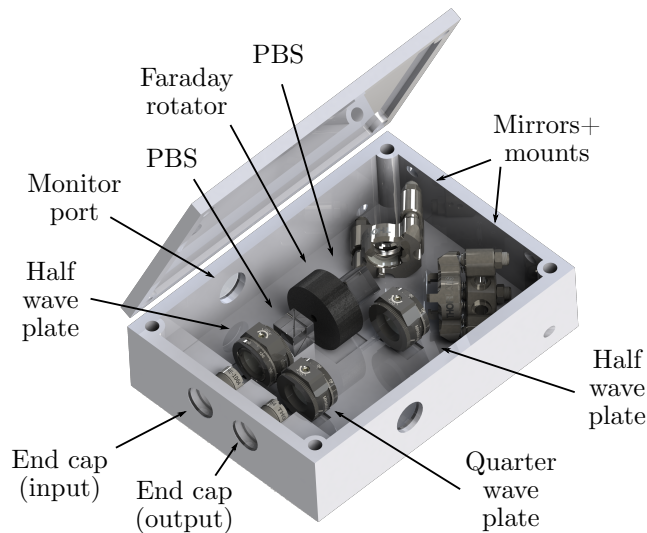


Figure 6.3: Schematic 3D-illustration of the interface between the pre- and the main-amplifier including an Faraday isolator.

A previous version of this device implemented on a simple breadboard is shown in Fig. A.1 in the Appendix. For a sufficient fiber-to-fiber coupling efficiency, the beam propagation between the fiber end facets was calculated by using the Gaussian optic. Because the pre-amplifier has an output power level of 15 W, the optical effect of the thermal lens was added in the calculations by including the heat input per infinitesimally small segment and the resulting optical lens in the medium. The propagation of such a beam with two different power levels (100 mW and 15 W) is demonstrated in Fig. A.2 in the Appendix. The calculation of the beam waist at the position of the 3C[®]-fiber influenced by the different heat input in the medium is presented in Fig. 6.4 in red. With an increasing power level of the pre-amplifier, the position of the beam waist at the same lens position is changed by

the induced lens effect. Thereby, the optical losses (blue) depend on the input power and are determined by the overlap of the beam diameter at the position of the fiber end facet and the MFD of the fiber. The entire device is optimized, so that minimum optical losses of <2 dB were achieved at the operating power level of 15 W.

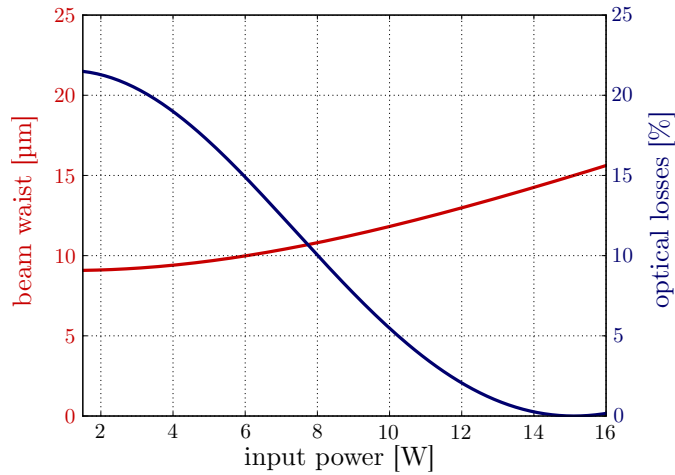


Figure 6.4: Theoretical calculation of the beam waist at the position of the 3C[®]-fiber end facet (red) at different input power levels of the pre-amplifier and the corresponding optical losses (blue) in %. The device is optimized for the operating power level of 15 W.

Finally, this architecture combines the advantages of two optical fiber components: a fiber-based isolator and a mode field adapter using specialty fibers. Considering the beam propagation including the effect of the thermal lens, the component is designed for the operating power level of the pre-amplifier and additionally, enables the monitoring of each amplifier stage.

6.1.2 Beam quality characterization

As already mentioned, this all-fiber amplifier based on the 3C[®]-fiber was designed to determine the performance of such a counter-propagating amplifier architecture. Therefore, only the most essential results of the characterization are examined here. A complete characterization of the final high-power amplifier design is discussed in detail in Chapter 6.3.

The amplifier output power is plotted versus the absorbed pump power in Fig. 6.5. Assuming a pump light absorption of ~90%, an optical-to-optical efficiency of 75% was determined at the maximum amplifier output of 172 W limited by the available pump power. Based on the seed signal power, a gain level of 19.3 dB is reached in this amplifier system.

At the highest available pump power level, the output power of the free-running 3C[®]-fiber amplifier was detected with an average power of 170.5 ± 0.3 W over 6 hours and is shown in Fig. 6.6(b) in red. Additionally, separated by a polarization beam splitter (PBS) the s- and p-polarized light of the beam were measured to calculate the PER of the system. The result is also shown in Fig. 6.6(b) in blue, where an extinction ratio of 17.8 ± 0.1 dB was achieved. In the warm-up time of ~1 hour, the output power level increased slightly from 170.2 W

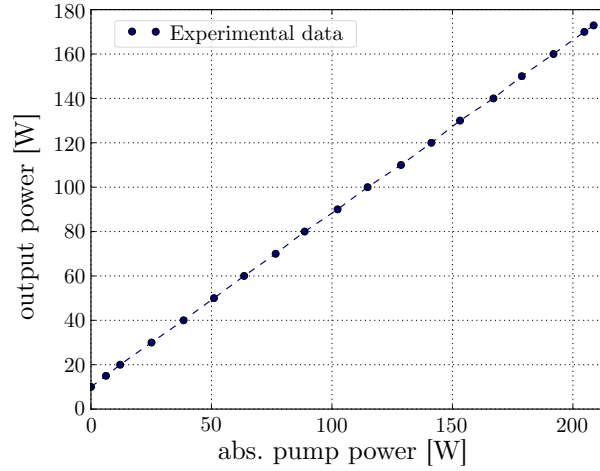


Figure 6.5: Slope of the 170 W 3C[®]-fiber amplifier with an optical efficiency of the absorbed pump power to optical output power of 75%.

to 171.1 W, which is known for fiber amplifiers, especially, for Yb:Er-codoped amplifier designs [Var17b]. Afterwards, the system reached a constant value of around 170.5 W. The reasons for this slight decrease cannot be clearly determined, especially not on these time scales. Correspondingly to the fluctuations of the output power, the PER decreases slightly similar to the performance curve probably due to the changed temperature conditions inside the fiber without an realignment of the wave plates. Subsequently, the PER level was at a stable value of 17.8 dB.

The beam quality was determined by using the above mentioned DBB. The normalized intensity is shown in dependence on the FSR on a logarithmic scale in Fig. 6.6(a). In addition to the known peaks at 0.15 FSR, 0.3 FSR and 0.65 FSR (see Section 5.2.2), the mode scan at an output power level of 170 W exhibits a significantly larger number of

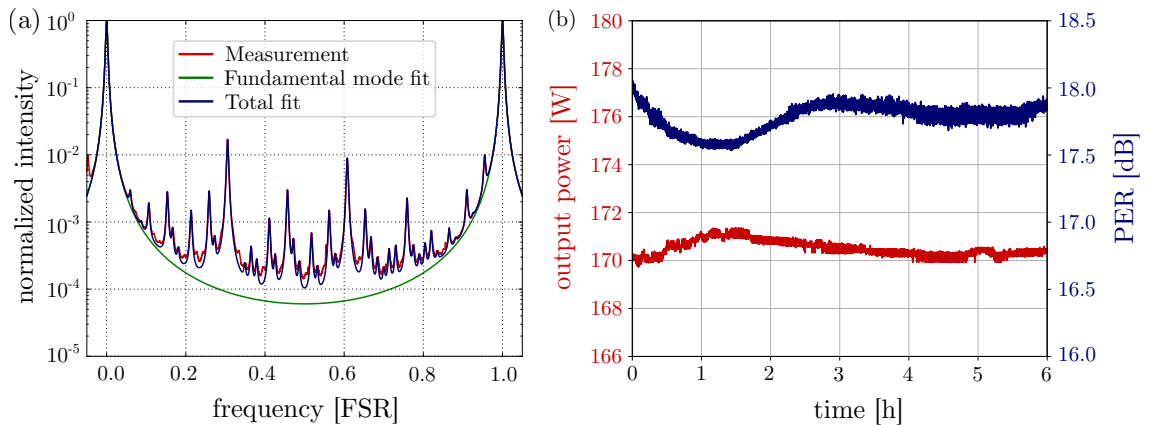


Figure 6.6: Slope of the 3C[®]-fiber amplifier with an optical efficiency of the absorbed pump power to optical output power of 75%.

peaks compared with the mode scan displayed in Fig. 5.6. This fact can be based on different physical reasons: Although this fiber amplifier system also has a MFA to avoid the generation of HOMs, the beam of the pre-amplifier is free-space coupled into the tapered 3C[®]-fiber, which can lead to the generation of HOMs by a slight misalignment. Another explanation is that HOMs created in the last few centimeters of the fiber system due to the large core diameter can not significantly interact with the side core of the remaining 3C[®]-fiber. Additionally, the induced heat load can also influence the amount of HOMs as reported by Zhu et al. [Zhu19]. Finally, this content of HOMs remains in the 3C[®]-fiber core and decreases the beam quality of the laser beam. Nevertheless, the system showed an excellent fundamental mode content of 94.4% at the maximum output power level. In total, taking into account the HOM content and the power in the wrong state of polarization, the overall output power in the linearly polarized TEM₀₀-mode was 157.7 W.

6.1.3 Conclusion

This first approach of an all-3C[®]-fiber amplifier was designed to determine the performance of such a system with a pump combiner integrated in a passive 3C[®]-fiber with 2 pump ports pumping in counter-propagation. At the maximum available pump power, this amplifier architecture achieved a stable optical output power level of 170 W at an excellent beam quality with 5.6% HOMs and 157.7 W in the linearly polarized TEM₀₀-mode.

Based on these results, the designed optical components in 3C[®]-fibers have been improved regarding their use in high-power all-fiber amplifiers. Especially, the pump combiner has been enhanced and two additional pump ports have been added. In addition, the overall coupling efficiency of the pump light into the fiber has been optimized by adjusting the respective manufacturing parameters.

The experimental setup of such a amplifier system with an advanced pump combiner with four pump ports will be presented in the following Section 6.2.

6.2 Experimental layout

The realized high-power 3C[®]-fiber amplifier system in MOPA configuration consisted of a two stage design (pre- and main-amplifier) operating at 1064 nm and is shown in Fig. 6.7. The architecture of the pre-amplifier consisting of the proven NPRO (*Innolight* Mephisto 2000NE) and the standard SM Yb³⁺-doped PM-fiber (Yb1200-10/125DC-PM, *nLight*) is already known from Section 6.1.1. Here, the experimental results of the pre-amplifier are discussed for the first time in the following Section 6.3.1. As in the previous setup, the pre-amplifier increased the signal light from 1.4 W coupled into the standard fiber to a power level of 15 W by using the pump light of two fiber-coupled pump diodes (BMU30-975-01-R/R02, *II-VI*) with 30 W each at 976 nm.

Section 6.1.1 describes the interface device between the pre- and main-amplifier based on a home-made compact Faraday isolator with robust fiber end caps connections. Such a proven component is also used in this high-power amplifier system and is the direct interface to the 3C[®]-fiber via an AR-coated fiber end cap. The monitor ports based on an included PBS were used to measure the performance of the pre-amplifier and to analyze the back-reflection of the main-amplifier.

The main-amplifier module consisted of a single 3 m Yb³⁺-doped 3C[®]-fiber with a core

diameter of 34 μm (Yb700-34/250DC-3C, *nLight*). As for the pre-amplifier, all necessary optical components were directly integrated into the 3C[®]-fiber to ensure an optimal beam quality without additional losses due to splices. The larger core diameter of the 3C[®]-fiber compared to standard LMA fibers has the benefit of an increased SBS threshold. For an even higher SBS threshold, the amplifier was operated in counter-propagating configuration with the advantages of an improved pump-induced thermal gradient along the fiber, which additionally increases the SBS threshold compared to a co-propagating configuration [Hil08] and the reduced effective interaction fiber length.

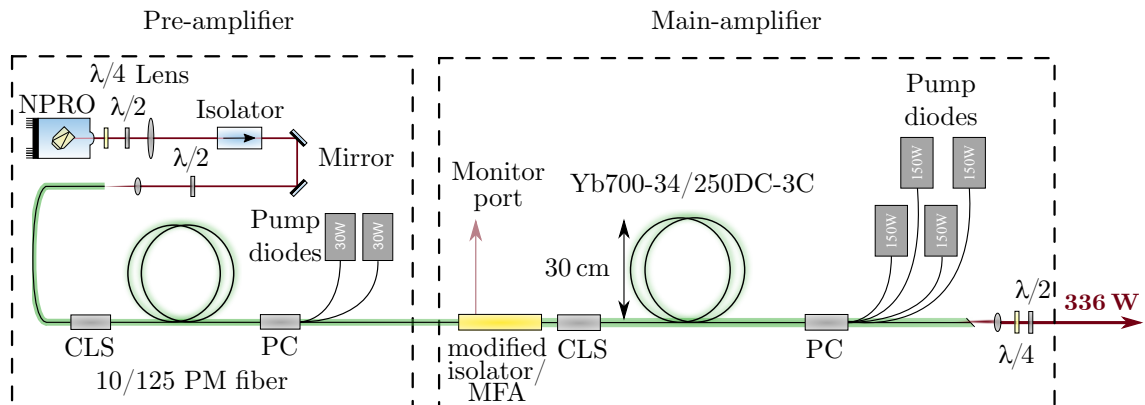


Figure 6.7: Experimental setup of a high-power all-3C[®]-fiber amplifier with an output power level of 336 W. The system in MOPA configuration consists of a non-planar ring oscillator (NPRO) as seed laser, a standard-fiber pre-amplifier and a main-amplifier based on a Yb-doped 3C[®]-fiber with an integrated high-power pump combiner. CLS: Cladding light stripper, PC: pump combiner, MFA: mode field adapter.

The key component of this spliceless amplifier system was the high-power signal and pump combiner operating in counter-propagating configuration. The advancement from two to four fiber pump ports doubles the available optical pump power of the entire amplifier system. Using the side-pumping technique the pump light was coupled via the outermost cladding surface into the 3C[®]-fiber with a pump light coupling efficiency of $>70\%$. As already mentioned, the key advantage of this technology was the uninterrupted helical structure and the elimination of the need for an additional fusion splice in conjunction with signal mode matching, which was shown for the first time. The required optical pump power was provided by four fiber coupled laser diodes (K976FN1RN-150.0W, *BWT*) with an optical output power of 150 W each at 976 nm spliced with a matched core diameter of 106.5 μm to the input pump fibers of the pump combiner.

The residual light in the cladding of the 3C[®]-fiber was suppressed by a further in-house made CLS. The CLS was directly integrated into the active 3C[®]-fiber and achieved a suppression of 19 dB. For an optimal suppression of propagating pump light, the grooves were generated on different sides of the fiber in the manufacturing process. The used 3C[®]-fiber has a nominal absorption of 2.15 dB/m at 920 nm and has been coiled on an aluminum spool with 30 cm diameter for thermal management. The temperatures of the significant components such as the spool, the pump combiner or cladding light stripper were

captured by an automatized programmable logic controller (PLC) produced by *Beckhoff Automation GmbH & Co. KG*. Additionally, the drivers of the pump diodes were controlled via this system, so that the entire amplifier module could be managed remotely.

6.3 Beam characterization

The characterization of the beam quality of the high-power spliceless 300 W single-frequency 3C[®]-fiber amplifier module is separated into various sections. First of all, the performance of the pre-amplifier will be discussed in Section 6.3.1. Afterwards, the decisive parameters of the optical slope and the PER, of the longterm-stability, of the modal content and of the relative power noise will be represented in following sections. Limitations due to nonlinear effects in the form of transverse mode instabilities and of stimulated Brillouin scattering will be characterized in Section 6.3.7 and in Section 6.3.8.

6.3.1 Experimental results of the pre-amplifier

In case of a small optical signal power, a desired high gain at a corresponding small noise figure value cannot commonly be reached due to an increased ASE level. Therefore, pre-amplifiers are typically used in fiber amplifier architectures to amplify the input signal to a sufficiently high power level and to avoid high gain factors of much more than > 20 dB. For this reason, a pre-amplifier was also integrated in this design.

The output power versus the injected pump power at 976 nm is plotted in Fig. 6.8. At a working point of a signal output power of 15 W, a pump power of ~ 18 W is required. With this fiber amplifier design, a higher output power level would also be possible, but was not used due to the increasing effect of the thermal lens and the laser-induced threshold inside the advanced interface device (see Section 6.1.1). In addition, no further amplification of the power level by the pre-amplifier is necessary, because no significant increase of the final ASE level could be observed in the optical spectrum. Finally, the pre-amplifier achieved an optical-to-optical efficiency of 82%, which is typically for such fiber amplifier systems known from the literature [Wel19].

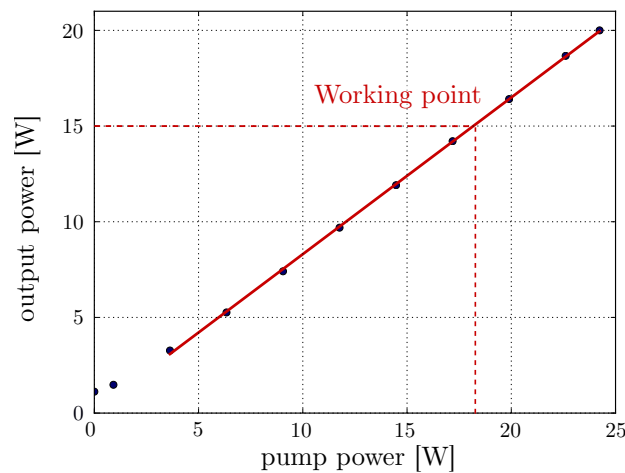


Figure 6.8: Slope of the used pre-amplifier with measured data (blue dots) and a linear fit (red line) with an optical-to-optical efficiency of 82%.

For a stable performance of the entire fiber amplifier system, the stability of the pre-amplifier is essential. Therefore, the optical output power of the pre-amplifier was measured over a time scale of one day. The experimental results are shown in Fig. 6.9 in red. The pre-amplifier exhibited a stable optical power level of 15.01 ± 0.05 W (corresponding to fluctuations of 0.3%).

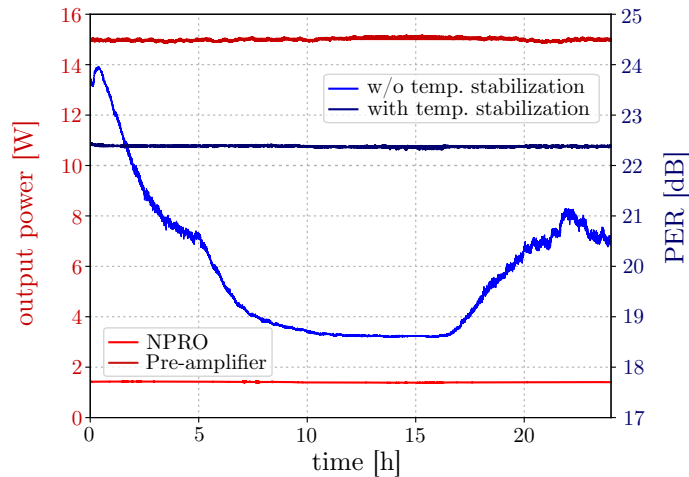


Figure 6.9: Evolution of the optical output power level of the pre-amplifier over a time scale of one day in red. Additionally, the corresponding results of the PER in blue with and without a temperature-stabilized spool.

The fiber of the pre-amplifier was coiled on an aluminum spool with a diameter of 15 cm. Without a temperature stabilization of this spool, the resulting PER showed significant fluctuations from a starting value of 24 dB to less than 19 dB at a local minimum between 10 and 15 hours (see Fig. 6.9 blue curve). Only a stabilization of the spool temperature and the associated constant temperature behavior within the fiber enabled to stabilize the PER at a value of 22.42 ± 0.01 dB determined over the entire time scale.

Based on these parameters, the input signal from the seed source could be increased by this pre-amplifier to a stable power level which allowed a sufficient saturation of the 3C[®]-fiber core.

6.3.2 Optical Slope and Spectrum

The spliceless 3C[®]-fiber amplifier module enabled a high-power output power level far beyond the limitations of standard LMA fibers. The measured optical amplifier output power versus the pump power is demonstrated in Fig. 6.10(a). With an absorbed pump to signal efficiency of $\sim 80\%$ and a coupling efficiency of the pump combiner of $\sim 70\%$, the amplifier system reached a maximum output power of 336 W. By further increasing the coupling efficiency of the pump combiner, even a higher output power level is possible. As typically known from fiber amplifiers, the experimental results of a low efficiency at lower pump power levels were caused by the shifted center pump wavelength away from the absorption maximum of Yb^{3+} at 976 nm. A compensation at these power levels was only partially possible by an adjustment of the diode temperature. Because the final operation

point is far above this point, no further temperature adjustment is required.

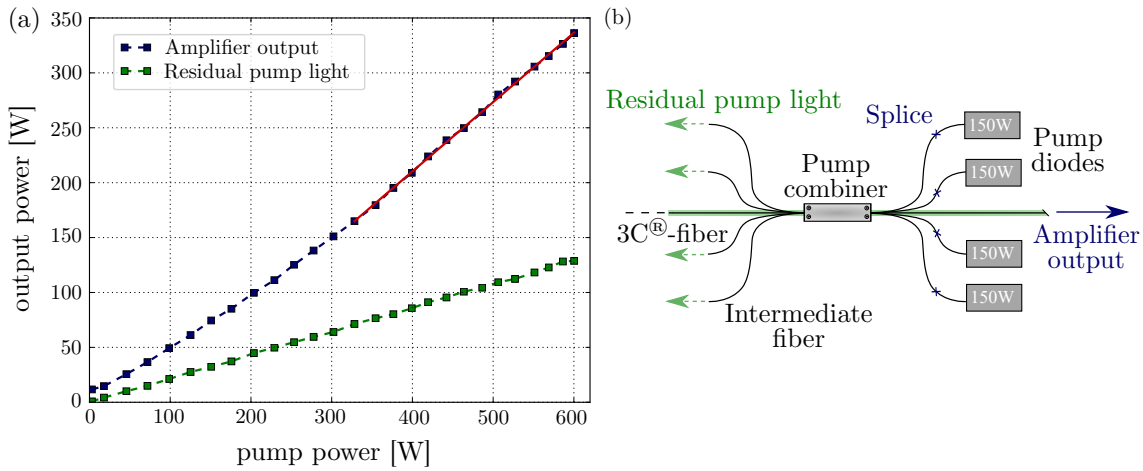


Figure 6.10: (a): Slope of the amplifier with measured data (blue squares) and a linear fit (red line). The residual pump light of the pump combiner is shown in green. (b): Pump combiner integrated in the 3C®-fiber with different fiber outputs for the non-transferred pump light.

Due to the coupling efficiency of $\sim 70\%$ of the pump combiner, a certain amount of pump light could not be used in the amplification process. The amount of the residual pump light remaining in the intermediate fibers was $\sim 22\%$ of the total diode power (see Fig. 6.10(a) and (b)). Accordingly, some residual pump light was lost in different ways in the pump combiner [The12b], which results in heating of the combiner housing. Therefore, the pump combiner was actively water-cooled by a specially designed cooling plate for thermal management. However, if too much pump light is guided into the coating and it reaches a

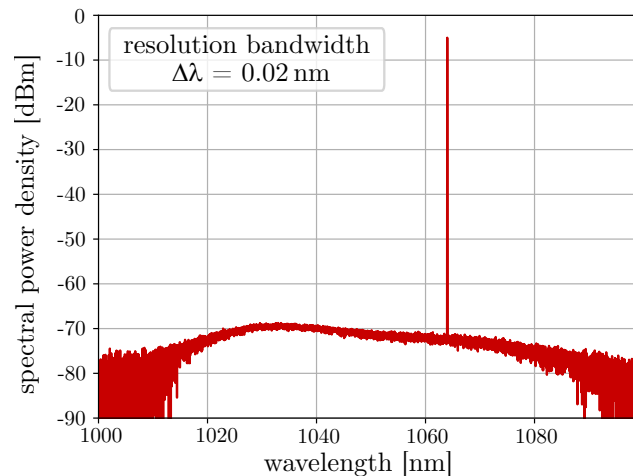


Figure 6.11: Optical spectrum at the maximum output power level of 336 W with a resolution bandwidth of 0.02 nm.

certain temperature threshold ($>80^{\circ}\text{C}$), the component is usually irreversibly damaged. The optical spectrum of the amplifier system at the maximum output power level of 336 W is depicted in Fig. 6.11. In a bandwidth range from 1000 nm to 1100 nm, the Yb^{3+} -ASE was slightly above the sensitivity level of the spectrum analyzer with an ASE-suppression of more than 63 dB.

6.3.3 Polarization extinction ratio

The polarization extinction ratio bases on the description of light as an electromagnetic wave. In case of linearly polarized light, the phase difference between the two orthogonal states is typical 0° or 180° . However, if the laser light is coupled into a SM fiber, the linear polarization is transformed into an arbitrary polarization. Due to a relatively strong induced birefringence, a PM fiber enables the polarization state to be maintained. Compared to PM fibers, the 3C[®]-fiber has a weak intrinsic birefringence and no additional stress rods inside the cladding. Twisting the 3C[®]-fiber preform during its manufacturing process removes any residual weak birefringence [McI78].

Indeed, the PER of the beam after the amplifier system was only slightly affected as also previous measurements showed [Zhu11]. For this system, Fig. 6.12 presents the PER of the optical beam at different output power levels of the pre- and main-amplifier over a 30 minutes-measurement. Exclusively, the pre-amplifier is based on a standard PM fiber exhibited a stable PER of (24.2 ± 0.4) dB, which was reduced over the measurement duration to (22.0 ± 0.4) dB. After the 3C[®]-fiber of the main-amplifier, the PER worsens at low main amplifier power to 17-19 dB due to the missing polarization-maintaining properties of the 3C[®]-fiber. At the maximum output power of 336 W the PER was reduced from (17.1 ± 0.8) dB to a stable PER of (13.4 ± 0.7) dB, which resulted in an unusable polarization of approximately of 15 W. However, as long as the PER is stable over the long term, the additional losses are not critical and will not couple in power fluctuations after transmission through polarizing optical components or optical resonators.

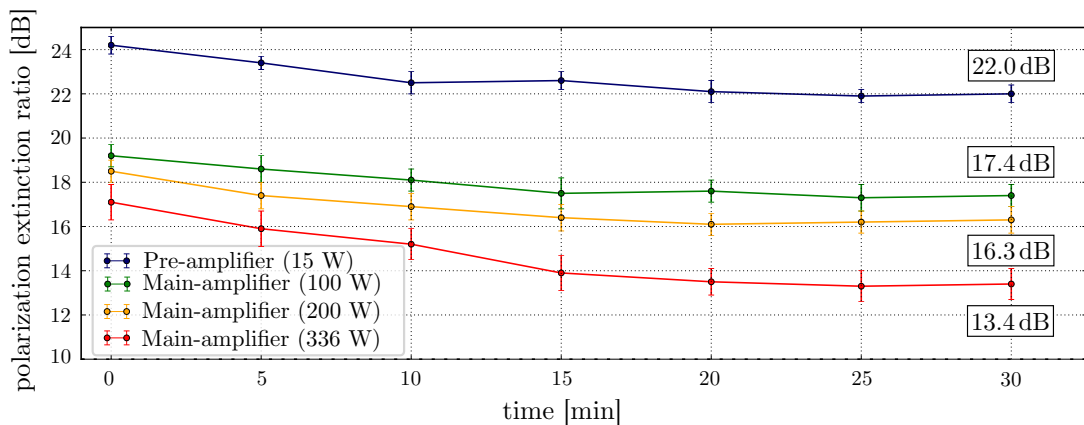


Figure 6.12: Evolution of the polarization extinction ratio of 3C[®]-fiber main-amplifier and the pre-amplifier at different output power levels over 30 minutes.

In the experimental setup, the 3C[®]-fiber was coiled on a aluminum spool with a diameter of 30 cm. The weak coiling-induced birefringence influences the stability of the PER as well as other external environmental impacts. Even if such polarization instabilities have not been observed yet, a torsion-free winding of the fiber would probably favor the long-term stability.

Besides, the spool was not actively temperature stabilized. Thus, any thermal drifts in the temperature couple directly to the fiber and can induce an additional birefringence inside the fiber. This can lead to further polarization instabilities.

However, the 3C[®]-fiber amplifier has shown a very robust and stable polarization output. An engineering prototype of this laboratory setup will have to validate these results in the long-term period.

6.3.4 Power stability in operation

For a variety of applications, also next to GWDs, the power stability and reliability is essential in high-power operation. Therefore, the output power of the free-running amplifier system is shown in Fig. 6.13 in red in a continuous operation of the laser over 5 hours. The optical power was sampled once per second using a high-power water cooled thermal sensor 1000W-BB-34 (*Ophir Optronics*). The measurement includes a warm-up time of approximately 1-2 hours, where the output power increased by 3.8% from 325 W to 336 W.

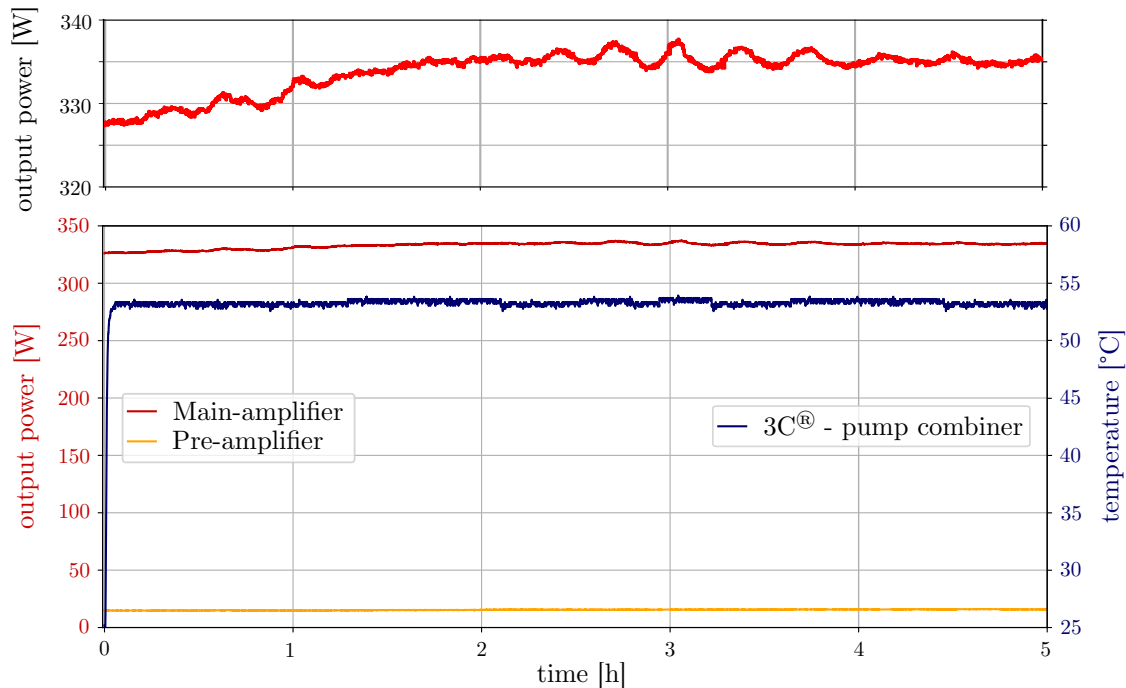


Figure 6.13: Long-term power stability measurement of the 3C[®]-fiber amplifier at an output power of 336 W in red and the corresponding pre-amplifier in orange. Additionally the behavior of the output power at 336 W is shown in detail in the upper plot. The temperature of the high-power pump combiner integrated in the 3C[®]-fiber is shown in blue.

Additionally, some power oscillations were observed during this test. External temperature fluctuations can couple from the non-temperature stabilized fiber spool to the gain process inside the 3C[®]-fiber and can lead to such oscillations. Besides, the performance of the pre-amplifier after propagating through the main-amplifier was monitored (Fig. 6.13, orange). In addition to the output power of the system, the temperature of the high-power pump combiner in the 3C[®]-fiber was logged and is shown in Fig. 6.13 in blue. After a warm-up time, the housing of the combiner reached a constant temperature of $\sim 52 \pm 2^\circ\text{C}$. All in all, the 3C[®]-fiber amplifier achieved an average output power during the operation test of (336.3 ± 2.7) W with a relative standard deviation of $<1\%$ after the warm-up time.

6.3.5 Modal content analysis

The application of GWDs can only utilize a pure TEM₀₀-mode in a linearly polarized beam in the interferometer, where a polarizing pre-mode cleaner cavity is integrated to suppress any HOMs. It is therefore essential that the designed laser systems for the next generation of GWDs ensure a consistently high fraction of the TEM₀₀-mode in order to prevent a potential conversion into power noise. As already mentioned, the characterization of the M²-value does not guarantee a pure single mode operation, as even an M² <1.1 can contain up to 30% of HOMs [Wie07].

The method of beam quality characterization of amplifier or laser systems discussed in Section 5.2 relies on a scanning ring-cavity as described by Kwee et al. in [Kwe07]. With a fused silica wedge, an amount of 4% of the high-power beam was sampled for the measurement of the beam quality. Furthermore, this characterization beam was adjusted to the required low power level of ~ 100 mW via a power tuning stage consisting of a half wave plate and a PBS. For the optimization of the mode matching into the cavity, the beam propagation was calculated by using the Gaussian optic to realize the optimal combination of lenses for the mode matching.

By scanning the piezo attached to one of the mirrors over a FSR, the frequency of the eigenmodes of the ring-cavity changes and the resulting normalized intensity in dependence of the cavity length over one FSR of the cavity is presented in Fig. 6.14(a). Thereby, each data point was an average of 100 measurements to reduce effects of short time fluctuations. The averaged samples were used to fit functions of the fundamental Gaussian mode (green) and the total fit including a sum of fundamental and HOMs with variable coefficients (blue), where the ratio of the coefficients of these two fits determines the relative TEM₀₀ mode content. By comparing the fits, inaccuracies in the measurement due to bad mode-matching to the cavity, potential amplified spontaneous emission (ASE) or residual unpolarized light could be minimized. At an output power level of 336 W the amplifier showed a modal content of 90.4% of the power in the fundamental mode, where the resulting image of the beam is presented in Fig. 6.14(b).

The mode scan exhibits several peaks in the measurements due to beam misalignment or mode mismatching to the cavity. The highest peak at 0.3 FSR corresponds to mode mismatching by the used lens combination and could not be further minimized through changing the lens positions and focal lengths. Additionally, the relative misalignment in vertical and horizontal direction were optimized by reducing the peaks at 0.15 FSR and

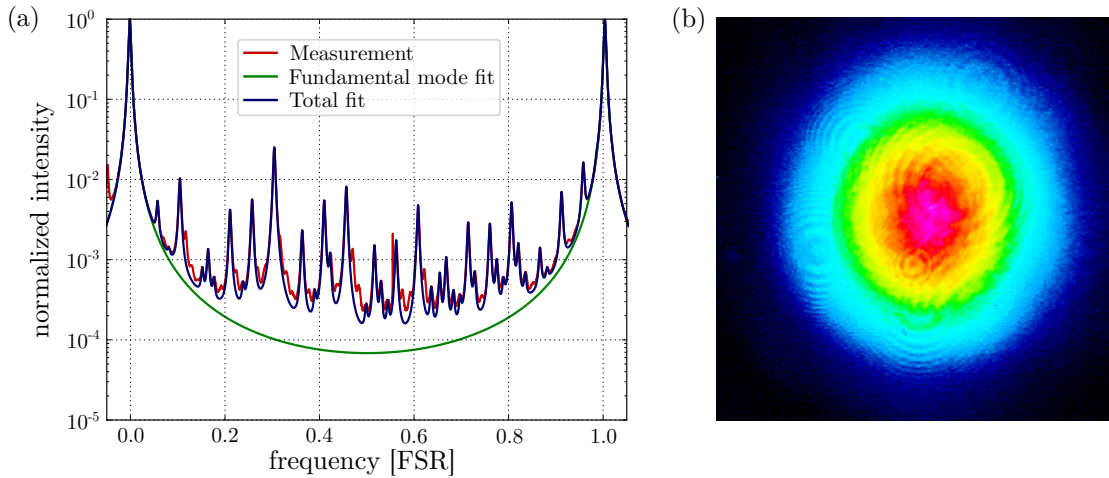


Figure 6.14: (a): Mode scan at an output power of 336W with a fundamental mode content of 90.4%. The normalized intensity is shown in dependence of the cavity length over one free spectral range of the ring-cavity. (b): Image of the beam profile measured with a CCD camera.

0.65 FSR.

The fundamental mode content is not constant over the output power of the 3C[®]-fiber amplifier. Therefore, the corresponding TEM₀₀ mode content was measured at different output power levels and is shown in Fig. 6.15. When only operating the pre-amplifier at a power level of ~ 15 W (main amplifier stage off), a fundamental mode content of 97.9% was measured. Over the entire output power slope, the beam quality decreased to a TEM₀₀ mode content of 90.4% at the maximum output power level of 336 W. Thereby, the alignment into the cavity was readjusted each time the output power was increased to minimize the influence of thermal lensing and other effects. At 100 W of output power, the resulting TEM₀₀ mode content of 97.5% is comparable to the determined beam quality of

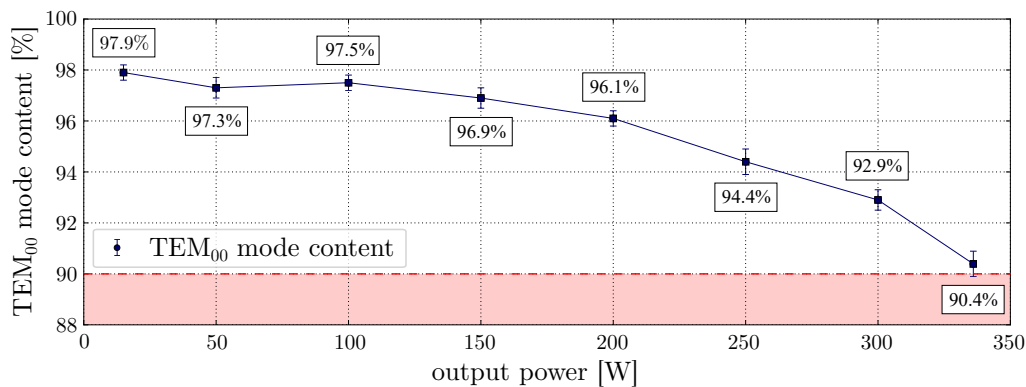


Figure 6.15: TEM₀₀-mode content of 3C[®]-fiber main-amplifier at different output power level. All measurements are above the requirements for GWDs of a TEM₀₀ mode content of more than 90% [Abe11].

the first 100 W-prototype demonstrated in Chapter 5.2.2. The fundamental mode content of 96.1% at 200 W exceeded the previous highest measured TEM₀₀ mode content of 94.7% in conjunction with single-frequency lasers or amplifiers [Wel19]. The observed slight decrease of the beam quality can be explained e.g. by the induced heat load and the impact on the modal loss reduction as reported by Zhu et al. [Zhu19]. At all measurements of the evolution of the beam quality, the fundamental mode content was above the requirements (TEM₀₀ mode content > 90% [Abe11]), which additionally emphasizes the high potential of fiber amplifiers based on 3C[®]-fibers as laser sources for the next generation of GWDs.

6.3.6 Relative power noise

Laser sources for GWDs have to exhibit low power noise characteristics, because power fluctuations directly couple to the read-out signal of the detectors at all frequencies, especially where the sensitivity is limited by the shot noise of the laser system. In addition, due to the fundamental frequencies of gravitational waves, the RPN in the frequency range from 1 Hz to 100 kHz is relevant for the ground-based interferometers. Therefore, the RPN of the free-running laser system was analyzed up to a power level of 336 W. The utilized photodiode (PDA10CF, *Thorlabs*) was a InGaAs detector with a 150 MHz bandwidth and the signal was analyzed with a SR785 (Stanford Research Systems) for FFT measurements. In Fig. 6.16, the RPN at the maximum power of the free-running amplifier system is compared to the measurements of the previous used 200 W solid state laser-system developed for the aLIGO Hanford Observatory [Wil12].

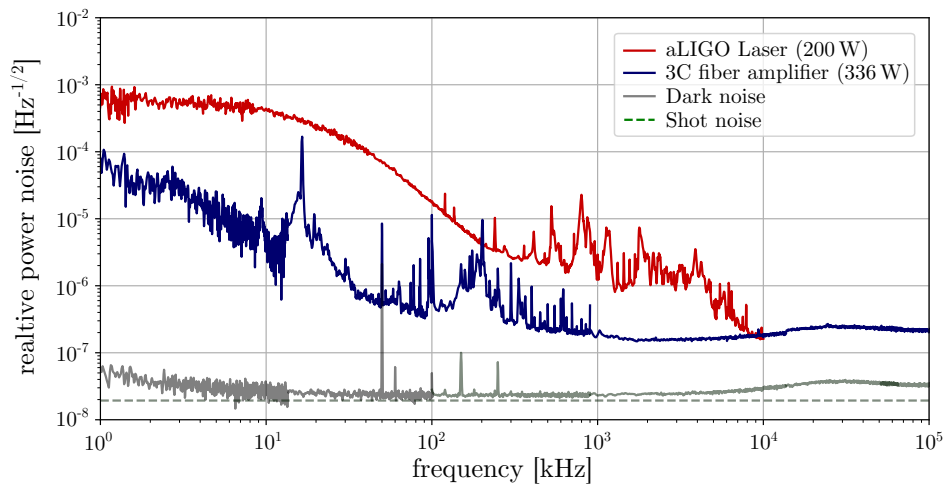


Figure 6.16: Relative power noise measurements of the 3C[®]-fiber amplifier system in comparison with the 200 W solid-state laser developed for the aLIGO detectors.

The presented fiber amplifier architecture with a spliceless all-fiber design based on 3C[®]-fibers exhibits a suitable RPN at all frequencies for the use in GWDs. These results confirm the characteristics of low RPN of fiber amplifier system determined in previous investigations [The15; Var17b; Wel19]. Especially below 100 Hz, the measured RPN of the amplifier is up to two orders of magnitudes lower compared to the RPN of GWD laser

systems [Win11]. At higher frequencies above 10 kHz, the RPN of both systems achieved similar noise levels. The RPN in this frequency range is determined by the NPRO as seed source, which was used in both laser systems.

Thereby, the RPN characteristic was analyzed in a free-running laser system. The already very low RPN level of this 3C[®]-fiber laser system can be further reduced by active power stabilization control schemes via e.g. pump power modulations as demonstrated by Thies et al. [Thi19]. Furthermore, the proven technique of laser stabilization by an integrated AOM after the high-power cw Nd:YAG laser system [Kwe12] can also be used and thus opens up further possibilities of laser stabilization.

6.3.7 Transverse mode instabilities

High-power fiber amplifiers operated at power levels of hundreds of watts can exhibit a kind of mode instability that the beam quality of the output decreases significantly above a certain threshold value [Smi11]. This effect of transverse modal instability (TMI) appears by using not purely single-mode fibers, where a small number of modes are guided in the fiber core as it is typical for high-power fiber amplifiers with integrated LMA fibers. In recent years, TMI has come into the focus of research and has been extensively studied [Joh13]. According to current knowledge, an induced thermal load and thermal gradient within fibers is the decisive physical parameter of the phenomenon of TMI. Jauregui et al. estimated a parameter of thermal load to the onset of TMI of around 34 W/m applicable to specific fiber geometries [Jau15].

In Section 6.3.2, the presented characteristic slope of the spliceless 3C[®]-fiber amplifier system had an optical-to-optical efficiency of $\sim 80\%$. Considering the estimated unabsorbed pump power of ~ 20 W, additional pump light losses in the pump combiner housing of $\sim 8\%$ and remaining pump light in the intermediate fibers of the pump combiner, the thermal load inside the 3C[®]-fiber was calculated to be < 22 W/m. Thereby, further signal losses

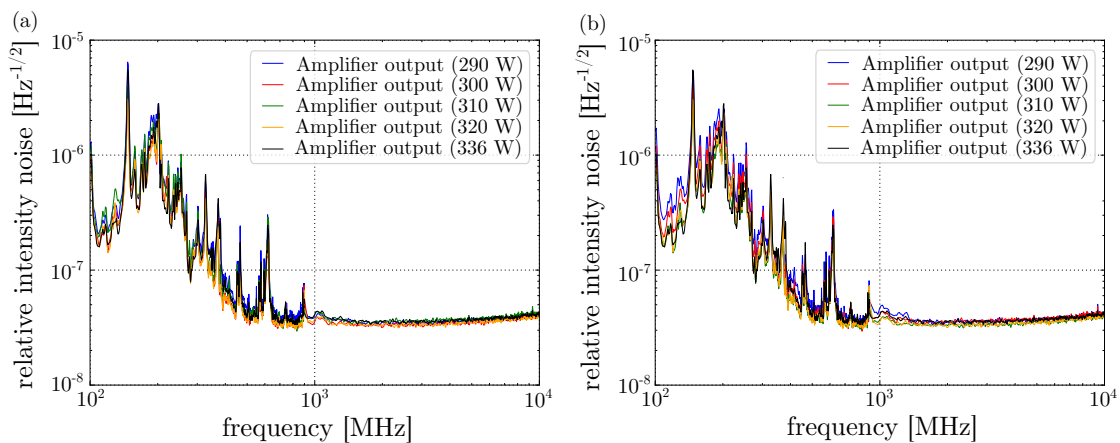


Figure 6.17: (a): Relative power noise spectra at different output power levels without an aperture in the sampled beam. (b): Relative power noise spectra with an aperture in the sampled beam to convert modal fluctuations into power fluctuations.

due to the collimating lens, dichroic mirrors or other effects are not included. Thus, the thermal load of the 3C[®]-fiber is below the introduced TMI limit.

Apparently, the HOM content of the laser system has a perceptible impact of onset of TMI [Joh13]. Here, the 3C[®]-fiber plays a special role, because it actively suppresses HOMs by its geometrical design and it should significantly increase the threshold of TMI. This influence of the 3C[®]-fiber geometry on the TMI threshold opens a new research field for further investigations and could be interesting for a variety of such fiber-based applications and high-power fiber amplifiers.

Although the value of the thermal load inside did not exceed the threshold of TMI, the behavior of the amplifier system was experimentally investigated by using the method described by Karow et al. [Kar13]. The RPN was measured with and without an optical aperture in the beam path in front of the InGaAs photodiode in the frequency range of 100 Hz to 10 kHz. Above the TMI threshold, an excess RPN should be observable in discrete noise peaks in a 500 Hz-5 kHz frequency range or, far above the TMI threshold, in a broadband excess chaotic RPN similarly as it is known from the nonlinear effect of SBS (see Chapter 3).

In Fig. 6.17, the RPN is presented in this frequency range with (a) and without (b) an aperture, whereby due to the aperture, modal fluctuations are converted into power fluctuations. Between both measurements the RPN at different output power levels does not show any significant differences in this frequency regime, neither discrete peaks nor a broadband excess RPN. The influence of the 3C[®]-fiber design on the threshold of TMI at higher power levels is an interesting research field and implies a high potential for future fiber amplifier systems.

6.3.8 Stimulated Brillouin scattering

Single-frequency laser or amplifier systems are mainly limited by the onset of SBS [Hil08]. The SBS threshold can be determined by several approaches, such as the common method of monitoring the backwards propagating light or monitoring the relative power noise at high frequencies. Here, the effect is exploited that SBS imprints a broadband excess power noise in forward direction at MHz-frequencies [Hor97]. This method is the most sensitive technique to determine the onset of SBS [Hil08].

For application in GWDs, the MHz-regime is also relevant and cannot be neglected. In the interferometer this frequency range is used for length and alignment stabilizations. Here, modulation side bands are imprinted on the signal beam, which also require a low power noise at these frequencies [Izu17].

Fig. 6.18 represents the relative power noise measured in the frequency range up to 30 MHz at different output power levels. The spectrum was detected with a spectrum analyzer E4440A (*Agilent*) and the utilized photodiode (PDA10CF, *Thorlabs*) was an InGaAs detector with 150 MHz bandwidth. The intrinsic stability of the NPRO as seed source could be further improved by an additional integrated Noise Eater (NE) technology, which suppresses the relaxation oscillation peak of the NPRO. The differences in the Fourier spectrum using a NE or not are shown in Fig. 6.18 (a) and (b). In (b) the NE was switched off and the relative power noise is almost unchanged up to a power level of 300 W and then increases slightly up to the maximum power of 336 W. From this it can be concluded

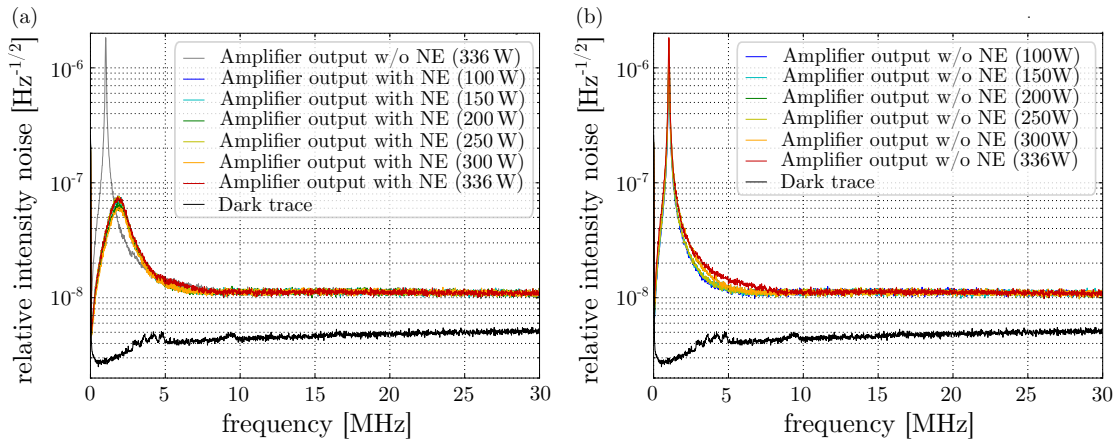


Figure 6.18: Relative power noise spectra at different power levels up to a frequency range of 30 MHz. a): With an additional integrated Noise Eater (NE) technology. b): Without a NE. At 336 W a slight noise increase in the 5 MHz range can be detected.

that the amplifier system might have shown the first onset of SBS at these power levels. In the spectrum in (a) the NE of the seed source was switched on. Here, the increase of the relative power noise is not clearly recognizable as in (b) due to the slight excess power noise in the frequency range of 2-3 MHz caused by the NE control loop of the NPRO. However, there is no impact of SBS recognizable in the slope in Fig. 6.10 and the amplifier system has no additional integrated techniques to suppress SBS yet. Thus, the SBS-threshold can be further increased by introducing a thermal gradient on the fiber to broaden the SBS gain spectrum [Liu09a]. In the experimental setup, this technique can be implemented by using two fiber spools at different temperatures, which was successfully integrated in the fiber amplifier system for the next generation of GWDs designed by Theeg et. al [The15]. Indeed, the number of possible windings on two spools is limited in 3C[®]-fiber amplifier architecture by the fiber length and the required coiling diameter of 30 cm. Thus, a ratio of windings on two spools of maximum 1:2 can be practically achieved to generate a thermal gradient. The influence of this technique will have to be tested and can be integrated in a further improved engineering prototype of this 3C[®]-fiber amplifier to achieve an even higher SBS-free output power. In addition, 3C[®]-fibers with a larger core diameter (e.g. 55 μm instead of 34 μm) are an effective method of significantly increasing the SBS threshold by more than a factor of 2.5.

6.4 Enhanced reliability through interlock system

For all class 3B and 4 lasers, regardless of the final application, the use of an interlock system is required in accordance with EN / IEC 60825-1. The mechanism of an interlock is to automatically turn off the laser system to ensure the laser safety. This is primarily used for personal protection. Furthermore, the interlock should be designed to safely intercept failures. In case of a loss of optical laser power, it should shut down the system to a safe state without an irreversible damage. It prevents expensive repair costs and minimizes the downtime of such systems. This point is particularly an important aspect

for a 24/7-application as GWDs.

For fiber amplifiers in MOPA configuration, there are different events which can lead to various failures. One of the most critical case is the loss of the seed signal and the corresponding onset of parasitic lasing or Q-switching effects. Therefore, this case is examined in more detail below and an interlock system is presented which enables a safe shutdown of the laser. An important aspect is the time scale, in which such processes lead to the parasitic lasing or Q-switching effects. The finite fluorescence lifetime of the $^2F_{5/2}$ laser-level of Yb^{3+} is in the range of 0.8 ms [Pas97b]. Hence, a suitable interlock system should be faster than this lifetime.

The basic idea behind the concept of the following interlock system is the fast shutdown due to an electrical short circuit of the pump laser diode. This is implemented via a MOSFET (metal-oxide-semiconductor field-effect transistor), which is switched by a corresponding control signal. A MOSFET driver delivers the required electrical power for a fast switching process. The electrical layout is presented in the Appendix B.2. The control signal is provided in the following by an external trigger signal and in the final experiment by the voltage of a photodiode. An integrated hysteresis prevents permanent oscillations around the shutdown threshold.

For fiber amplifier systems, high-power pump laser diodes with an optical power over 100 W are typically used. Therefore, the interlock system was tested with such a laser diode with 150 W output power (K976FN1RN-150.0W, BWT). The optical output signal of the diode was detected by a photodiode, whose evolution of the photodiode voltage is shown in Fig. 6.19. After an external trigger event (see black curve in Fig. 6.19), the gate of the MOSFET is switched and the laser diode is shorted. At all different pump currents, the optical signal on the photodiode drops to zero within a microsecond. Thus, the measured decrease in the optical signal is significantly below the fluorescence lifetime of the $^2F_{5/2}$ laser-level. For this reason, the interlock system was tested on an existing fiber amplifier with an output power of 15 W and the shutdown behavior of the system was investigated.

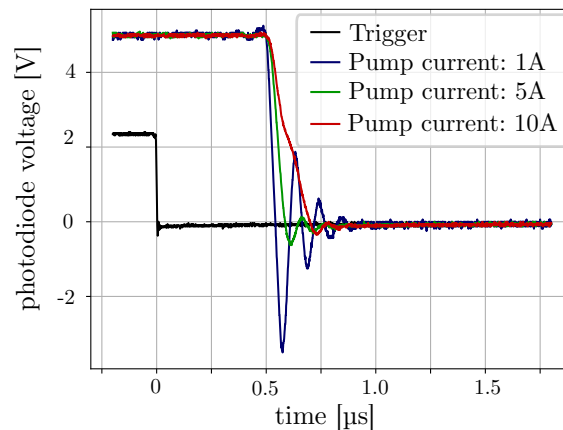


Figure 6.19: Evolution of the photodiode voltage detecting the optical output power of a fiber-coupled high-power pump diode. After a trigger event, the interlock system shut down the optical power within a 1 μ s.

The setup of the used fiber amplifier design is the same as the pre-amplifier of Chapter 6.1.1. The design is further on illustrated in Fig. 6.7. The trigger signal for the controlled shutdown was given by a photodiode before the actual fiber amplifier stage. For this purpose, a small part of the NPRO signal was focused on the photodiode. The temporal evolution of the induced voltage is depicted in Fig. 6.20a). The event of the shutdown was triggered by a mechanical shutter by blocking the NPRO signal and is therefore in the range of a few milliseconds. The curve in blue shows the photodiode voltage with an activated interlock system. In Fig. 6.20b), the voltage of a second photodiode behind the amplifier stage is presented. With an activated interlock system, the optical system could be shutdown in a controlled way. This result could be reproduced in several tests. The entire laser system was then completely functional at all times without any kind of degradation.

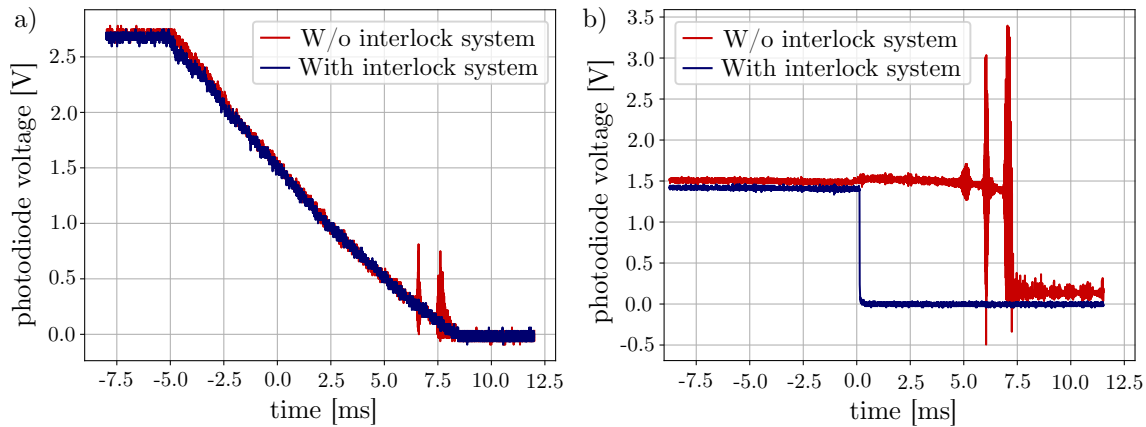


Figure 6.20: Evolution of the photodiode voltage detecting the optical output power in a) in front of and in b) behind a fiber amplifier system. Both plots illustrate the behavior of the amplifier with an activated and without an interlock system. With an deactivated interlock, the laser was damaged irreversible due to parasitic lasing effects.

If the interlock system is deactivated, the fiber amplifier behaves completely differently after the shutdown event. In Fig. 6.20, this is illustrated by the red curves. At 12.5 ms after the event, parasitic oscillations are recognizable on the output signal of the photodiode. The third and largest oscillation was simultaneous with burning off the fiber end facet and the irreversible damage of the laser system. These measurements confirm the initial assumption that the parasitic effects are on a time scale of a few ms. Because the design of the interlock can perform a controlled shutdown within a microsecond as shown, this system is suitable for a use in fiber amplifiers or other laser systems.

Finally, the conceptual design was transferred to a circuit board including the key components of a MOSFET and a corresponding driver. An image of the circuit board is illustrated in Fig. 6.21 (and in the Appendix B.1). The required electrical components are listed in Table B.1 in the appendix. With final dimensions of $(7 \times 4) \text{ cm}^2$, the board can be easily integrated in existing control systems. For this purpose, only an external power supply ($\pm 15 \text{ V}$) and a photodiode signal as a trigger are required. A reference voltage as a threshold for the shutdown process can also be specified externally. In Fig. 6.21b), the

integration on a top-hat rail to an existing automation laser control system by *Beckhoff* is visualized.

The interlock system was also successfully tested in a high-power fiber amplifier operating at a wavelength of 1.5 μm . This long-term test over several days confirmed the reliability of the circuit board even in long-term operation.

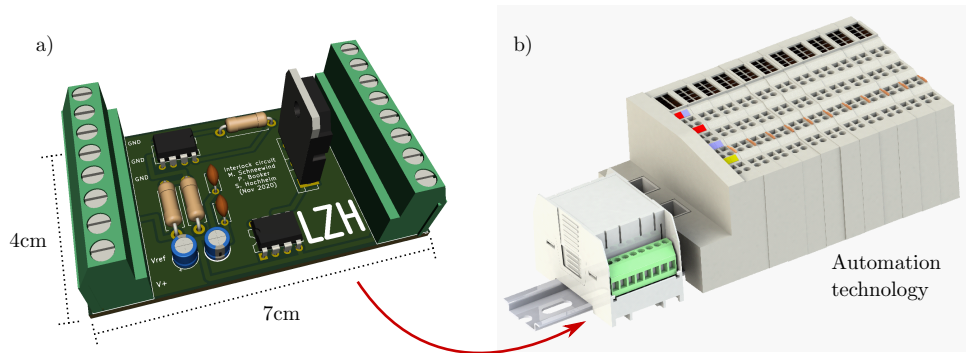


Figure 6.21: Image of the circuit board of the interlock system in a) and illustration of the implementation to an existing automation laser control system by *Beckhoff*.

6.5 Conclusion

The further power scaling of stable and reliable laser sources for the next generation of GWDs is an important aspect and the main part of this chapter. The realization of an output power level of several hundreds of watts operating at 1064 nm above the limitations of standard fiber amplifiers or other laser designs requires new technologies and optical components.

Therefore, this chapter presented the use of 3C[®]-fibers in all-fiber amplifier systems based on the results from Chapter 4 and 5. This resulted in two laser systems with optical output power of 170 W and above 300 W. Both designs are initially designed to validate the functional feasibility and the optical parameters of such amplifier architectures in an all-fiber configuration. For the first time, all optical components of the amplifier system were directly integrated in a single 3C[®]-fiber to achieve a spliceless design and a high spatial purity. Finally, at an output power of 336 W, a fundamental mode content of 90.4% at a PER above 13 dB was demonstrated. For the realization of such parameters, the amplifier architecture was designed with two amplifier stages. The pre-amplifier was based on a standard SM fiber and typical optical components with an output power of 15 W. The interface to the main-amplifier was realized by an advanced 3C[®]-fiber isolator with an integrated MFA. The entire optical device was optimized including thermal lens effects, so that minimum optical losses were achieved.

Besides for the first time, the key component of a signal and pump combiner directly integrated in the active 3C[®]-fiber was used. This device enabled the pumping with an optical power of 600 W into the active fiber. Afterwards, the pump power limited amplifier system operated stable over several hours and showed no onset of degradation. At the maximum output power level of 336 W no impact of TMI or other parasitic effects was

determined. However, with a first slight intensity noise increase in the 5 MHz range, the first onset of SBS might be indicated.

This world's first prototype of an all-fiber design with optical components integrated directly in the active 3C[®]-fiber successfully demonstrated optical specification capabilities using such amplifier architectures. With respect to the excellent beam quality at these output power levels, this work emphasizes the high potential of fiber amplifiers based on 3C[®]-fibers as laser sources for the next generation of GWDs.

The developments of the monolithic 3C[®]-fiber amplifier designs and the corresponding optical components can be significantly improved by using 3C[®]-fibers with larger cores. These and other optimization technologies are discussed in the next Chapter 7.

CHAPTER 7

Summary and Outlook

Future detector generations of earth-based gravitational wave detectors such as the European project "Einstein Telescope" require a laser with an optical power level of more than several of hundreds watts in the TEM₀₀ mode for improving their sensitivities. The challenging parameters of such a laser system with a linearly-polarized SF signal at 1064 nm can not be fulfilled by current amplifier designs. A promising approach to overcome current limitations are fiber amplifiers with conventional large mode area fibers. Laboratory and afterwards engineering prototypes were operated successfully at power levels of 200 W over thousands of hours. Finally, SF amplifier architectures employing these fiber types were limited in their output power levels by the nonlinear effect of stimulated Brillouin scattering.

Due to the limiting properties of SBS for fiber laser or amplifier systems, the knowledge of the excess intensity noise above the SBS threshold conduces to the comprehension of noise properties of such laser systems and can be useful for further laser stabilization methods. Therefore, this work focused on the impact of the excess broadband intensity noise by the conversion from phase to intensity noise. Using a heterodyne measurement technique, an asymmetric gain spectrum was experimentally observed and a modified Lorentzian equation was used to describe the measured profile. Based on these results and the parameter of the mathematical fit, the total phase shift of one round trip in the single-mode fiber system was calculated to explain the observed eigenfrequencies in the intensity noise spectrum. Only through the addition of a phase shift term caused by SBS, the resonator eigenfrequencies can be mathematically described correctly. For the verification, the experiments were repeated with different fiber lengths in the setup. Besides, a splitting of the resonator peaks in the intensity noise spectrum was observed and also explained by the additional phase shift due to an asymmetric Lorentzian profile. This theoretical model was verified by experimental investigations of intensity noise spectra at different power levels above the SBS threshold. These new and consistent results suggest the conversion from phase to intensity noise and confirm the parameter of the fitted and modified Lorentzian profile. In the scientific context, the presented measurements continue the idea of Peral and Zhang [Per99; Zha05] and open up a new perspective on the impact of the Brillouin gain spectrum to the nonlinear effect of SBS. For the first time, the shape of the excess intensity noise was reconstructed based on the parameter of the asymmetric Brillouin gain spectrum. At different power levels above the SBS threshold, the gain spectra were measured and the fitted profile was used to describe the characteristic shape of the intensity noise. The investigations and understanding of this nonlinear effect have a large impact for optimizing

future laser or amplifier systems based on fiber architectures and the increase of the SBS threshold.

Over the last decade, several fibers have been developed to overcome these limitations and avoid the onset of SBS. Especially, the photonic crystal fiber (PCF) has found its way into commercial use by the large variety of applications. However, due to the micro-structured pattern with an arrangement of air holes inside of PCFs, these fiber types are only partially suitable for the construction of fiber-based components and therefore monolithic fiber amplifiers. Here, specialty fiber geometries based on an all-solid design exhibit a significant advantage for the assembly of such optical components. A promising fiber concept in this context with an enlarged mode field diameter to reduce the impact of nonlinearities is the so called chirally-coupled core (3C[®]) fiber. Due to additional side cores around the actual signal core and the corresponding mode interaction by an optical angular momentum, the 3C[®]-fiber performs as an effectively single-mode fiber. Several laser systems were already designed and successfully tested with this fiber type. A temporal overview of the different achieved output power levels of such 3C[®]-fibers amplifier systems is illustrated in Fig. 7.1.

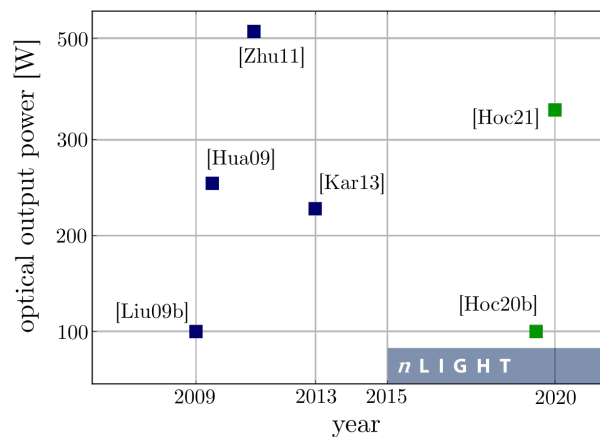


Figure 7.1: Historical overview of the output power levels achieved with 3C[®]-fibers amplifier systems. The results of this work (green squares) are taken into the scientific context with previous systems (blue squares). For the first time, the presented architectures are all-fiber amplifier designs. Since 2015, nLight has been distributing the 3C[®]-fibers.

In 2009, Liu and the group of Galvanauskas presented a 10 ns-pulsed amplifier design at average powers of 100 W exceeding pulse energies of 1 mJ. In the same year, the group demonstrated the first power scaling experiments up to power levels of 250 W. The first approach of power scaling of SF signal wavelengths at 1064 nm with this fiber was performed by Zhu et al. and Karow et al. at the LZH in 2013. Here, a total amplifier output of 230 W with a fundamental mode content of 95% and a maximum output power of 511 W was achieved. However, all these amplifier systems were operated in a free-space pumping configuration. For the reduction of the system complexity and the long-term reliability, this work presented for the first time all-fiber amplifier designs using 3C[®]-fibers. In 2019, a monolithic 3C[®]-fiber amplifier architecture addressing the power requirements of laser sources in GWDs with an integrated mode-field adapter (MFA) was developed. At an

output power level of 100 W operating at 1064 nm, a TEM_{00} mode content of 98.9% was measured. This fundamental mode content is the highest value for an output power level of around 100 W. Additionally, the system exhibited a stable operation for several days with no onset of SBS or other parasitic effects. This world's first prototype was designed to validate the functional feasibility and the optical parameter of such all-fiber amplifier architectures. Based on these experimental results and the limitations of this amplifier architecture, the design was revised and further optical components were integrated in the 3C[®]-fiber. Since the entire pump light was not propagating through the MFA, further power scaling was feasible by using a highly-integrated 3C[®]-fiber signal and pump combiner. Such optical key components were developed, manufactured and characterized afterwards. In this context, an all-fiber characterization concept of an S^2 -imaging technique was presented. This concept enabled the ability to measure the mode content in real time, so that, for example, the quality of optical components can be controlled during the manufacturing process.

Finally, a mode field adapter, an end cap, a cladding light stripper and a pump combiner were directly integrated for the first time in an Yb^{3+} -doped fiber for the implementation in a high-power amplifier system. Such a spliceless fiber amplifier architecture guaranteed to maintain the optical signal specifications of the seed signal. The system was designed in MOPA configuration with two amplifier stages. At an output power level of 336 W, a fundamental mode content of 90.4% at a PER above 13 dB was demonstrated. Pump power-limited at an optical power of 600 W at 976 nm, the amplifier showed no impact of TMI or other parasitic effects. A first slight increase of the intensity noise in the 5 MHz range might indicate the onset of SBS. With respect to the excellent beam quality at the achieved output power levels, this work emphasizes the high potential of fiber amplifiers based on 3C[®]-fibers as laser sources for the next generation of GWDs and opened up a variety of new research questions.

In the scientific context, this work presented new all-fiber amplifier concepts above current state of the art technology. However, improvements integrated in the current systems can realize further power scaling of these high-power amplifiers. A critical component of the presented architecture was the signal and pump combiner with an coupling efficiency of $\sim 78\%$, which is significantly below the efficiencies ($>90\%$) of PC with standard fibers. An optimization of the manufacturing process and the corresponding parameters could optimize this coupling efficiency and the total amplifier output power. Additional modifications of the cladding structure of the 3C[®]-fiber by a CO_2 laser could be a useful tool to increase these efficiencies. If coupling efficiencies above 90% will be achieved with this fiber type, an optical power level of more than 350 W could be realized. However, such a power level is still below the requirements of the 'Einstein Telescope' design study. One suitable approach to fulfill these specifications is the coherent beam combination of two of such 3C[®]-fiber amplifier systems. Combining two SF 200 W amplifiers based on standard LMA fibers was already successfully demonstrated [Wel21].

The polarization properties of the presented design decrease with increasing power levels. Further investigations have shown that this can be optimized by winding the fiber without excess mechanical torsion. A potential engineering prototype could integrate such a manufacturing step for an improved polarization extinction ratio.

Further power scaling of SF signals can be achieved by increasing the mode field diameter even further above the $34\ \mu\text{m}$. In this context, 3C[®]-fibers with core diameter of $55\ \mu\text{m}$ and $85\ \mu\text{m}$ are under development by nLight. Increasing the core diameter to $55\ \mu\text{m}$ corresponds to an increase in the core area by a factor of around 2.5. Accordingly, the onset of nonlinear-effects is suppressed and higher amplifier output power levels can be realized. In addition to SBS, other effects such as TMI become more and more relevant at further power scaling and have to be taken into account in the amplifier design and characterization. If these effects can be successfully suppressed in following systems, the required performance levels of ET can also be achieved by a single amplifier system. This in turn minimizes the complexity of such a laser system.

The development of the 3C[®]-fibers opened up new possibilities for power scaling of SF signals, which can fulfill the special requirements of the next generation of GWDs. This work demonstrated that new all-fiber designs allows amplifier power levels above the state of the art technology in compact laser systems.

Bibliography

- [ISO11146] 11146, ISO STANDARD: *Lasers and laser-related equipment – Test methods for laser beam widths, divergence angles and beam propagation ratios*. 2005 (cit. on p. 36).
- [Aba12] ABADIE, J. and et AL: *Search for gravitational waves from low mass binary coalescence in LIGO’s sixth science rund and Virgo’s science runs 2 and 3*. Physical Review D **85**(8), 0820021-08200212, 2012 (cit. on p. 2).
- [Abb17] ABBOTT, B. and et AL: *Multi-messenger Observations of a Binary Neutron Star Merger*. The Astrophysical Journal **848**(2), L12, 2017 (cit. on p. 2).
- [Abb16] ABBOTT, B. and et AL: *Oberservation of gravitational waves from a binary black hole merger*. Physical Review Letters **116**(6), 2016 (cit. on pp. 1, 2).
- [Abe11] ABERNATHY, M., et AL., and (THE ET SCIENCE TEAM): *The Einstein gravitational wave telescope conceptual design study (No.4)*. ET-0106C-10, 2011 (cit. on pp. 3, 69, 83, 84).
- [Ada01] ADAM, J.-L.: *Fluoride glass research in France: Fundamentals and applications*. J. Fluor. Chem. **107**(2), 265 – 270, 2001 (cit. on p. 8).
- [Adh06] ADHIKARI, R., P. FRITSCHER, and S. WALDMAN: *Enhanced LIGO*. Technical Report LIGO-T060156, LIGO Laboratory Pasadena, CA, USA, 2006 (cit. on p. 2).
- [Agr01] AGRAWAL, G. P.: *Nonlinear Fiber Optics*. 3rd ed. Academic Press Inc., 2001 (cit. on pp. 8, 12, 13, 15–18, 26–28).
- [Agr20] AGRAWAL, L. and D. GANOTRA: *Suppression of parasitic lasing and inter-pulse self-pulsing in a pulsed Erbium–Ytterbium co-doped fiber amplifier*. Appl. Phys. B **126**, 14, 2020 (cit. on p. 12).
- [All03] ALLEN, L., S. M. BARNETT, and M. J. PADGETT: *Optical Angular Momentum*. I.O.P., London, UK, 2003 (cit. on p. 19).
- [All92] ALLEN, L., M. W. BEIJERSBERGEN, R. J. C. SPREEUW, and J. P. WOERDMAN: *Orbital angular momentum of light and the transformation of Laguerre-Gaussian laser modes*. Physical Review A **45**(11), pp. 8185-8190, 1992 (cit. on pp. 20, 21).
- [Bar99] BARNES, N. P. and B. M. WALSH: *Amplified spontaneous emission - Application to Nd:YAG lasers*. IEEE Journal of Quantum Electronics **35**(1), 101-109, 1999 (cit. on p. 12).

- [Bar91] BARNES, W. L. and et AL.: *Absorption and emission cross section of Er^{3+} doped silica fibers*. IEEE J. Quantum Electron. 27 (4), 1004, 1991 (cit. on p. 10).
- [Bas95] BASISTIY, I.V., M.S. SOSKIN, and M.V. VASNETSOV: *Optical wavefront dislocations and their properties*. Optics Communications 119(5), pp. 604-612, 1995 (cit. on p. 21).
- [Bay90] BAYVEL, P. and P.M. RADMORE: *Solutions of the SBS equations in single mode optical fibres and implications for fibre transmission systems*. Electron. Lett. 26(7), 434-436, 1990 (cit. on p. 65).
- [Baz90] BAZHENOV, V.Y., M.V. VASNETSOV, and M.S. SOSKIN: *Laser beams with screw dislocation in their wavefronts*. JETP Letters 52(8), pp. 429-431, 1990 (cit. on p. 21).
- [Bet36] BETH, R. A.: *Mechanical detection and measurement of the angular momentum of light*. Physical Review Letters 50(2), pp. 115-125, 1936 (cit. on p. 20).
- [Bill99] BILLINGTON, R.: *NPL Report COEM 31*. (accessed August 10, 2020). URL: <http://eprintspublications.npl.co.uk/> (cit. on p. 18).
- [Bir95] BIRKS, T. A. and et AL.: *Full 2-d photonic bandgaps in silica/air structures*. Electron. Lett. 31, 1941, 1995 (cit. on p. 18).
- [Bla11] BLAZEK, M. and et AL.: *Unifying intensity noise and second-order coherence properties of amplified spontaneous emission sources*. Opt. Lett. 36 (17), 3455, 2011 (cit. on p. 12).
- [Bod20a] BODE, N., J. BRIGGS, X. CHEN, M. FREDE, P. FRITSCHEL, M. FYFFE, E. GUSTAFSON, M. HEINTZE, P. KING, J. LIU, J. OBERLING, R.L. SAVAGE, A. SPENCER, and B. WILLKE: *Advanced LIGO Laser Systems for O3 and Future Observation Runs*. Galaxies 8(84), 2020 (cit. on p. 2).
- [Bod20b] BODE, N., F. MEYLAHN, and B. WILLKE: *Sequential high power laser amplifiers for gravitational wave detection*. Opt. Exp. 28(2), 29469-29478, 2020 (cit. on p. 2).
- [Boy03] BOYD, R. W.: *Nonlinear Optics*. Academic Press Inc., Second Edition, 2003 (cit. on pp. 14, 15).
- [Bri22] BRILLOUIN, L.: *Diffusion de la Lumière et des Rayonnes X par un Corps Transparent Homogène; Influence del'Agitation Thermique*. Annales des Physique 17, 88, 1922 (cit. on p. 15).
- [Bro02] BROMAGE, J. and et AL.: *A method to predict the Raman gain spectra of germanosilicate fibers with arbitrary index profiles*. IEEE Photon. Technol. Lett. 14 (1), 24, 2002 (cit. on p. 16).
- [Buc04] BUCK, J. A.: *Fundamentals of Optical Fibers*. 2nd ed. Wiley - Interscience, 2004 (cit. on pp. 8, 9, 13, 14).

-
- [Bui19] BUIKEMA, A., F. JOSE, S.J. AUGST, P. FRITSCHER, and N. MAVALVALA: *Pump-gain integrated functional laser fiber towards 10 kW-level high-power applications*. Opt. Lett. **44**(15), 3833-3836, 2019 (cit. on p. 3).
- [Cha04] CHANG, G., A. GALVANAUSKAS, H. G. WINFUL, and T. B. NORRIS: *Dependence of parabolic pulse amplification on stimulated Raman scattering and gain bandwidth*. Opt. Lett. **29**, 2647-2649, 2004 (cit. on p. 16).
- [Che10] CHEN, H.-W., T. SOSNOWSKI, C.-H. LIU, L.-J. CHEN, J. R. BIRGE, A. GALVANAUSKAS, F. X. KÄRTNER, and G. CHANG: *Chirally-coupled-core Yb-fiber laser delivering 80-fs pulses with diffraction-limited beam quality warranted by a high-dispersion mirror based compressor*. Opt. Exp. **18**, 24699-24705, 2010 (cit. on p. 24).
- [Che06] CHENG, M.-Y., K.-C. HOU, A. GALVANAUSKAS, D. ENGIN, R. CHANGKAKOTI, and P. MAMIDIPUDI: *High average power generation of single-transverse mode MW-peak power pulses using 80 μ m core Yb-doped LMA fibers*. Conference on Lasers, Electro-Optics/Quantum Electronics, and Laser Science Conference (CLEO/QELS), Optical Society of America, 2006 (cit. on p. 18).
- [Chi64] CHIAO, R. Y., C.H. TOWNES, and B. P. STOICHEFF: *Stimulated Brillouin Scattering and Coherent Generation of Intense Hypersonic Waves*. Phys. Rev. Lett. **12**, 592, 1964 (cit. on p. 15).
- [Col18] COLUCELLI, N., E. VICENTINI, A. GAMBETTA, C. R. HOWLE, K. MCEWAN, P. LAPORTA, and G. GALZERANO: *Broadband Fourier-transform coherent Raman spectroscopy with an ytterbium fiber laser*. Opt. Express **26**, 18855-18862, 2018 (cit. on p. 11).
- [Cre99] CREGAN, R. F. and et AL.: *Single-mode photonic band gap guidance of light in air*. Science **285**, 1537, 1999 (cit. on p. 18).
- [NPRO] *Datasheet of Innolight Mephisto 2000NE*. (accessed August 10, 2020). URL: https://edge.coherent.com/assets/pdf/COHR_Mephisto_DS_0417_2.pdf (cit. on p. 32).
- [Dej99] DEJNEKA, M. and B. SAMSON: *Rare-Earth-Doped Fibers for Telecommunications Applications*. MRS Bulletin, **24**(9), 39-45, 1999 (cit. on p. 10).
- [DiG99] DIGIOVANNI, D. J. and A. J. STENTZ: *Tapered fiber bundles for coupling light into and out of cladding-pumped fiber devices*. U.S. Patent 5864644, 1999 (cit. on p. 52).
- [Dig01] DIGONNET, M.: *Rare-Earth-Doped Fiber Lasers and Amplifiers*. Inc. New York EUA, 172-184, 2001 (cit. on p. 10).
- [Dil20] *Dilas GmbH*. (accessed August 10, 2020). URL: <http://www.dilas.com/products/search/horizontal-stacked> (cit. on p. 9).

- [Dix20] DIXNEUF, C., G. GUIRAUD, Y. BARDIN, Q. ROSA, M. GOEPPNER, A. HILICO, C. PIERRE, J. BOULLET, N. TRAYNOR, and G. SANTARELLI: *Ultra-low intensity noise, all fiber 365 W linearly polarized single frequency laser at 1064 nm*. Opt. Exp. **82**, 10960-10969, 2020 (cit. on p. 3).
- [Ein16] EINSTEIN, A.: *Die Grundlage der allgemeinen Relativitätstheorie*. Annalen der Physik **354**(7), 769–822, 1916 (cit. on p. 1).
- [Eng14] ENGELBRECHT, R.: *Nichtlineare Faseroptik*. Springer Vieweg, Berlin, Heidelberg, 2014 (cit. on pp. 18, 65).
- [Fer98] FERMAN, M. E.: *Single-mode excitation of multimode fibers with ultrashort pulses*. Opt. Lett. **23**, pp. 52-54, 1998 (cit. on p. 18).
- [Fil90] FILIPPOV, V. N. and et AL.: *Measurement of polarisation beat length in single-mode optical fibres with a polarisation modulator*. Electron. Lett. **26** (10), 658, 1990 (cit. on p. 9).
- [Fre07] FREDE, M., B. SCHULZ, R. WILHELM, P. KWEE, F. SEIFERT, B. WILLKE, and D. KRACHT: *Fundamental mode, single-frequency laser amplifier for gravitational wave detectors*. Opt. Exp. **15**(2), 459, 2007 (cit. on p. 2).
- [Fri12] FRICKE, T.T., N.D. SMITH-LEFEBVRE, R. ABBOTT, K.L. DOOLEY, M. EVANS, P. FRITSCHER, V.V. FROLOV, K. KAWABE, J.S. KISSEL, and et AL.: *DC readout experiment in Enhanced LIGO*. Class. Quantum Gravity **29**, 065005, 2012 (cit. on p. 3).
- [Gar64] GARMIRE, E. and C. H. TOWNES: *Stimulated Brillouin scattering in liquids*. Appl. Phys. Lett. **5**, 84, 1964 (cit. on p. 15).
- [Glo71a] GLOGE, D.: *Weakly guiding fibers*. Applied Optics **10**(10), 2252 – 3358, 1971 (cit. on p. 8).
- [Glo71b] GLOGE, D.: *Weakly guiding fibers*. Applied Optics **10**(10), 2252-2258, 1971 (cit. on p. 13).
- [Gra16] GRAY, D. R., M. N. PETROVICH, S. R. SANDOGHCHI, N. V. WHEELER, N. K. BADDELA, G. T. JASON, T. BRADLEY, D. J. RICHARDSON, and F. POLETTI: *Real-Time Modal Analysis via Wavelength-Swept Spatial and Spectral (S^2) Imaging*. IEEE Photonics Technology Letters, vol. 28, no. 9, pp. 1034-1037, 2016 (cit. on p. 39).
- [Gro18] GROTE, H.: *Gravitationswellen - Geschichte einer Jahrhundertentdeckung*. Verlag C.H. Beck oHG, München, 2018 (cit. on pp. 1–3).
- [Gup20] GUPTA G.P. Sil N., DEY S.K. and et AL.: *Modal propagation characteristics of mono-mode polarization maintaining optical fiber with off centered core*. Indian J Phys, 2020 (cit. on p. 10).
- [Han88] HANNA, D. C. and et AL.: *Continuous-wave oscillation of a monomode ytterbium-doped fiber laser*. Electron. Lett. **24**, 1111, 1988 (cit. on p. 10).

-
- [Hea05] HEADLEY, C., M. FISHTEYN, A. D. YABLON, M. J. ANDREJCO, K. BRAR, J. MANN, M. D. MERMELSTEIN, and D. J. DIGIOVANNI: *Tapered fiber bundles for combining laser pumps (Invited Paper)*. Proc. SPIE **5709**, 263–272, 2005 (cit. on p. 52).
- [Hem14] HEMMING, A. and et AL.: *A review of recent progress in holmium-doped silica fibre sources*. Opt. Fiber Technol. 20 (6), 621, 2014 (cit. on p. 10).
- [Hil09] HILD, S., S. CHELKOWSKI, A. FREISE, J. FRANC, N. MORGADO, R. FLAMINIO, and R. DESALVO: *A xylophone configuration for third generation gravitational wave detector*. Classical and Quantum Gravity 27(1), 0150031-0150038, 2009 (cit. on pp. 2, 69).
- [Hil08] HILDEBRANDT, M., S. BÜSCHE, P. WESSELS, M. FREDE, and D. KRACHT: *Brillouin scattering spectra in high-power single-frequency ytterbium doped fiber amplifiers*. Opt. Exp. 16 (20), 15970, 2008 (cit. on pp. 16, 18, 65, 66, 76, 86).
- [Hoc21] HOCHHEIM, S., E. BROCKMÜLLER, P. WESSELS, M. STEINKE, J. KOPONEN, T. LOWDER, S. NOVOTNY, J. NEUMANN, and D. KRACHT: *Highly-integrated signal and pump combiner in chirally-coupled-core fibers for all-fiber lasers and amplifiers*. in Journal of Lightwave Technology, doi: 10.1109/JLT.2021.3111993, 2021 (cit. on p. 36).
- [Hoc20a] HOCHHEIM, S., J. NEUMANN, D. KRACHT, and M. STEINKE: *Broadband excess intensity noise due to an asymmetric Brillouin gain spectrum in optical fibers*. OSA Continuum 3, 2902-2911, 2020 (cit. on p. 25).
- [Hoc20b] HOCHHEIM, S., M. STEINKE, P. WESSELS, O. de VARONA, J. KOPONEN, T. LOWDER, S. NOVOTNY, J. NEUMANN, and D. KRACHT: *Single-frequency chirally-coupled-core all-fiber amplifier with 100 W in a linearly-polarized TEM₀₀-mode*. Opt. Lett. 45, 939-942, 2020 (cit. on p. 59).
- [Hor97] HOROWITZ, M., A. R. CHRAPLYVY, R. W. TKACH, and J. L. ZYSKIND: *Broad-Band Transmitted Intensity Noise Induced by Stokes and Anti-Stokes Brillouin in Single-Mode Fibers*. IEEE Phot. Technol. Lett. **9**(1), 124–126, 1997 (cit. on pp. 25, 86).
- [Hua09] HUANG, S., C. ZHU, C.-H. LIU, X. MA, C. SWAN, and A. GALVANAUSKAS: *Power scaling of CCC fiber based lasers*. in Conference on Lasers and Electro-Optics/International Quantum Electronics Conference, 2009 (cit. on p. 23).
- [FMA] *Interfiber Analysis, FMA-100*. (accessed August 10, 2020). URL: <http://www.interfiberanalysis.com/products.html> (cit. on p. 39).
- [Ipp72] IPPEN, E. P. and R. H. STOLEN: *Stimulated Brillouin scattering in optical fibers*. Appl. Phys. Lett. 21, 539, 1972 (cit. on p. 15).
- [Iza87] IZAWA, T. and S. SUDO: *Advances in Optoelectronics, in Optical Fibers: Materials and Fabrication*. T. Okoshi, 1987 (cit. on p. 8).

- [Izu17] IZUMI, K. and D. SIGG: *Advanced LIGO: Length Sensing and Control in a Dual Recycled Interferometric Gravitational Wave Antenna*. Classical Quantum Gravity **34**(1), 015001, 2017 (cit. on p. 86).
- [Jau15] JAUREGUI, C., H.-J. OTTO, F. STUTZKI, J. LIMPERT, and A. TÜNNERMANN: *Simplified modelling the mode instability threshold of high power fiber amplifiers in the presence of photodarkening*. Opt. Exp. **23**(16), 20203, 2015 (cit. on p. 85).
- [Jav16] JAVADIMANESH M., GHAVAMI SABOURI S. and KHORSANDI A.: *The effect of cladding geometry on the absorption efficiency of double-clad fiber lasers*. Optica Applicata, Vol. XLVI, No. 2, 2016 (cit. on p. 10).
- [Jeo05] JEONG, Y., J.K. SAHU, D.B.S. SOH, C. A. CODEMARD, and J. NILSSON: *High power tunable single-frequency single-mode Erbium:Ytterbium codoped large core fiber master-oscillator power amplifier source*. Opt. Lett. **30** (22), pp. 2997–2999, 2005 (cit. on p. 61).
- [Jeo07] JEONG, Y., S. YOO, C. CODEMARD, J. NILSSON, J. SAHU, D. PAYNE, R. HORLEY, P. TURNER, L. HICKEY, A. HARKER, M. LOVELADY, and A. PIPER: *Erbium:Ytterbium codoped large-core fiber laser with 297-W continuous-wave output power*. IEEE J. Sel. Top. Quantum Electron. **13** (3), pp. 573–579, 2007 (cit. on p. 61).
- [Joh13] JOHANSEN, M. M., K. R. HANSEN, M. LAURILA, T. TANGGAARD ALKESKJOLD, and J. LÆGSGAARD: *Estimating modal instability threshold for photonic crystal rod fiber amplifiers*. Opt. Exp. **21**, 15409-15417, 2013 (cit. on pp. 85, 86).
- [Kab19] KABACINSKI, P. and et AL.: *Nonlinear refractive index measurement by SPM-induced phase regression*. Opt. Express **27** (8), 11018, 2019 (cit. on p. 15).
- [Kai09] KAISER, T., D. FLAMM, S. SCHRÖTER, and M. DUPARRE: *Complete modal decomposition for optical fibers using CGH-based correlation filters*. Optics Exp. **17**(11), 9347-9356, 2009 (cit. on p. 63).
- [Kam81] KAMINOW, I.P.: *Polarization in optical fibers*. IEEE Journal of Quantum Electronics **17**(1), pp. 15-22, 1981 (cit. on p. 9).
- [Kap20] KAPASI, D.P., J. EICHHOLZ, T. MCRAE, R.L. WARD, B.J.J. SLAGMOLEN, S. LEGGE, K.S. HARDMAN, P.A. ALTIN, and D.E. MCCLELLAND: *Tunable narrow-linewidth laser at 2 μ m wavelength for gravitational wave detector research*. Opt. Exp. **28**, 3280-3288, 2020 (cit. on p. 3).
- [Kar13] KAROW, M.: *TEM₀₀ mode power scaling in specialty fibers*. Thesis: PhD Leibniz U., Hannover, 2013 (cit. on pp. 20, 24, 59, 64, 86).
- [Kle81] KLEPPNER, D.: *Inhibited spontaneous emission*. Physical Review Letters **47**(4), 233-236, 1981 (cit. on p. 12).

-
- [Kni17] KNIGGE, A., C. KNOTHE, U. OECHSNER, and G. FEDERAU: *Fibers with End Caps - While maintaining polarization, the application is extended to higher powers and photocontamination effects are avoided*. Wiley-VCH Verlag GmbH and Co. KGaA, Weinheim, 2017 (cit. on p. 48).
- [Kni03] KNIGHT, J. C.: *Photonic crystal fibres*. Nature 424, 847, 2003 (cit. on pp. 18, 45).
- [Koc15] KOCHANOWICZ, M., J. ZMOJDA, P. MILUSKI, J. PISARSKA, W. A. PISARSKI, and D. DOROSZ: *NIR to visible upconversion in double – clad optical fiber co-doped with Yb^{3+}/Ho^{3+}* . Opt. Mater. Express 5, 1505-1510, 2015 (cit. on p. 11).
- [Kon97] KONKANEN, S. and et AL.: *High Er concentration phosphate glasses for planar waveguide amplifiers*. Proc. SPIE 2996, 32, 1997 (cit. on p. 10).
- [Kop00] KOPLOW, J. P., D. A. V. KLINER, and L. GOLDBERG: *Single-mode operation of a coiled multimode fiber amplifier*. Optics Lett. 25(7), pp. 442-442, 2000 (cit. on pp. 4, 18).
- [Kou02] KOUZNETSOV, D. and MOLONEY J.V.: *Efficiency of pump absorption in double-clad fiber amplifiers. II. Broken circular symmetry*. J. Opt. Soc. Am. B 19 (6), 1259, 2002 (cit. on p. 10).
- [Kou03] KOUZNETSOV, D. and MOLONEY J.V.: *Efficiency of pump absorption in double-clad fiber amplifiers. III: Calculation of modes*. J. Opt. Soc. Am. B 19 (6), 1304, 2003 (cit. on p. 10).
- [Kov99] KOVALEV, V. I. and R. G. HARRISON: *Diffraction limited output from a CW ND:YAG maser-oscillator/ power amplifier with fibre phase conjugate SBS mirror*. Optics Communications 166(1), 89-93, 1999 (cit. on p. 12).
- [Kum84] KUMAR, A. and et AL.: *Birefringence calculations in elliptical-core optical fibers*. Electron. Lett. 20, 112, 1984 (cit. on p. 9).
- [Kwe12] KWEE, P., C. BOGAN, K. DANZMANN, M. FREDE, H. KIM, P. KING, J. PÖLD, O. PUNCKEN, R. L. SAVAGE, F. SEIFERT, P. WESSELS, L. WINKELMANN, and B. WILLKE: *Stabilized high-power laser system for the gravitational wave detector advanced LIGO*. Opt. Exp. 20, 10617-10634, 2012 (cit. on p. 85).
- [Kwe07] KWEE, P., F. SEIFERT, B. WILLKE, and K. DANZMANN: *Laser beam quality and pointing measurement with an optical resonator*. Review of Scientific Instruments 78 (7), p. 073103, 2007 (cit. on pp. 63, 82).
- [Kyo93] KYOTO M. Ohoga Y., ISHIKAWA S. and ISHIGURO Y.: *Characterisation of fluorine-doped silica glasses*. Journal of Materials Science 28(10), 2738-2744, 1993 (cit. on p. 8).
- [Las20a] Laserline GmbH. (accessed August 10, 2020). URL: <https://www.laserline.com/en-int/ldm-serie/> (cit. on p. 9).
- [Las20b] Laserline GmbH. (accessed August 10, 2020). URL: <https://www.laserline.com/de-int/ldf-serie/> (cit. on p. 10).

- [Lee13] LEE, Y.-W., H.-W. CHIEN, C.-H. CHO, J.-Z. CHEN, J.-S. CHANG, and S. JIANG: *Heavily Tm^{3+} -Doped Silicate Fiber for High-Gain Fiber Amplifiers*. *Fibers* 1, 82-92, 2013 (cit. on p. 12).
- [Lef13] LEFRANCOIS, S., C.-H. LIU, M. L. STOCK, T. SOSNOWSKI, A. GALVANAUSKAS, and F. W. WISE: *High-energy similariton fiber laser using chirally coupled core fiber*. *Opt. Lett.* **38**, 43-45, 2013 (cit. on p. 24).
- [Lef11] LEFRANCOIS, S., T. SOSNOWSKI, C.-H. LIU, A. GALVANAUSKAS, and F. W. WISE: *Energy scaling of mode-locked fiber lasers with chirally-coupled core fiber*. *Opt. Exp.* **19**, 3464-3470, 2011 (cit. on p. 24).
- [Lin06] LIN, Q. and G. P. AGRAWAL: *Raman response function for silica fibers*. *Opt. Lett.* 31 (21), 3086, 2006 (cit. on p. 15).
- [Liu09a] LIU, A., X. CHEN, M. J. LI, J. WANG, D. T. WALTON, and L. A. ZENTENO: *Comprehensive Modeling of Single Frequency Fiber Amplifiers for Mitigating Stimulated Brillouin Scattering*. *J. Lightwave Technol.* 27(13), 2189–2198, 2009 (cit. on p. 87).
- [Liu04] LIU, C.-H. and et AL.: *810W continuous-wave and single-transverse-mode fibre laser using 20um core Yb-doped double-clad fibre*. *Electronics Letters* 40(23), 1471-1472, 2004 (cit. on p. 10).
- [Liu07a] LIU, C.-H., G. CHANG, N. LITCHINISTER, A. GALVANAUSKAS, D. GUERTIN, N. JACOBSEN, and K. TANKALA: *Effectively single-mode chirally-coupled core fiber*. *Advanced Solid-State Photonics, OSA Technical Digest Series*, 2007 (cit. on pp. 20, 45).
- [Liu07b] LIU, C.-H., G. CHANG, N. LITCHINISTER, D. GUERTIN, N. JACOBSEN, K. TANKALA, and A. GALVANAUSKAS: *Chirally coupled core fibers at 1550nm and 1064nm for effectively single-mode core size scaling*. *Conference on Lasers et al.*, 2007 (cit. on pp. 19, 20, 23).
- [Liu09b] LIU, C.-H., S. HUANG, C. ZHU, and A. GALVANAUSKAS: *High Energy and High Power Pulsed Chirally-Coupled Core Fiber Laser System*. in *Adv. Solid-State Photonics, OSA Technical Digest Series (CD)*, 2009 (cit. on p. 23).
- [Lou16] LOUOT, C. and et AL.: *Supercontinuum Generation in an Ytterbium-Doped Photonic Crystal Fiber for CARS Spectroscopy*. *IEEE Photonics Technology Letters*, 28(19), pp. 2011-2014, 2016 (cit. on p. 11).
- [Ma11a] MA, X.: *Understanding and Controlling Angular Momentum Coupled Optical Waves in Chirally-Coupled-Core Fibers*. Thesis: The University of Michigan, 2011 (cit. on pp. 19–22).
- [Ma11b] MA, X., C.-H. LIU, G. CHANG, and A. GALVANAUSKAS: *Angular-momentum coupled optical waves in chirally-coupled-core fibers*. *Opt. Exp.* 19, 26515-26528, 2011 (cit. on pp. 4, 19, 20, 60).

-
- [Ma14] MA, X., C. ZHU, I.-N. HU, A. KAPLAN, and A. GALVANAUSKAS: *Single-mode chirally-coupled-core fibers with larger than 50 μm diameter cores*. Opt. Exp. **22**, 9206-9219, 2014 (cit. on p. 4).
- [Mac04] MACHEWIRTH, D., V. KHITROV, U. MANYAM, K. TANKALA, A. CARTER, J. ABRAMCZYK, J. FARRONI, D. GUERTIN, and N. JACOBSON: *Large mode area double clad fibers for pulsed and CW lasers and amplifiers*. Proceeding of SPIE Volume 5335, Fiber Lasers: Technology, Systems and Applications, pp. 140-150, 2004 (cit. on pp. 18, 52).
- [Mac07] MACHEWIRTH, D. P., Q. WANG, B. SAMSON, K. TANKALA, M. O'CONNOR, and M. ALAM: *Current developments in high-power monolithic polarization maintaining fiber amplifiers for coherent beam combining applications*. Proc. SPIE 6453, Fiber Lasers XI: Technology, Systems and Applications, 2007 (cit. on p. 35).
- [Mag94] MAGNE, S., Y. OUERDANE, M. DRUETTA, J. P. GOURE, P. FERDINAND, and G. MONNOM: *Cooperative luminescence in an ytterbium-doped silica fibre*. Optics Communications 111(3), 310-316, 1994 (cit. on p. 11).
- [Mar76] MARCUSE, D.: *Field deformation and loss caused by curvature of optical fibers*. Journal of the Optical Society of America 66(4), pp. 311-320, 1976 (cit. on p. 18).
- [Mar77] MARCUSE, D.: *Loss analysis of single-mode fiber splices*. The Bell System Technical Journal 56, 703-718, 1977 (cit. on p. 14).
- [Mar91a] MARCUSE, D.: *Theory of Dielectric Optical Waveguides*. 2nd ed. Academic Press Inc., 1991 (cit. on p. 8).
- [Mar91b] MARCUSE, D.: *Theory of Dielectric Optical Waveguides*. Academic Press Inc., 2nd edition, 1991 (cit. on p. 13).
- [Mar06] MARRUCCI, L., C. MANZO, and D. PAPARO: *Optical spin-to-orbital angular momentum conversion in homogeneous anisotropic media*. Physical Review Letters 96(16), pp. 1639051-1639054, 2006 (cit. on p. 21).
- [McC14] MCCOMB, T. S., D. MCCAL, R. FARROW, T. L. LOWDER, D. LOGAN, J. GREEN, T. N. KUTSCHA, C. YE, V. AALLOS, J. J. KOPONEN, and G. FANNING: *High-peak power, flexible-pulse parameter, chirally coupled core (3C) fiber-based picosecond MOPA systems*. Proc. SPIE 8961, Fiber Lasers XI: Technology, Systems and Applications, 896112, 2014 (cit. on p. 24).
- [McI78] MCINTYRE, P. and A. W. SNYDER: *Light Propagation in Twisted Anisotropic Media: Application to Photoreceptors*. J. Opt. Soc. Am., 68(2), 149 – 157, 1978 (cit. on p. 80).
- [Mer08] MERMELSTEIN, M. D., K. BRAR, M.J. ANDREJCO, A.D. YABLON, M. FISHTEYN, C. HEADLEY III, and D.J. DIGIOVANNI: *All-fiber 194 W single-frequency single-mode Yb-doped master-oscillator power amplifier*. Proc. SPIE 6873, 2008 (cit. on p. 3).

- [Mes08] MESCHÉDE, D.: *Optik, Licht und Laser*. Vieweg + Teubner, 3rd edition, 2008 (cit. on p. 12).
- [Mit10] MITSCHKE, F.: *Fiber Optics: Physics and Technology*. Springer, Berlin, 2010 (cit. on p. 13).
- [Mit05] MITSCHKE, F.: *Glasfasern*. Heidelberg: Elsevier-Spektrum Akademischer Verlag, 2005 (cit. on p. 8).
- [Mor08] MORGNER, U., M. ENGELBRECHT, D. WANDT, F. HAXSEN, A. RÜHL, and D. KRACHT: *High-power passively mode-locked thulium-doped fibre ring laser with variable dispersion compensation*. EPS-QEOD Europhoton Conference on Solid State, Fibre, and Waveguide Coherent Light Sources, 31. August-5. September, Paris, 2008 (cit. on p. 10).
- [Mor03] MORTENSEN, N. A., J. R. FOLKENBERG, M. D. NIELSEN, and K. P. HANSEN: *Modal cutoff and the V parameter in photonic crystal fibers*. Optics Lett. 28(20), 1879-1881, 2003 (cit. on p. 14).
- [Muk17] MUKHTUBAYEV, A. B., S. M. AKSARIN, and V. E. STRIGALEV: *Polarization extinction ratio of the polarization crosstalk caused by point pressure force in the polarization-maintaining fiber*. Optical Fiber Technology **38**, 119-122, 2017 (cit. on p. 9).
- [Mun19] MUNIZ-CÁNOVAS, P., Y. O. BARMENKOV, A. V. KIR'YANOV, J. L. CRUZ, and M. V. ANDRÉS: *ASE narrow-band noise pulsing in erbium-doped fiber amplifier and its effect on self-phase modulation*. Opt. Exp. 27, 8520-8528, 2019 (cit. on p. 12).
- [Nag82] NAGEL S., J. B. MACCHESNEY and K. WALKER: *An overview of the modified chemical vapor deposition (MCVD) process and performance*. IEEE J. Quant. Electron. 18 (4), pp. 459-476, 1982 (cit. on p. 8).
- [neoLase] *neoLase GmbH*. (accessed August 10, 2020). URL: <https://www.neolase.com> (cit. on p. 2).
- [New07] NEWELL, T.C., P. PETERSON, A. GAVRIELIDES, and M.P. SCHARMA: *Temperature effects on the emission properties of Yb-doped optical fibers*. Optics Communications 273(1), pp. 256-259, 2007 (cit. on p. 11).
- [Nic08] NICHOLSON, J. W., A. D. YABLON, S. RAMACHANDRAN, and S. GHALMI: *Spatially and spectrally resolved imaging of modal content in large-mode-area fibers*. Opt. Exp. 16(10), pp. 7233-7243, 2008 (cit. on pp. 36-38).
- [nLi20] *nLIGHT, Inc.* (accessed August 10, 2020). URL: <https://www.nlight.net/semiconductor-lasers-products> (cit. on pp. 9, 11).
- [Lie20] *nLIGHT, Inc.* (accessed August 10, 2020). URL: <https://www.nlight.net/optical-fibers-products> (cit. on pp. 10, 14).
- [Nod86] NODA J., OKAMOTO K. and SASAK Y.: *Polarization-maintaining fibers and their applications*. Journal of Lightwave Technology, vol. 4, no. 8, pp. 1071-1089, 1986 (cit. on p. 9).

-
- [Nuf20] *Nufern*. (accessed August 10, 2020). URL: https://www.nufern.com/pam/optical_fibers/ (cit. on pp. 10, 14, 18).
- [Nye74] NYE, J.F. and M.V. BERRY: *Dislocations in wave trains*. Proceedings of the Royal Society of London A - Mathematical and Physical Sciences 336(1605), pp. 165-190, 1974 (cit. on p. 21).
- [Oh12] OH, K. and U.-C. PAEK: *Silica Optical Fiber Technology for Devices and Components: Design, Fabrication, and International Standards*. Hoboken: Wiley, 2012 (cit. on p. 8).
- [Oka06] OKAMOTO, K.: *Fundamentals of Optical Waveguides*. Academic Press Inc., 2nd edition, 2006 (cit. on pp. 15, 20).
- [Opp17] OPPERMAN, P.: *Characterization and Stabilization of a High Power Fiber Amplifier Laser*. Thesis: PhD Leibniz U., Hannover, 2017 (cit. on p. 69).
- [Ott98] OTTAWAY, D. J., P.J. VEITCH, M. W. HAMILTON, C. HOLLITT, and J. MUNCH: *A compact injection-locked Nd:YAG laser for gravitational wave detection*. IEEE Journal of Quantum Electronics 34(10), 2006-2009, 1998 (cit. on p. 12).
- [Pas97a] PASCHOTTA, R. and et AL.: *Characterization and modeling of thulium:ZBLAN blue upconversion fiber lasers*. J. Opt. Soc. Am. B 14 (5), 1213, 1997 (cit. on p. 10).
- [Pas97b] PASCHOTTA, R. and et AL.: *Ytterbium-doped fiber amplifiers*. IEEE J. Quantum Electron. 33 (7), 1049, 1997 (cit. on pp. 10, 11, 88).
- [Pas97c] PASCHOTTA, R., J. NILSSON, R. P. BARBER, J. E. CAPLEN, A. C. TROPPER, and D. C. HANNA: *Limetime quenching in Yb doped fibers*. Optics Communications 136(5), 375-378, 1997 (cit. on p. 11).
- [Pas94] PASK, H. M., J.L. ARCHAMBAULT, D. C. HANNA, L. REEKIE, P. ST. RUSSELL, J. E. TOWNSEND, and A.C. TROPPER: *Operation of cladding-pumped Yb³⁺-doped silica fibre laser in 1 um region*. Electronics Letters 30(11), 863-865, 1994 (cit. on p. 11).
- [Pau12] PAURISSE, M., L. LEVEQUE, M. HANNA, F. DURON, and R. GEORGES: *Complete measurement of fiber modal content by wavefront analysis*. Optics Exp. 20(4), 4074-4084, 2012 (cit. on p. 63).
- [Per99] PERAL, E. and A. YARIV: *Degradation of Modulation and Noise Characteristics of Semiconductor Lasers After Propagation in Optical Fiber Due to a Phase Shift Induced by Stimulated Brillouin Scattering*. IEEE J. Quan. Electron. 35, 1185-1195, 1999 (cit. on pp. 25, 26, 34, 93).
- [Pes95] PESCHEL, U., T. PESCHEL, and F. LEDERER: *A compact device for highly efficient dispersion compensation in fiber transmission*. Applied Physics Letters 67(15), pp. 2111-2113, 1995 (cit. on p. 20).

- [Qi18] QI, X., S. CHEN, Z. LI, T. LIU, Y. OU, N. WANG, and J. HOU: *High-power visible-enhanced all-fiber supercontinuum generation in a seven-core photonic crystal fiber pumped at 1016 nm*. Opt. Lett. 43, 1019-1022, 2018 (cit. on p. 45).
- [Qiu94] QIU, R. C. and I.-T. LU: *Guided waves in chiral optical fibers*. J. Opt. Soc. Am. A. 11, 3212-3219, 1994 (cit. on p. 23).
- [Ram28] RAMAN, V. V. and K. S. KRISHNAN: *A new type of secondary radiation*. Nature 121, 501, 1928 (cit. on p. 15).
- [Rei97] REIDER, G.A.: *Photonik - Eine Einführung in die Grundlagen*. Springer-Verlag, 1st edition, 1997 (cit. on pp. 13, 14, 64).
- [Rob14] ROBIN, C., I. DAJANI, B. PULFORD, and C. VERGIEN: *Single-frequency Yb-doped photonic crystal fiber amplifier with 800W output power*. Proc. SPIE 8961, Fiber Lasers XI: Technology, Systems, and Applications, 2014 (cit. on pp. 4, 10).
- [Row00] ROWAN, S. and J. HOUGH: *Gravitational wave detection by interferometry (ground and space)*. Living Reviews in Relativity 3(3), 1-41, 2000 (cit. on p. 2).
- [Rus06] RUSSELL, P. ST. J.: *Photonic-crystal fibers*. Journal of Lightwave Technology 24(12), pp. 4729-4749, 2006 (cit. on p. 18).
- [Rus14] RUSSELL, P. ST. J. and et AL.: *Hollow-core photonic crystal fibres for gas-based nonlinear optics*. Nature Photon. 8, 278, 2014 (cit. on pp. 18, 45).
- [Saa09] SAAD, M.: 'Fluoride glass fiber: State of the art'. *Conf. Fiber Optic Sensors and Applications VI*. SPIE-The International Society for Optical Engineering. Orlando, FL, USA, 2009 (cit. on p. 8).
- [Sai05] SAITOH, K. and M. KOSHIBAL: *Empirical relations for simple design of photonic crystal fibers*. Opt. Exp. 13 (1), 267, 2005 (cit. on p. 18).
- [Sak78] SAKAI, J. and T. KIMURA: *Bending loss of propagation modes in arbitrary-index profile optical fibers*. Applied Optics 17(10), pp. 1499-1506, 1978 (cit. on p. 18).
- [Sch00] SCHAUDEL, B., P. GOLDNER, M. PRASSAS, and F. AUZEL: *Cooperative luminescence as a probe of clustering in Yb³⁺ doped glasses*. Journal of Alloys and Compounds 300, 443-449, 2000 (cit. on p. 11).
- [Sch99] SCHUTZ, B.F.: *Gravitational wave astronomy*. Classical and Quantum Gravity 16(12A), A131-A156, 1999 (cit. on p. 1).
- [Sha05] SHARPING, J. E., Y. OKAWACHI, and A. L. GAETA: *Wide bandwidth slow light using a Raman fiber amplifier*. Opt. Exp. 13, 6092-6098, 2005 (cit. on p. 16).
- [She90] SHEIK-BAHAE, M. and et AL.: *Dispersion and band-gap scaling of the electronic Kerr effect in solids associated with two-photon absorption*. Phys. Rev. Lett. 65 (1), 96, 1990 (cit. on p. 15).

-
- [Shi83] SHIBATA N. Sasaki Y., OKAMOTO K. and HOSAKA T.: *Fabrication of polarization-maintaining and absorption-reducing fibers*. IEEE Journal of Lightwave Technology 1 (1), pp. 38-43, 1983 (cit. on p. 9).
- [Sie93] SIEGMAN, A. E.: *Defining, Measuring, and Optimizing Laser Beam Quality*. in Proc. SPIE, 2, 1993 (cit. on p. 36).
- [Sie86] SIEGMAN, A.E.: *Lasers*. University Science Books, 1st edition, 1986 (cit. on p. 63).
- [Sig98] SIGG, D.: *Gravitational waves*. In Proceedings of TASI 98 (Theoretical Advanced Study Institute in Elementary Particle Physics), Publication LIGO-P980007-00-D, 1998 (cit. on p. 1).
- [Smi11] SMITH, A. V. and J. J. SMITH: *Mode instability in high power fiber amplifiers*. Opt. Exp. **19**(11), 10180, 2011 (cit. on p. 85).
- [Smi72] SMITH, R.: *Optical power handling capacity of low loss optical fibers as determined by stimulated Raman and Brillouin scattering*. Appl. Opt. 11(11), 2489–2494, 1972 (cit. on pp. 18, 65).
- [Sni88] SNITZER E. Po H., HAKIMI F. and MC COLLUM B.C.: *Double clad, offset core Nd fiber laser*. Optical Fiber Sensors, Vol. 2 of OSA Technical Digest Series, 1988 (cit. on p. 10).
- [Ste15] STEINKE, M.: *Fiber Amplifiers at 1.5 um for Gravitational Wave Detectors*. Thesis: PhD Leibniz U., Hannover, 2015 (cit. on pp. 13, 64).
- [Sté02] STÉPIEN, L., S. RANDOUX, and J. ZEMMOURI: *Origin of spectral hole burning in Brillouin fiber amplifiers and generators*. Phys. Rev. A 65, 053812, 2002 (cit. on p. 30).
- [Sto11] STOCK, M. L., C. H. LIU, A. KUZNETSOV, G. TUDURY, A. GALVANAUSKAS, and T. SOSNOWSKI: *Polarized, 100 kW peak power, high brightness nanosecond lasers based on 3C optical fiber*. Fiber Lasers VIII: Technology, Systems, and Applications, SPIE, 7914, 170 - 178, 2011 (cit. on p. 60).
- [Sto73] STOLEN, R. H. and E. P. IPPEN: *Raman gain in glass optical waveguide*. Appl. Phys. Lett. 22 (6), 276, 1973 (cit. on p. 16).
- [Tak95] TAKUSHIMA, Y. and K. KIKUCHI: *Spectral gain hole burning and modulation instability in a Brillouin fiber amplifier*. Opt. Lett. 20, 34-36, 1995 (cit. on p. 30).
- [Tan02] TANABE, S.: *Rare-earth-doped glasses for fiber amplifiers in broadband telecommunication*. C. R. Chimie 5, 815, 2002 (cit. on p. 10).
- [Tan06] TANG F. McNamara P., BARTON G. W. and RINGER S. P.: *Nanoscale characterization of silica soots and aluminium solution doping in optical fibre fabrication*. J. Non-Cryst. Solids 352 (36), pp. 3799–3807, 2006 (cit. on p. 8).
- [Tan11] TANKALA K. Guertin D., J. ABRAMCZYK and N. JACOBSON: *Reliability of low-index polymer coated double-clad fibers used in fiber lasers and amplifiers*. Optical Engineering 50(11), 1116071-1116078, 2011 (cit. on p. 10).

- [Ter14] TER-MIKIRTYCHEV, V.: *Fundamentals of Fiber Lasers and Fiber Amplifiers*. Springer Series in Optical Sciences 181, 2014 (cit. on pp. 8, 9).
- [The15] THEEG, T.: *Monolithischer Yb-Faserverstärker zur Leistungsskalierung von einfrequenter Laserquellen: Erforschung und Integration eines vollständig faserbasierten Pumplichtkopplers*. Thesis: PhD Leibniz U., Hannover, 2015 (cit. on pp. 69, 84, 87).
- [The16] THEEG, T., C. OTTENHUES, H. SAYINC, J. NEUMANN, and D. KRACHT: *Core-pumped single-frequency fiber amplifier with an output power of 158 W*. Opt. Lett. 41, 9-12, 2016 (cit. on p. 11).
- [The12a] THEEG, T., H. SAYINC, J. NEUMANN, and D. KRACHT: *All-Fiber Counter Propagation Pumped Single Frequency Amplifier Stage With 300 W Output Power*. IEEE Photonics Technology Letters 24(20), 1864-1867, 2012 (cit. on pp. 3, 4).
- [The12b] THEEG, T., H. SAYINC, J. NEUMANN, L. OVERMEYER, and D. KRACHT: *Pump and signal combiner for bi-directional pumping of all-fiber lasers and amplifiers*. Opt. Exp. 20, 28125-28141, 2012 (cit. on pp. 35, 52, 54, 57, 79).
- [Thi19] THIES, F., N. BODE, P. OPPERMANN, M. FREDE, B. SCHULZ, and B. WILLKE: *Nd:YVO₄ high-power master oscillator power amplifier laser system for second-generation gravitational wave detectors*. Opt. Lett. 44, 719-722, 2019 (cit. on pp. 2, 65, 85).
- [Tur81] TURNER, E. H. and R. H. STOLEN: *Fiber Faraday circulator or isolator*. Opt. Lett. 6 (7), 322, 1981 (cit. on p. 71).
- [Ung08] UNGER, S., A. SCHWUCHOW, S. JETSCHKE, V. REICHEL, A. SCHEFFEL, and J. KIRCHHOFF: *Optical properties of Yb-doped laser fibers in dependence on codopants and preparation conditions*. Proceedings of SPIE Vol. 6890 - Optical Components and Materials V, 6890161-68901611, 2008 (cit. on p. 11).
- [Urq88] URQUHART, P.: *Review of rare earth doped fibre lasers and amplifiers*. IEE Proceedings 135(6), 385-407, 1988 (cit. on p. 11).
- [Var17a] VARONA, O. de, W. FITTKAU, P. BOOKER, T. THEEG, M. STEINKE, D. KRACHT, J. NEUMANN, and P. WESSELS: *Single-frequency fiber amplifier at 1.5 μm with 100 W in the linearly-polarized TEM₀₀ mode for next-generation gravitational wave detectors*. Opt. Express 25, 24880-24892, 2017 (cit. on p. 11).
- [Var17b] VARONA, O. de, W. FITTKAU, P. BOOKER, T. THEEG, M. STEINKE, D. KRACHT, J. NEUMANN, and P. WESSELS: *Single-frequency fiber amplifier at 1.5 μm with 100 W in the linearly-polarized TEM₀₀ mode for next-generation gravitational wave detectors*. Opt. Exp. 25, 24880-24892, 2017 (cit. on pp. 3, 62, 74, 84).
- [Web72] WEBER, J.: *Advances in gravitational radiation detection*. General Relativity and Gravitation 3, 59, 1972 (cit. on p. 2).

-
- [Web69] WEBER, J.: *Evidence for Discovery of Gravitational Radiation*. Physical Review Letters **22**(24), 1320-1324, 1969 (cit. on p. 1).
- [Web71] WEBER, J.: *The detection of gravitational waves*. Scientific American **224**, 22-29, 1971 (cit. on p. 2).
- [Wel21] WELLMANN, F., N. BODE, P. WESSELS, L. OVERMEYER, J. NEUMANN, B. WILLKE, and D. KRACHT: *Low noise 400 W coherently combined single frequency laser beam for next generation gravitational wave detectors*. Opt. Exp. **29**, 10140-10149, 2021 (cit. on pp. 4, 95).
- [Wel19] WELLMANN, F., M. STEINKE, F. MEYLAHN, N. BODE, B. WILLKE, L. OVERMEYER, J. NEUMANN, and D. KRACHT: *High power, single-frequency, monolithic fiber amplifier for the next generation of gravitational wave detectors*. Opt. Exp. **27**(20), 28523-28533, 2019 (cit. on pp. 3, 52, 61, 65, 69, 77, 84).
- [Wie07] WIELANDY, S.: *Implications of Higher-Order Mode Content in Large Mode Area Fibers with Good Beam Quality*. Opt. Exp. **15**(15), 402-15, 2007 (cit. on pp. 36, 82).
- [Wie16] WIENKE, A., H. SAYINC, C. OTTENHUES, S. YILMAZ, D. KRACHT, M. WYSMOLEK, D. WANDT, K. HAUSMANN, and J. NEUMANN: *Innovative Laser Sources Operating Around 2 um*. Physics Procedia (83), 1184-1195, 2016 (cit. on p. 10).
- [Wil12] WILLKE, B. and et AL: *Pre-Stabilized Laser Subsystem Testing and Acceptance - L1 PSL*. Technical Report No.LIGO-E1100716-v6, 2012 (cit. on p. 84).
- [Win11] WINKELMANN, L., O. PUNCKEN, R. KLUZIK, C. VELTKAMP, P. KWEE, J. POELD, C. BOGAN, B. WILLKE, M. FREDE, J. NEUMANN, P. WESSELS, and D. KRACHT: *Injection-locked single-frequency laser with an output power of 220W*. Appl. Phys. B **102**(3), 529, 2011 (cit. on pp. 2, 85).
- [Wys18] WYSMOLEK, M., C. OTTENHUES, T. PULZER, T. THEEG, H. SAYINC, M. STEINKE, U. MORGNER, J. NEUMANN, and D. KRACHT: *Microstructured Fiber Cladding Light Stripper for Kilowatt-Class Laser Systems*. Appl. Opt. **57** (23), 6640-6644, 2018 (cit. on pp. 28, 50, 70).
- [Y80] Y., FUJII and SANOS K.: *Polarization transmission characteristics of optical fibers with elliptical cross section*. Electron. Comm. Jpn. Pt. I, pp. 87-93, 1980 (cit. on p. 9).
- [Yeh90] YEH, C.: *Handbook of Fiber Optics: Theory and Applications*. 4th ed. Academic Press, 1990 (cit. on p. 8).
- [Yin17] YIN, L., M. YAN, Z. HAN, H. WANG, H. SHEN, and R. ZHU: *High power cladding light stripper using segmented corrosion method: theoretical and experimental studies*. Opt. Exp. **25**, 8760-8776, 2017 (cit. on p. 50).

- [Yod06] YODA, H., O. POLYNKIN, and M. MANSURIPUR: *Beam Quality Factor of Higher Order Modes in a Step-Index Fiber*. J. Lightwave Technol. 24, 1350–1355, 2006 (cit. on p. 36).
- [Zel97] ZELLMER H. Tünnermann A., WELLING H. and REICHEL V.: *Double-clad fiber laser with 30 W output power*. Optical Amplifiers and Their Applications, p. FAW18, 1997 (cit. on p. 10).
- [Zen93] ZENTENO, L.: *High-power double clad fiber lasers*. Journal of Lightwave Technology 11(9), 1435-1446, 1993 (cit. on pp. 10, 12).
- [Zha18a] ZHAN, H. and et AL: *Pump-gain integrated functional laser fiber towards 10kW-level high-power applications*. Laser Physics Letters 15.9, 095107, 2018 (cit. on p. 3).
- [Zha05] ZHANG, J. and M.R. PHILLIPS: *Modeling Intensity Noise Caused by Stimulated Brillouin Scattering in Optical Fibers*. Conference on Lasers and Electro-Optics, 2005 (cit. on pp. 25, 26, 34, 93).
- [Zha18b] ZHAO, J., G. GUIRAUD, C. PIERRE, F. FLOISSAT, A. CASANOVA, A. HREIBI, W. CHAIBI, N. TRAYNO, J. BOULLET, and G. SANTARELLI: *High-power all-fiber ultra-low noise laser*. Appl. Phys. B 124, 114, 2018 (cit. on p. 45).
- [Zhe18] ZHENG, J., W. ZHAO, B. ZHAO, Z. LI, C. CHANG, G. LI, Q. GAO, P. JU, W. GAO, S. SHE, P. WU, C. HOU, and W. LI: *High pumping-power fiber combiner for double-cladding fiber lasers and amplifiers*. Opt. Eng. 57(3), 036105, 2018 (cit. on p. 52).
- [Zhu11] ZHU, C., I. HU, X. MA, and A. GALVANAUSKAS: *Single-frequency and single-transverse mode Yb-doped CCC fiber MOPA with robust polarization SBS-free 511W output*. Advances in Optical Materials, OSA Technical Digest (CD) (Optical Society of America), 2011 (cit. on pp. 3, 80).
- [Zhu19] ZHU, S., J. LI, L. LI, K. SUN, C. HU, X. SHAO, and X. MA: *Impact of the heat load on the laser performance of chirally-coupled-core fibers*. Opt. Exp. 27(26), 2019 (cit. on pp. 24, 75, 84).

List of Figures

2.1	Visualization of a cross-section of a typical step-index fiber in a) with the corresponding refractive index profile in b). The parameter $r_{\text{co/cl}}$ and $n_{\text{co/cl}}$ denote the radius and refractive indices of the core and cladding. In c) a polarization-maintaining fiber is shown in a PANDA configuration. Other fiber designs with additional rotating side cores were developed such as chirally-coupled core fibers in d).	7
2.2	(a): Schematic overview of the important energy levels of Yb^{3+} -doped silica as presented in Ref. [New07]. (b): Typical absorption and emission cross-sections of Yb^{3+} -doped silica at around $1.0 \mu\text{m}$ [Pas97b].	11
2.3	Illustration of the phenomena of stimulated Brillouin scattering (a): Schematic energy transfer from the injected pump and frequency-shifted signal wave. (b): Corresponding intensity pattern inside the fiber due to interference of propagating waves. (c): Moving acoustic wave by material density fluctuations. (d): Time-dependent change of the refractive index of the medium, where pump light will be scattered.	16
2.4	Lorentzian Brillouin gain spectrum $g_{\text{B}}(\nu)$ in dependence of frequency in conjunction with the bandwidth Ω_{BS} and the Brillouin gain coefficient $g_{\text{B}0}$ at frequency shift ν_{B} according to Eq. 2.15.	17
2.5	Schematic 3D geometry of the $3\text{C}^{\text{®}}$ -fiber structure with a single side core with a constant helix pitch Λ_{helix} and helix offset R_{helix}	19
2.6	Visualization of the spin optical angular momentum (SAM) with the modes wavelength in fiber's propagation z-axis and the electric field vector \mathbf{E} corresponding to a circular polarized field in a Cartesian coordinate system according to [Ma11a].	20
2.7	Visualization of the orbital optical angular momentum (OAM) with the modes wavelength in fiber's propagation z-axis and the electric field vector \mathbf{E} corresponding to the phase front of the electric field rotates and propagates at the same time according to [Ma11a]. The azimuthal phase completes a full 2π rotation in the transverse plane.	21
2.8	Simplified physical illustration in a case of matched phase-velocity between the LP_{01} - and the LP_{11} -mode in a $3\text{C}^{\text{®}}$ -fiber. The plot presents the corresponding overlap integral of the modes at different rotation angles.	22
2.9	Simplified physical illustration of QPM in a case of unmatched phase-velocity between the LP_{01} - and the LP_{11} -mode in a $3\text{C}^{\text{®}}$ -fiber. The plot presents the corresponding constant overlap integral of the modes at different rotation angles.	23

3.1	Phasor diagram for amplitude (a) and phase (b) modulated light with the carrier field (red arrow) and the sideband vectors (blue arrows). The resulting modulated oscillation is shown in a green arrow. The time-dependent projection of the electric field is depicted to the right of the corresponding phasor diagram.	26
3.2	Principle of the conversion from phase to intensity noise based on an asymmetric Brillouin loss and a corresponding asymmetric phase shift for the transmitted signal. A symmetric gain or loss spectrum has no influence on the amplitude and the sidebands experience a pure PM. Due to an asymmetric spectrum (right), the sidebands experience a differential loss and phase shift and the pure phase modulation is converted into a mixture of amplitude and phase modulation.	27
3.3	Experimental setup for intensity noise measurements of the transmitted light above the SBS threshold. The system consisted of an NPRO for the signal beam, a monolithic fiber amplifier and a single-mode fiber for the generation of SBS. The connection between the MOPA stage and the single-mode fiber was either a high power fiber isolator (at higher signal power b)) or a circulator (at lower signal power a)) to measure the Brillouin gain spectrum. CLS: cladding light stripper, PC: pump combiner, L_i : lens. Splices are represented by x.	28
3.4	Measured stimulated Brillouin scattering gain spectrum: a) Spectrum of a 20 m single-mode fiber at a frequency shift of around 14.7 GHz and a fitted asymmetric Lorentzian profile. b) Gain profile at different signal power levels with a 20 m single-mode fiber.	29
3.5	Intensity noise spectrum of the transmitted signal below and above the SBS threshold P_B for a fiber length of 20 m. The differences of the eigenfrequencies are marked as $\Delta\nu_i$	30
3.6	Shift of the phase of the round trip without (red dashed line) and with an additional phase shift due to SBS (blue line). The insert visualizes the case for the shifted round trip of 2π and 4π with a corresponding eigenfrequency of 2.8 MHz and 5.7 MHz.	31
3.7	Intensity noise of the transmitted signal above the SBS threshold P_B in a frequency range from 13 to 17 MHz. The splitting of the resonances expressed by the red arrows indicates an asymmetric gain profile.	32
3.8	Intensity noise spectrum of the transmitted light above and below the SBS threshold P_B . A model of the noise for three measurements based on an asymmetric Lorentzian gain spectrum and a conversion from phase to intensity noise is shown in red.	33
4.1	(a) Visualization of a S^2 imaging setup. (b) Typical optical spectrum measured at an arbitrary (x,y) point and (c) the Fourier transform of the optical spectrum by (b) showing multiple beat frequencies according to Ref. [Nic08].	37

4.2	Schematic comparison between a conventional S^2 imaging setup in (a) and an approach of a S^2 technique for real time measurements in (b) [Gra16].	39
4.3	Setup of an all-fiber tunable fiber filter based on a Fabry-Perot cavity (FFP-TF) in a). The transmission spectrum of the normalized intensity in dependence of the wavelength is shown in b).	40
4.4	Setup of an S^2 -measurement including an all-fiber tunable fiber laser based on a Fiber Fabry-Perot tunable filter (FFP-TF) and a high-speed CMOS camera. WDM: wavelength-division multiplexer.	41
4.5	Optical spectrum of the ASE input signal in front of the Fiber Fabry-Perot tunable filter in black and the narrow-band transmission afterwards at different voltages applied to the filter in color.	42
4.6	Cross-sectional microscope image of the 34/250DC-3C fiber. The 34 μm core is surrounded by a single side core.	43
4.7	Comparison of the S^2 -imaging results of $3C^{\text{®}}$ -fiber, a tapered $3C^{\text{®}}$ -fiber and a standard LMA fiber. The reconstruction of the corresponding modes at b and c is presented in Fig. 4.8.	44
4.8	Reconstruction of the optical modes (b+c) guided in the side core of a tapered 34/250DC-3C fiber. a): Entire beam profile captured with a CMOS camera.	44
4.9	Illustration of the designed mode field adapter with a standard polarization-maintaining SM-fiber (PLMA-GDF-10/125-M, <i>Nufern</i>) and a $3C^{\text{®}}$ -fiber (34/250DC-3C).	46
4.10	Image of a splice of the MFA between a standard polarization-maintaining SM-fiber (right side: PLMA-GDF-10/125-M, <i>Nufern</i>) and a tapered $3C^{\text{®}}$ -fiber (left side: 34/250DC-3C).	46
4.11	Results of the S^2 imaging technique: Fourier transforms of the optical spectrum of a $3C^{\text{®}}$ -fiber-MFA compared with an untreated and tapered $3C^{\text{®}}$ -fiber and a typical LMA fiber (PLMA-GDF-25/205-M, <i>Nufern</i>). The corresponding beam profile and the reconstruction of the mode at the beat-frequency (b) at 0.9 ps/m is shown in Fig. 4.12.	47
4.12	Left: The beam profile integrated across the optical spectrum after the $3C^{\text{®}}$ -fiber of the MFA. Right: Reconstruction of the LP_{11} -mode, which is exclusively guided in the sidecore.	48
4.13	(a): Image of the tapered $3C^{\text{®}}$ -fiber, where the cladding diameter is reduced to 125 μm and spliced on an end cap. (b): Image of the mount for the end cap including the tapered $3C^{\text{®}}$ -fiber.	48
4.14	Image of a fabricated cladding light stripper integrated in a $3C^{\text{®}}$ -fiber with micro-structured grooves on a single side in (a), on two sides in (b) and on three sides in (c).	49

4.15	Experimental setup for the characterization of the cladding light stripper. In a), a 30 W pump diode was spliced to the 3C [®] -fiber to measure the attenuation by the CLS. In b), the light of an NPRO was guided through the core of the 3C [®] -fiber to determine the impact of the CLS on the core light. Afterwards, the optical output power was measured with a thermal power head.	50
4.16	Cladding light attenuation of the first in-house cladding light stripper directly integrated in a 3C [®] -fiber with an optical suppression of ~19 dB, which is comparable to components based on standard fibers.	51
4.17	The signal light attenuation of the in-house designed cladding light stripper directly integrated in a 3C [®] -fiber is below the verifiable accuracy.	51
4.18	Schematic side view of a side-pumped 3C [®] -fiber including important ray paths. The pump fiber is spliced to a tapered coreless intermediate fiber, which enables an efficient pump light coupling to the 3C [®] -fiber.	53
4.19	3C [®] -fiber (34/250DC-3C) combiner with up to four fiber coupled pump diodes (150 W each at 976 nm).	54
4.20	Experimental output power results (red) of the combined pump power for a 4+1x1 high-power fiber combiner integrated in a 3C [®] -fiber. The corresponding coupling efficiency of total diode power to the 3C [®] -fiber is shown in blue in percent.	54
4.21	Experimental output power results (red) of the combined pump power for a 2+1x1 high-power fiber combiner integrated in a standard fiber with a octagonal structure. The corresponding coupling efficiency of total diode power to the signal fiber is shown in blue in percent.	55
4.22	Cross-section images of a two port 3C [®] -fiber pump combiner in a)-c) and of a pump combiner based on a fiber with octagonal cladding structure in d)-f) at different positions in the combiner. The two PFs are at all time in contact with the octagonal fiber, whereas the IF is not permanently attached on the 3C [®] -fiber.	56
5.1	Experimental setup of a monolithic amplifier based on a 3C [®] -fiber. The system consists of a non-planar ring oscillator (NPRO), a cladding light stripper (CLS) and a pump combiner integrated in a single-mode fiber. The Yb-doped 3C [®] -fiber is adapted to the single-mode fiber via a mode field adapter (MFA). x: splice.	60
5.2	Slope of the 3C [®] -fiber amplifier prototype with measured data (blue squares) and a linear fit (red line). The slope efficiency of the absorbed pump power to optical output power is calculated to be 71%.	61
5.3	Evolution of the optical output power of the amplifier system over 3.5 days.	62
5.4	Evolution of the polarization extinction ratio at different output power levels in (a) and the evolution of the PER over 5 hours at the maximum output power of 100 W in (b).	63

5.5	Modal content measurement setup with scanning ring-cavity. The input power is adjusted by a power tuning stage and two lenses enable the mode matching to the cavity. PBS: Polarization beam splitter; PZT: Piezo.	64
5.6	Mode scan at an output power of 103 W with a fundamental mode content of 98.9%. The normalized intensity is shown in dependence of the frequency over one free spectral range of the cavity.	65
5.7	Relative intensity noise of the optical amplifier output at different power levels up to 103 W with no onset of SBS.	66
5.8	Evolution of the temperature of the MFA at different output power levels and time.	67
6.1	Experimental setup of an all-fiber amplifier based on a 3C [®] -fiber. The system consists of a non-planar ring oscillator (NPRO), a cladding light stripper (CLS) and a pump combiner integrated in a single-mode fiber. The Yb-doped 3C [®] -fiber is adapted to the single-mode fiber via a mode field adapter (MFA). x: splice.	70
6.2	Image of the alignment of two cleaved 3C [®] -fibers in (a) and the subsequent splice in (b). In (c) an image of an angle-cleaved 3C [®] -fiber is shown.	71
6.3	Schematic 3D-illustration of the interface between the pre- and the main-amplifier including an Faraday isolator.	72
6.4	Theoretical calculation of the beam waist at the position of the 3C [®] -fiber end facet (red) at different input power levels of the pre-amplifier and the corresponding optical losses (blue) in %. The device is optimized for the operating power level of 15 W.	73
6.5	Slope of the 170 W 3C [®] -fiber amplifier with an optical efficiency of the absorbed pump power to optical output power of 75%.	74
6.6	Slope of the 3C [®] -fiber amplifier with an optical efficiency of the absorbed pump power to optical output power of 75%.	74
6.7	Experimental setup of a high-power all-3C [®] -fiber amplifier with an output power level of 336 W. The system in MOPA configuration consists of a non-planar ring oscillator (NPRO) as seed laser, a standard-fiber pre-amplifier and a main-amplifier based on a Yb-doped 3C [®] -fiber with an integrated high-power pump combiner. CLS: Cladding light stripper, PC: pump combiner, MFA: mode field adapter.	76
6.8	Slope of the used pre-amplifier with measured data (blue dots) and a linear fit (red line) with an optical-to-optical efficiency of 82%.	77
6.9	Evolution of the optical output power level of the pre-amplifier over a time scale of one day in red. Additionally, the corresponding results of the PER in blue with and without a temperature-stabilized spool.	78
6.10	(a): Slope of the amplifier with measured data (blue squares) and a linear fit (red line). The residual pump light of the pump combiner is shown in green. (b): Pump combiner integrated in the 3C [®] -fiber with different fiber outputs for the non-transferred pump light.	79

6.11	Optical spectrum at the maximum output power level of 336 W with a resolution bandwidth of 0.02 nm.	79
6.12	Evolution of the polarization extinction ratio of 3C [®] -fiber main-amplifier and the pre-amplifier at different output power levels over 30 minutes. . . .	80
6.13	Long-term power stability measurement of the 3C [®] -fiber amplifier at an output power of 336 W in red and the corresponding pre-amplifier in orange. Additionally the behavior of the output power at 336 W is shown in detail in the upper plot. The temperature of the high-power pump combiner integrated in the 3C [®] -fiber is shown in blue.	81
6.14	(a): Mode scan at an output power of 336W with a fundamental mode content of 90.4%. The normalized intensity is shown in dependence of the cavity length over one free spectral range of the ring-cavity. (b): Image of the beam profile measured with a CCD camera.	83
6.15	TEM ₀₀ -mode content of 3C [®] -fiber main-amplifier at different output power level. All measurements are above the requirements for GWs of a TEM ₀₀ mode content of more than 90% [Abe11].	83
6.16	Relative power noise measurements of the 3C [®] -fiber amplifier system in comparison with the 200 W solid-state laser developed for the aLIGO detectors.	84
6.17	(a): Relative power noise spectra at different output power levels without an aperture in the sampled beam. (b): Relative power noise spectra with an aperture in the sampled beam to convert modal fluctuations into power fluctuations.	85
6.18	Relative power noise spectra at different power levels up to a frequency range of 30 MHz. a): With an additional integrated Noise Eater (NE) technology. b): Without a NE. At 336 W a slight noise increase in the 5 MHz range can be detected.	87
6.19	Evolution of the photodiode voltage detecting the optical output power of a fiber-coupled high-power pump diode. After a trigger event, the interlock system shut down the optical power within a 1 μ s.	88
6.20	Evolution of the photodiode voltage detecting the optical output power in a) in front of and in b) behind a fiber amplifier system. Both plots illustrate the behavior of the amplifier with an activated and without an interlock system. With an deactivated interlock, the laser was damaged irreversible due to parasitic lasing effects.	89
6.21	Image of the circuit board of the interlock system in a) and illustration of the implementation to an existing automation laser control system by <i>Beckhoff</i>	90
7.1	Historical overview of the output power levels achieved with 3C [®] -fibers amplifier systems. The results of this work (green squares) are taken into the scientific context with previous systems (blue squares). For the first time, the presented architectures are all-fiber amplifier designs. Since 2015, nLight has been distributing the 3C [®] -fibers.	94

A.1	Schematic illustration of the advanced mode field adapter with an integrated isolator. This laboratory prototype served as an first experimental approach to investigate the performance of the final component.	123
A.2	Calculation of the beam propagation by using the Gaussian optic. The optical effect of the thermal lens was added by including the heat input per infinitesimally small segment and the resulting optical lens in the medium. The propagation of the beam with an optical power of 100 mW is shown in blue and with a power level of 15 W in red. The gray blocks represents the corresponding optics.	124
B.1	Printed circuit board of the interlock system.	125
B.2	Electrical layout of the interlock system. The label of the positions corresponds to the Table B.1.	125

List of Tables

3.1	Measured and calculated resonator eigenfrequencies at different fiber lengths	31
4.1	Relevant specifications of the corresponding FFP-TF	41
4.2	Relevant specifications of the CMOS camera (ace-acA2000-165um-NIR). W: width, H: height.	42
4.3	Parameters of the 34/250DC-3C provided by <i>nLight Oy</i>	43
B.1	List of electrical components of the interlock system.	126

A Advanced mode field adapter

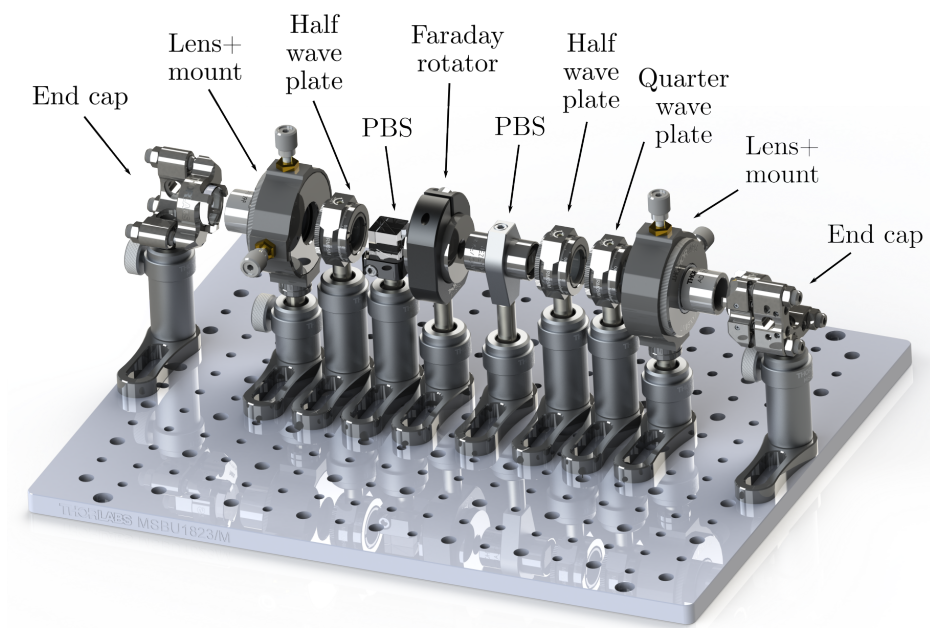


Figure A.1: Schematic illustration of the advanced mode field adapter with an integrated isolator. This laboratory prototype served as an first experimental approach to investigate the performance of the final component.

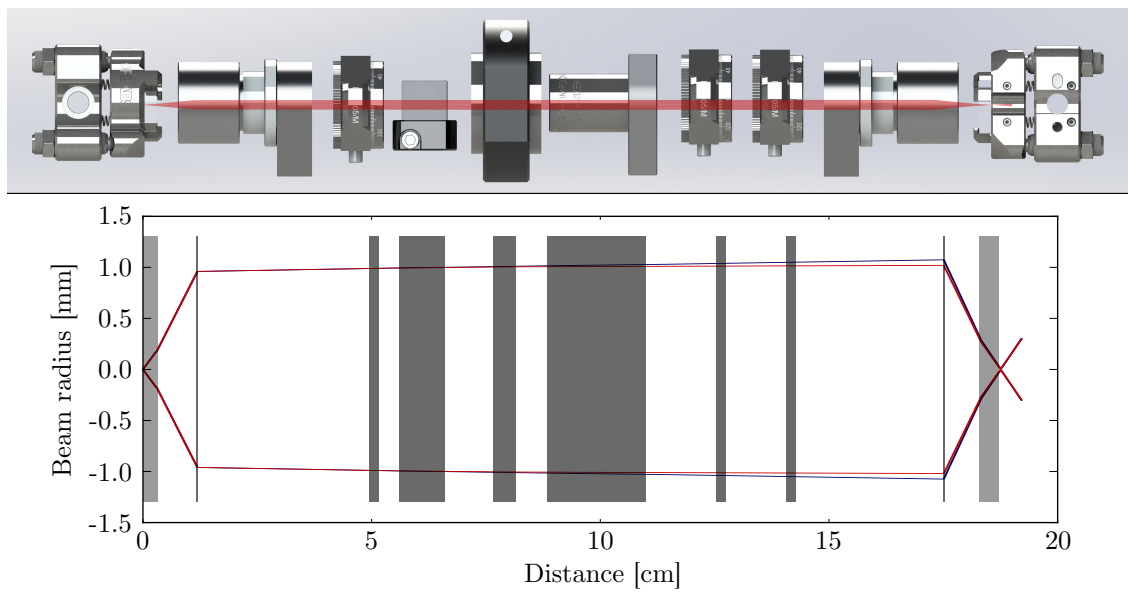


Figure A.2: Calculation of the beam propagation by using the Gaussian optic. The optical effect of the thermal lens was added by including the heat input per infinitesimally small segment and the resulting optical lens in the medium. The propagation of the beam with an optical power of 100 mW is shown in blue and with a power level of 15 W in red. The gray blocks represents the corresponding optics.

B Automatic interlock system

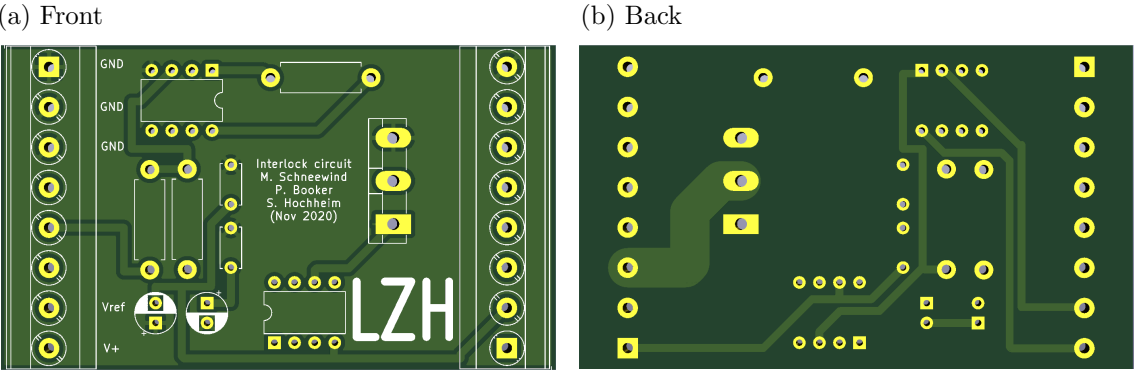


Figure B.1: Printed circuit board of the interlock system.

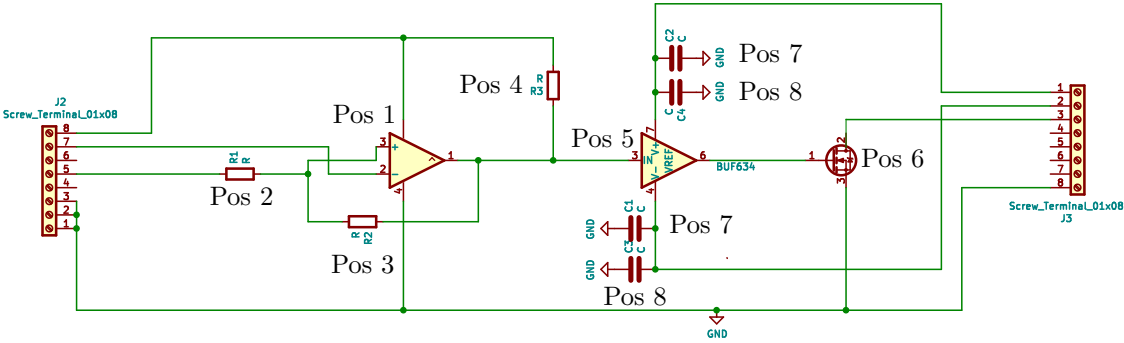


Figure B.2: Electrical layout of the interlock system. The label of the positions corresponds to the Table B.1.

B.1 List of used electrical components

Table B.1: List of electrical components of the interlock system.

Position	Component	Description
1	comparator	TLC372CP
2	resistance R1	10k Ω
3	resistance R2	100k Ω
4	resistance R3	5k Ω
5	MOSFET	IXTH80N65X2
6	MOSFET driver	BUF634
7	capacitor C1,C2	10 μ F
8	capacitor C3,C4	10 nF

Publications

Scientific publications in peer-reviewed journals

1. **Hochheim, S.**, E. BROCKMÜLLER, P. WESSELS, J. KOPONEN, T. LOWDER, S. NOVOTNY, J. NEUMANN, and D. KRACHT: *Single-frequency 336 W spliceless all-fiber amplifier based on a chirally-coupled-core fiber for the next generation of gravitational wave detectors*. in Journal of Lightwave Technology, doi: 10.1109/JLT.2021.3133814, 2021.
2. **Hochheim, S.**, E. BROCKMÜLLER, P. WESSELS, M. STEINKE, J. KOPONEN, T. LOWDER, S. NOVOTNY, J. NEUMANN, and D. KRACHT: *Highly-integrated signal and pump combiner in chirally-coupled-core fibers for all-fiber lasers and amplifiers*. in Journal of Lightwave Technology, doi: 10.1109/JLT.2021.3111993, 2021.
3. **Hochheim, S.**, J. NEUMANN, D. KRACHT, and M. STEINKE: *Broadband excess intensity noise due to an asymmetric Brillouin gain spectrum in optical fibers*. OSA Continuum 3, 2902-2911, 2020.
4. **Hochheim, S.**, M. STEINKE, P. WESSELS, O. de VARONA, J. KOPONEN, T. LOWDER, S. NOVOTNY, J. NEUMANN, and D. KRACHT: *Single-frequency chirally-coupled-core all-fiber amplifier with 100 W in a linearly-polarized TEM₀₀-mode*. Opt. Lett. 45, 939-942, 2020.

Invited submissions to international conferences

1. **Hochheim, S.**, F. WELLMANN, T. THEEG, O. de VARONA, P. BOOKER, P. WESSELS, M. STEINKE, J. NEUMANN, and D. KRACHT: *Monolithic fiber amplifiers for the next generation of gravitational wave detectors*. Proc. SPIE 10683, Fiber Lasers and Glass Photonics: Materials through Applications, 1068320, 2018.

Submissions to international conferences

1. BROCKMÜLLER, E., **S. Hochheim**, P. WESSELS, J. KOPONEN, T. LOWDER, S. NOVOTNY, J. NEUMANN, and D. KRACHT: *Pump combiner with chirally coupled core fibers for side pumped single frequency all fiber amplifiers*. Proc. SPIE 11667, Components and Packaging for Laser Systems VII, 116670J, 2021.
2. **Hochheim, S.**, E. BROCKMÜLLER, P. WESSELS, J. KOPONEN, T. LOWDER, S. NOVOTNY, J. NEUMANN, and D. KRACHT: *Integrated signal and pump combiner in chirally-coupled-core fibers for all-fiber lasers and amplifiers*. in OSA Advanced Photonics Congress (AP) 2020 (IPR, NP, NOMA, Networks, PVLED, PSC, SPPCom, SOF), 2020.

3. **Hochheim, S.**, E. BROCKMÜLLER, P. WESSELS, J. KOPONEN, T. LOWDER, S. NOVOTNY, J. NEUMANN, and D. KRACHT: *Low noise spliceless single-frequency chirally-coupled-core all-fiber amplifier*. Proc. SPIE 11665, Fiber Lasers XVIII: Technology and Systems, 116651L, 2021.
4. **Hochheim, S.**, E. BROCKMÜLLER, P. WESSELS, M. STEINKE, J. KOPONEN, T. LOWDER, S. NOVOTNY, J. NEUMANN, and D. KRACHT: *Integrated fiber components based on chirally-coupled-core fibers for all-fiber amplifier*. Proc. SPIE 11357, Fiber Lasers and Glass Photonics: Materials through Applications II, 113570Y, 2020.
5. **Hochheim, S.**, R. HOUSSAINI, M. STEINKE, J. NEUMANN, and D. KRACHT: *Monolithic tunable fiber laser for real-time S^2 -measurements*. 8th EPS-QEOD Europhoton Conference, 2018.
6. **Hochheim, S.**, J. NEUMANN, D. KRACHT, and M. STEINKE: *Broadband excess intensity noise due to an asymmetric Brillouin gain spectrum in optical fibers*. Proc. SPIE 10897, Fiber Lasers XVI: Technology and Systems, 108971R, 2019.
7. **Hochheim, S.**, M. STEINKE, P. WESSELS, J. KOPONEN, T. LOWDER, S. NOVOTNY, J. NEUMANN, and D. KRACHT: *Monolithic amplifier based on a Chirally-coupled-core fiber*. in Conference on Lasers, Electro-Optics Europe, and European Quantum Electronics Conference, OSA Technical Digest (Optical Society of America), 2019.
8. **Hochheim, S.**, M. STEINKE, P. WESSELS, O. de VARONA, J. KOPONEN, T. LOWDER, S. NOVOTNY, J. NEUMANN, and D. KRACHT: *Single-frequency chirally-coupled-core all-fiber amplifier with 100 W in a linearly-polarized TEM_{00} -mode*. Proc. SPIE 11260, Fiber Lasers XVII: Technology and Systems, 112601C, 2020.

Submissions to LVK meetings

1. **Hochheim, S.**, P. BOOKER, F. WELLMANN, O. de VARONA, F. THIES, N. BODE, M. PICKENPACK, L. WEI, M. STEINKE, J. NEUMANN, B. WILLKE, and D. KRACHT: *Further power scaling in fiber amplifiers: Challenges and concepts*. LVC March 2019, LIGO Document G1900507, 2019.
2. **Hochheim, S.**, P. BOOKER, P. WESSELS, O. de VARONA, J. KOPONEN, T. LOWDER, S. NOVOTNY, J. NEUMANN, B. WILLKE, and D. KRACHT: *Power scaling concepts for fiber amplifiers at 1.0 μm and 1.5 μm* . LVC March 2020, LIGO Document G2000403, 2020.
3. **Hochheim, S.**, E. BROCKMÜLLER, P. WESSELS, J. KOPONEN, T. LOWDER, S. NOVOTNY, J. NEUMANN, B. WILLKE, and D. KRACHT: *Single-frequency 336 W spliceless all-fiber amplifier based on a chirally-coupled-core fiber*. LVC September 2020, LIGO Document G2001553, 2020.

Curriculum Vitae

Personal Data

Name Sven Hochheim
Date of birth 29.03.1991 in Gehrden
Family status married

Education

1998 - 2002 Berlinschule Bad Nenndorf
2002 - 2004 Orientierungsstufe Bad Nenndorf
2004 - 2010 Gymnasium Bad Nenndorf
May 2010 Abitur

Zivildienst

2010 - 2011 Rheumaklinik Bad Nenndorf

University Education

2011 - 2016 Universität Osnabrück, Physics
Topic of the master thesis: 'Multiskalen-Absorptionsspektroskopie am Beispiel von TiO₂'
Sep 2016 Graduation: Master of science

Promotion

2016 - present Research scientist at the Laser Zentrum Hannover e.V., Fiber optics and Single-frequency lasers group

Declaration

I hereby declare that this thesis is my own work and effort and that it has not been submitted anywhere for any award. Where other sources of information have been used, they have been acknowledged.

<insert data and location>

Sven Hochheim

Acknowledgments

First of all, I am deeply thankful to Prof. Benno Willke for the supervision and to Prof. Detlef Ristau and Prof. Volker Quetschke for the evaluation of this thesis.

Furthermore, I acknowledge Dr. Dietmar Kracht and Dr. Jörg Neumann for giving me the opportunity to carry out my research at the Laser Zentrum Hannover e.V. as the atmosphere throughout the whole institute was always very motivating and encouraging. The laser development department was like a second family to me at all times.

Additionally, I am very thankful to Dr. Jörg Neumann and Dr. Peter Weßels for the amendment of this thesis and my publications because their remarks increased the corresponding quality significantly. I would also like to thank Dr. Kracht and Dr. Neumann for giving me the opportunity to present my work at diverse scientific conferences and to represent the Laser Zentrum Hannover e.V.

I am grateful to Dr. Peter Weßels and Dr. Michael Steinke for providing their support whenever I needed it, answering hundreds of questions, advising me countless times as well as for letting me the freedom to investigate all the (stupid) things that came to my mind.

In addition, thanks goes to the whole laser development department, in particular to Phillip Booker and Felix Wellmann for helpful discussions in the project. I want to specially thank Eike Brockmüller for his support with multiple fiber components.

Furthermore, I am thankful to Steffen Novotny and the fiber group of nLight for providing the 3C[®]-fibers and for detailed discussions about the experimental results and challenges.

Last but not least I would like to thank my family, who have always supported my decisions. This thesis is the result of a very long-term project that they initiated. I don't find the words to thank my wife Julia for what she has given to me during these years. She has been by my side all the time, making my life and myself better, and inspiring me every single day.

